

TAILORING MATERIAL PROPERTIES

TAILORING MATERIAL PROPERTIES BY FILLER
PARTICLE ARRANGEMENTS

BY

PEIYING JENNIFER TSAI, B.Sc., M.Sc.

A Thesis Submitted to the School of Graduate Studies
in Partial Fulfilment of the Requirements
for the Degree of
Doctor of Philosophy

McMaster University © Copyright by Peiyong Jennifer Tsai, April 2017

All Rights Reserved

Doctor of Philosophy (2017)
(Mechanical Engineering)

McMaster University
Hamilton, Ontario, Canada

TITLE: Tailoring Material Properties by Filler Particle
Arrangements

AUTHOR: Peiyong Jennifer Tsai
B.Sc., (Aeronautical and Astronautical Engineering)
National Cheng Kung University, Tainan, Taiwan
M.Sc., (Aeronautics and Astronautics)
University of Washington, Seattle, Washington,
USA

SUPERVISOR: Professor I.K. Puri

NUMBER OF PAGES: xii, 124

To my parents and my husband

Lay Abstract

The organization of filler particles in particle-polymer composites influences the properties of the bulk material. With the emergence of additive manufacturing, the external field assisted self-assembly of filler particles inside an elastomeric matrix is now possible. To fully utilize the benefits of this advanced manufacturing technology, a comprehensive understanding of structure-property relationships is necessary, since precise control over particle arrangements is still unachievable in most applications. This dissertation uses numerical simulations to model precise particle configurations, such as chainlike particle structures, to explore their influence on bulk mechanical stiffness, electrical permittivity, and thermal conductivity. The influence of filler volume fractions, interparticle and interchain spacing, particle sizes, zigzag angles, and chain orientations is investigated. When particles align into straight chains lying along the direction of loading, material properties are enhanced, whereas there is negligible effect when the chains are placed perpendicular to the loading direction. The introduction of a zigzag angle produces intermediate values, enabling finer tuning of material properties.

Abstract

The bulk properties of a material are governed by the internal particle arrangements. Nature has the luxury of arranging atoms into different morphologies that produce distinct properties among materials. The manipulation of atoms using human technology is both very expensive and inefficient. Fortunately, nanoparticles can be used to alter bulk material properties by varying their configuration inside materials. The self-assembly of nanoparticles is an effective method for organizing nanoparticles into designated arrangements, providing rapid and remote assembly with minimum human interference. Nanoparticles can either be preprogrammed to communicate with each other to form certain patterns under an external excitation, or be guided by external fields to assemble. The latter approach is relevant to the emerging development of additive manufacturing, broadening possibilities for material design. To fully utilize this facet of advanced additive manufacturing, a comprehensive understanding of material structure-property relationships is essential. However, precise control over particle arrangements using field-assisted assembly is still impractical. In this dissertation, a numerical approach using finite element analysis that explores the relationship between chainlike particle structures and material properties of elastomeric composites, specifically mechanical stiffness, electrical permittivity and thermal conductivity, is reported. With particles

aligning into linear chains parallel to the mechanical loading direction, the bulk stiffness enhances 100-fold compared to the same composite with randomly distributed particles. Similar trends are observed for electrical permittivity and thermal conductivity. In contrast, when chains are aligned perpendicular to the direction of mechanical loading, applied voltage, or the heat transfer path, the influence of particle chains on these material properties is negligible. The introduction of zigzag chains provides intermediate results, offering granular modulation over the bulk properties. The mechanical stiffness, electric permittivity, and axial thermal conductivity decrease gradually with increasing zigzag angle, while the transverse thermal conductivity increases as this angle is increased. The electric permittivity also increases with interchain spacing, but decreases as interparticle spacing increases. When the filler volume fraction is lower than 9%, smaller particles contribute towards higher permittivity, while when the volume fraction is larger than 9%, the sample containing larger particles has a higher permittivity. To predict the anisotropic thermal conductivity of a composite consisting of particle chains, a modified empirical model that accounts for the effects of interparticle spacing and zigzag angle is proposed. Prospective research directions are discussed in the last chapter.

Acknowledgements

A special thanks goes to my supervisor, Prof. Ishwar K. Puri, for the generous supervision, guidance, support, and understanding, especially in the times when life is covered in darkness. Acknowledgements also go to my supervisory committee members, Prof. Peidong Wu and Prof. Gu Xu, for precious discussion and guidance. Gratitude goes to my most important mentor, Dr. Suvojit Ghosh, for shining lights through my entire PhD career. All the gracious encouragement from Dr. Puri, Dr. Ghosh, Dr. Wu, and Dr. Xu is at the heart of the success of this research. I would also like to thank Prof. Raffaella De Vita, Prof. Jake Socha, Prof. Marwan Al-Haik, and Prof. Mayuresh Patil whom Suvojit and I visited at Virginia Tech for many valuable inspiration and discussions. I also wish to acknowledge the assistance of Suchitra Nayak with some of the simulations, Yu-Chen Ting with the use of ABAQUS, and Dr. Souvik Pal with major discussion on thermal properties. Thank all the colleagues at Multiphysics Research Group, Abdel Fattah Abdel Rahman, Tahereh Majdi, Ahmed Abdalla, Ri Chen, Sarah Mishriki, and Dr. Rakesh Sahu for great discussions as well as all the good times we shared. Thank the LORD for leading me to meet these amazing people and fulfilling my dream of completing this degree. This work is dedicated to the author's family in appreciation for all of the support and sacrifice to make this degree a reality.

Contents

Lay Abstract	iv
Abstract	v
Acknowledgements	vii
1 Introduction	1
1.1 Learn from Nature	1
1.2 Smart Material Self-assembly	3
1.3 Field Assisted Additive Manufacturing	5
1.4 Numerical Simulation Approaches	6
1.5 Model Simplification	8
1.5.1 Representative Volume Element	9
1.5.2 Interfaces and Defects	10
1.5.3 Monodispersed Isotropic Filler Particles	10
1.5.4 Percolation	11
1.6 Outline	12
1.6.1 Mechanical Stiffness	12
1.6.2 Electrical Permittivity	13
1.6.3 Thermal Conductivity	13

1.6.4	Conclusion and Future Directions	14
2	Tailoring Material Stiffness by Filler Particle Organization	15
2.1	Introduction	16
2.2	Materials and Methods	17
2.3	Results and Discussion	21
2.4	Conclusion	28
2.5	Acknowledgements	28
2.6	Supporting Information	29
2.6.1	Boundary Conditions for Unit Cell Methods	29
2.6.2	Hyperelastic Model Verification	30
3	Influence of Particle Arrangement on the Permittivity of an Elastomeric Composite	47
3.1	Introduction	48
3.2	Materials and Methods	49
3.3	Results and Discussion	51
3.4	Conclusion	58
3.5	Acknowledgements	60
3.6	Supporting Information	60
3.6.1	Model Verification	60
3.6.2	Determination of a_x	62
3.6.3	Results for zigzag configurations with varying particle sizes	63
4	Tailoring Anisotropic Thermal Conductivity by Varying Particle Organization in Nickel-PDMS Composites	71
4.1	Introduction	72

4.2	Materials and Methods	74
4.3	Results and Discussion	78
4.4	Conclusion	84
4.5	Acknowledgements	85
4.6	Supporting Information	85
4.6.1	Simulation methods, settings, and verification	85
4.6.2	Model verification for random configuration	88
4.6.3	Packing fraction for simple cubic structures	90
5	Conclusion and Future Directions	97
5.1	Conclusion	97
5.2	Future Directions	99
5.2.1	Model Improvements	99
5.2.2	Other Particle Organizations	100
5.2.3	Wing Design of Micro Aerial Vehicles	101
	Bibliography	103
A	Matlab Code for Random Configurations	111
A.1	RangGen2_rad_v1.m	111
B	Matlab Code for Calculating Thermal Conductivity	119
B.1	conductivity2.m	119
B.2	Batch Processing	122
B.2.1	BatchPost_k.m	122
B.2.2	BatchPost_k_zigzag.m	123

List of Figures

2.1	Schematics of axial, lateral, random, and zigzag configurations	19
2.2	Stress-Strain curves for axial, lateral, random, and zigzag configurations	22
2.3	Example of Von Mises stress map	24
2.4	Young's modulus vs. volume fraction and zigzag angle	26
2.5	evaluation of hyperelastic models	35
2.6	Silicone rubber test data from Arruda and Boyce	36
2.7	Hyperelastic model evaluation using Silicon rubber from Arruda and Boyce	37
2.8	Material evaluation of large strain	38
2.9	Uniaxial extension, biaxial extension, and pure shear tests for rubber	38
2.10	Comparison of initial shear modulus for Arruda-Boyce, Yeoh, Ogden models	39
2.11	Verification of Arruda-Boyce model for rubber	40
2.12	Verification of Arruda-Boyce parameters for rubber	41
3.1	Schematics of a modelled parallel capacitor and chain structures	50
3.2	Permittivity vs. interparticle spacing and clearance	53
3.3	Influence of interchain spacing on permittivity	55

3.4	Influence of particle sizes and volume fractions on permittivity .	57
3.5	Influence of zigzag angle on permittivity	59
3.6	Simulated results of effective relative permittivity for random configuration	63
3.7	Results for zigzag configurations with varying particle sizes . . .	64
4.1	Schematics of axial and zigzag chains	75
4.2	Conductivity vs. volume fraction and interparticle spacing . . .	77
4.3	Axial and transverse conductivities vs. zigzag angle	80
4.4	Contour and line plots of axial and transverse conductivities predicted using the proposed model	83
4.5	Examples of the temperature distribution map for straight and zigzag chains	86

Chapter 1

Introduction

1.1 Learn from Nature

We, as human beings, love to build things. Ancient people built objects and structures, such as stone tools in prehistoric Stone Age and the pyramids of Giza, using materials they could find in nature without much knowledge about the characteristics of these materials. As material science developed, in the 21st century we use artificial or synthesized materials to build almost everything. These things closely affect our daily life, such as smartphones, things that are implanted inside our bodies, e.g., pacemakers and artificial tissues, or even the Mars Rover deployed to explore another planet. The material properties of these human engineered materials are often homogeneous, or uniform, throughout the entire material. Homogeneity is convenient for manufacturing processes and also easy for us in developing fundamental theories; however, this is not how Mother Nature constructs things.

The invention of the microscope opens up our understanding about how Mother Nature creates things. Through electron microscopes, we observe how

she arranges atoms into different formations that govern the outcomes of materials. Then, by assembling these materials heterogeneously, natural objects and living creatures are formed. Due to the heterogeneity, the attributes of materials found in nature are often distributed non-uniformly, resulting in gradients of material properties on the final objects. For example, a mechanical stiffness gradient is found on insect wings, which are relatively stiff at leading edges yet compliant at the trailing edges (Combes and Daniel, 2003), providing collision resilience (Mountcastle and Combes, 2014) as well as load-lifting enhancement during a flight (Mountcastle and Combes, 2013). Cuticle cells are responsible for such stiffness heterogeneity through curving and folding of a single layer of cells, or changing the orientation of the chitin-protein fibres (Combes, 2010; Sample *et al.*, 2015; Vincent, 2002). Similarly, the heterogeneous distribution of stiffness on fish fins and scales affects the manner a fish swims, offering passive propulsion in the presence of vortex wakes, which minimizes the energy consumption of a fish in swimming, i.e., less active muscular actuation is required (Beal *et al.*, 2006; Esposito *et al.*, 2012; Long *et al.*, 1996; Shelton *et al.*, 2014). Soft tissues such as ligaments (Tan *et al.*, 2015) also has stiffness heterogeneity to help maintaining internal organs in place. Besides these stiffness variations stated above, the nanostructure-induced heterogeneity also influences other material attributes. The unique transparent feature of the wings of the glasswing butterflies is a result of the special pillar-like nanostructures (Siddique *et al.*, 2015). The dark brown and white coloured areas appearing on the same transparent wing show only slight differences in their nanostructures. They are both formed by scales, but the scales in the brown region have membranes while those in the white region do not.

These examples demonstrate again the wondrous work of nature. The

capability of arranging atoms to form complex nano- and micro-structures that lead to the perfect features of matter is her divine privilege. What we human beings can do is to develop advanced technologies of fabrication and material designs that can mimic, as close as possible, the way nature works. These futuristic techniques also need to meet the requirements of affordability, accessibility, and rapid production to satisfy our modern life.

1.2 Smart Material Self-assembly

Nanotechnology has been booming since the IBM researchers (Eigler and Schweizer, 1990) demonstrated the capability of arranging individual atoms, in this case xenon atoms, on a surface. This atomic scale resolution has extremely low throughput and is often restricted by the choice of atoms. Nanoparticles, which have the size of only a few thousands atoms, can be organized more easily and also maintain the ability of controlling the bulk material properties by varying their organizations (Glotzer and Solomon, 2007). Several efficient methods of organizing nanoparticles have been developed. For instance, optical tweezers are used to move individual nanoparticles one at a time and achieve high precision nanoscale resolution (Guffey and Scherer, 2010). Complex 2D patterns composed of nanospheres can be generated using vapour deposition beams (Nemiroski *et al.*, 2014). Such methods, however, require sophisticated instruments with extremely high costs that often, in general, are only realizable in scientific research institutes. Therefore, for real life applications, a cheaper, simpler, and easier way of organizing particles is desired.

Self-assembly is an assembly technique in which matter assembles into an object or a specific shape without the intervention of direct human labour.

The ability to organize multiple particles simultaneously greatly enhances the effectiveness of the assembly technique during a manufacturing process. In addition, for a scenario when an object is located at a remote or hazardous place, being difficult to reach or manoeuvre, the capability of the object to self-assemble and self-repair under the influence of an applied field or external stimulation from its surroundings is extremely attractive.

Self-assembly can generally be categorized into three groups by the manner of assembly, namely individual assembly, origami folding, and chain folding. The first involves the assembly of several individual elements into an organized arrangement through the help of external stimuli inserted into the system (Bazin and Zhu, 2013), similar to playing Lego[®] that builds 1D, 2D, or 3D structures using fundamental building blocks. Each element is connected by mechanical connections (Tibbits, 2012; Tibbits and Cheung, 2012), magnetic forces (Tibbits, 2014), chemical bonding (Nakakubo and Shimoyama, 2000), surface tension (Syms *et al.*, 2003), etc. Origami folding is similar to folding a paper airplane that a flat pattern is predefined followed by a folding sequence to form the desired 3D shape (Tibbits, 2014; Pandey *et al.*, 2013; Felton *et al.*, 2013). The direction of folding is designed using mechanical forces, such as surface tension and capillary force (Py *et al.*, 2007). Another concept similar to popup books is also common (Sreetharan *et al.*, 2012; Whitney *et al.*, 2011). The chain folding (Tibbits and Cheung, 2012), or DNA folding (Rothmund, 2006), produces the designed configuration by folding a long chain-like string that is pre-programmed to describe the shape requested. The techniques mentioned above all require certain application of external stimuli to trigger the assembly process, such as heat (Pandey *et al.*, 2013), stochastic energy in water and in space (Tibbits, 2014), as well as light (Genzer *et al.*, 2014).

1.3 Field Assisted Additive Manufacturing

Unlike origami folding and chain folding, the pattern formed through individual assembly is often guided by external fields, such as electric (Morariu *et al.*, 2003; Batra and Cakmak, 2015), magnetic (Wang *et al.*, 2009; Ghosh and Puri, 2013), acoustic (Collino *et al.*, 2015), etc., without preprinting or preprogramming the substances. Initially, individual particles or elements are placed randomly either in a liquid matrix or in air. Then, with the application of external fields, these elements move towards the designated locations controlled by the fields, allowing rapid assembly.

The simplest configuration assembles through external fields is chainlike structures. When electric or magnetic fields are applied, dipole moments are induced within filler particles, triggering self-movements from the interparticle dipolar interactions. The resulting configuration is chainlike structures oriented along the field lines. Batra and Cakmak (2015) demonstrates the formation of particle chains depends on the frequency of applied electric field. In their experiments, particle chains are observed at 100 Hz but not 10 Hz or 1000 Hz. They also shows the particle-to-particle interaction which controls the interchain spacing and the chain alignments is influenced by the electric field strength and applied voltage. The higher the field strength, the greater the interparticle forces, leading to better alignments along chains but wider interchain spacing due to larger repulsive forces. Ghosh and Puri (2013) further shows the height or length of the chainlike structures decreases with increasing the magnetic field gradient. For acoustic fields, Collino *et al.* (2015) presents that the orientation of particle chains is parallel to the direction of acoustic wave propagation, and the formation of chains is governed by the focusing and

scattering forces acting on the particles by the acoustic waves.

It is foreseeable that more complex structures with better precision controls will be realized in the near future. Combine with the emerging development of additive manufacturing, i.e., 3D printing, this field assisted self-assembly technique gains more and more attention and value.

Additive manufacturing is now an established method of fabrication. It is simple, affordable, convenient, and highly customizable, which fits our modern life where increasing on-demand services are desired. However, the materials created from traditional additive manufacturing often have homogeneous material properties, lacking the heterogeneous characteristics of natural materials. Luckily, with the help of field assisted assembly, printing products with heterogeneous properties is plausible (Kokkinis *et al.*, 2015). As an example, fill one of the cartridges of a 3D printer with mixture of particles and liquid polymer, extrude the mixture while applying magnetic fields to form the desired particle organization, and then solidify the polymer mixture before removing the magnetic field. The particles are now kept in organized patterns that create heterogeneous properties as we deem fit.

1.4 Numerical Simulation Approaches

To fully utilize additive manufacturing that employs field assisted assembly, the relationship between embedded structure and bulk material properties must be understood. Then, one can print an object with designated heterogeneous material properties by instructing the machine to organize the particles in specific configurations. All this sounds simple and easy; however, the interaction between particle and matrix as well as between particles themselves is still an

active research field. A comprehensive understanding of the structure-property relationship is absent. Furthermore, precise control of particle arrangements using these external fields is still inconceivable. Therefore, a numerical simulation approach to investigate the structure-property relation is an appropriate and feasible approach.

Through simulations, the bulk properties of a composite can be predicted before the actual material is fabricated. In the theory of composite materials, the simplest estimation of bulk properties of a composite material is made by applying parallel or series, e.g., isostrain and isostress, assumptions that frame its upper and lower bounds (Chawla, 2012; Fu *et al.*, 2008). For particulate-reinforced composites, which are composed of filler particles embedded inside matrix materials, large filler volume fractions are required to significantly enhance the bulk material properties of the composites (Young and Lovell, 2011). Theoretical approximations of the bulk material properties use empirical, semi-empirical, or micromechanics approaches (Fu *et al.*, 2008; Móczó and Pukánszky, 2008). Some well-known examples of empirical approaches include modified Einstein's equations (Einstein, 1956) that is solely a function of the filler volume fraction (Guth, 1945), and a modified rule of mixtures method that is a function of the moduli of the elastomer matrix and particle material and the filler volume fraction (Fu *et al.*, 2002). Semi-empirical approaches additionally account for particle shapes and the Poisson ratio of matrix material (Halpin, 1969b,a; Tsai, 1968). A maximum particle packing fraction, whose value ranges from 0.7405 for ideal face-centre-cuboid (fcc) arrangement to 0.37 for loose random packing with agglomerations (Nielsen and Landel, 1994), is often included in semi-empirical methods (Móczó and Pukánszky, 2008; Nielsen, 1970; Nielsen and Landel, 1994).

Bulk material properties, also called effective properties, obtained from empirical or semi-empirical approaches only account for particle volume fraction, material moduli, and the maximum packing fraction for which the value is typically uncertain (Móczó and Pukánszky, 2008; Nielsen, 1970; Nielsen and Landel, 1994). Micromechanics approaches are more granular since they consider filler geometries, such as the organization of the dispersed particles. However, the geometric effect, e.g., of rod- and chain-like structures, is statistically averaged throughout the entire material and represented by shape functions to determine a homogeneous modulus (Nielsen, 2005). Conventional micromechanics approaches predict the effective properties using approximations and bounds by assuming that the effective properties are isotropic (Hashin and Shtrikman, 1963; Mori and Tanaka, 1973). Numerical approaches, which can involve Fast Fourier Transforms (Moulinec and Suquet, 1998) and the phase-field method (Ni and Chiang, 2007), are usually based on inclusion theory (Eshelby, 1957). The inclusion theory, for example, initially estimates an effective strain for the inclusion, the value of which has a strong influence on how accurate the final predicted stiffness is. That estimated effective strain, however, cannot be obtained precisely (Ni and Chiang, 2007). Therefore, we choose to adopt finite element analysis to account for the complexity of particle organization, the filler volume fraction, and the material properties of each constituent with minimal assumptions.

1.5 Model Simplification

The goal of this dissertation is to provide conceptual material design strategies for exploring wider parameter space on the influence of simple microstructure

geometry on bulk material properties. Complex analyses were not performed as they will dilute the scope of this work otherwise. Several simplification techniques and assumptions were made and described in this section, granting considerable computational cost savings and undisturbed concentrations on geometrical influences of filler arrangements. The results, therefore, are largely qualitative yielding profound values for conceptual design.

1.5.1 Representative Volume Element

When using numerical simulation approaches to estimate bulk material properties of a composites, a smaller modelling domain instead of the whole material chunk is desirable in order to reduce computational cost. Therefore, the selection of this small domain is extremely important. It has to be small enough to maximize the computational economy yet maintain the same material behaviour and properties as the whole material to represent the whole. For a material, the choice of the small domain is not unique as long as the elected domain is sufficiently representative (Michel *et al.*, 1999). Such domain is then called a representative volume element (RVE) or a unit cell.

The aforementioned statistical models and finite element methods both embrace the unit cell concept to predict homogeneous bulk properties from a heterogeneous unit cell. While the homogenization process of statistical models uses statistical averaging (Ni and Chiang, 2007), that of finite element methods requires appropriate boundary conditions. The results from inappropriate boundary conditions are often misleading (Li, 2008). Considering a square unit cell containing a quarter circle pattern around its lower left corner, for example, when symmetry boundary conditions are applied to both the left

and bottom sides of the square and periodic conditions are on the other two sides, the repeated pattern appears as circles. However, if periodic boundary conditions are imposed on all four sides, the repeated pattern is now quarter circles. Thus, with suitable boundary conditions, the results obtained from finite element methods and statistical models are essentially the same.

1.5.2 Interfaces and Defects

Another important consideration is the interfacial bonding between the filler and polymer matrix. It is very common in real world material systems to functionalize filler particles through surface treatment to enhance their adhesion to the polymer matrix (Bele *et al.*, 2015). Such bonding enhancement can be mechanical, physical, or chemical (Chawla, 2012). No matter which technique is used, they create an interfacial layer with properties differentiate from the matrix and the filler (Abdel Fattah *et al.*, 2016). Moreover, the thickness of this layer depends strongly on the experimental treatments. In addition, defects within the composite material, such as air bubbles or impurity, can occur throughout the material and is extremely difficult to predict the location and constitution of their occurrence. All these variables will unduly complicate our analyses. Therefore, the models used in this dissertation assume perfect bonding between filler and matrix and no defects inside the entire material in order to focus on the geometrical influence of different filler microstructures.

1.5.3 Monodispersed Isotropic Filler Particles

Due to the nature of RVEs, the filler particle microstructures are considered being dispersed uniformly and periodically throughout the material. Since all

simulations presented in this research are in steady state, the use of RVEs yields ergodicity in a material volume. The size of the filler particles employed here is also uniform even though in reality the particle size often falls into a certain range due to fabrication uncertainties. The average size is then adopted as the uniform size of particles in this study.

Regarding material properties of the filler and matrix, only those with isotropic properties are considered. This helps the simplification of investigating the anisotropy brought by the particle microstructures.

1.5.4 Percolation

Percolation is another term commonly seen in synthesizing particle-polymer composite materials (Nielsen, 2005; Batra and Cakmak, 2015; Jouni *et al.*, 2013), referring to a state in which the originally isolated particles form a connected path that goes through the material system. As the filler volume fraction increases, the probability of particles forming a connected path increases, and the lowest filler volume fraction which initiates this connectivity is identified as the percolation threshold volume fraction. In this dissertation, simple percolation is examined in the form of connected chain structures in an RVE. However, for the material system containing randomly distributed filler particles, percolation is intentionally avoided by limiting the volume fraction to be less than that of the percolation threshold. Besides, through either simulation or futuristic high precision manipulation of particle arrangements, the ability of precise control of particle locations also eliminates percolation where it is undesirable.

1.6 Outline

Through finite element analysis, the effective mechanical stiffness, electric permittivity, and thermal conductivity of a particulate-reinforced polymer composite are investigated in each chapter. The particle structure studied herein is focused on chainlike structure which is the most common structure produced by field assisted techniques. Other forms of filler particle arrangements are the prospective directions of research in the future. This section provides a brief outline of the following chapters.

1.6.1 Mechanical Stiffness

In Chapter 2, effective mechanical stiffness of elastomeric composites consisting of stiff filler particles is discussed. Concise background information and the implication of the mechanical stiffness gradients are provided. With the help of stiff particles arranging in chainlike structures within a soft elastomer matrix, the effective stiffness increases up to two orders of magnitude. Granular control can be achieved by arranging the particles in a zigzag fashion. The content of this chapter has been previously published in a paper entitled *Tailoring Material Stiffness by Filler Particle Organization* by Peiyong J. Tsai, Suvojit Ghosh, Peidong Wu, and Ishwar K. Puri, available online on October 4, 2016 (DOI: 10.1021/acsami.6b10895) in the *ACS Applied Materials and Interfaces*. The author of this thesis is the first author and the main contributor of the above mentioned publication.

1.6.2 Electrical Permittivity

Effective electrical permittivity of elastomeric composite containing electric conductive filler particles is explored in Chapter 3. Brief background information and potential applications of the enhancement of electrical permittivity of elastomeric composites are presented. The influence of each characteristic parameter of the chainlike structure on the effective permittivity is discussed. The content of this chapter has been previously published in a paper entitled *Influence of Particle Arrangement on the Permittivity of an Elastomeric Composite* by Peiyong J. Tsai, Suchitra Nayak, Suvojit Ghosh, and Ishwar K. Puri, available online on January 3, 2017 (DOI: 10.1063/1.4973724) in the *AIP Advances*. The author of this thesis is the first author and the main contributor of the above mentioned publication.

1.6.3 Thermal Conductivity

In Chapter 4, effective thermal conductivity of polymer composites comprising high thermal conductive filler particles inside low thermal conductive polymer matrix is investigated. Brief background information and the potential application of directional thermal conductivity are presented. A modified empirical model which accounts for the directional influence of chainlike structure as well as the effect of the internal particle alignment angle is proposed. The content of this chapter has been previously submitted in a paper entitled *Tailoring Anisotropic Thermal Conductivity by Varying Particle Organization in Nickel-PDMS Composites* by Peiyong J. Tsai, Souvik Pal, Suvojit Ghosh, and Ishwar K. Puri, submitted on March 13, 2017 to the *Composites Science and Technology*. The author of this thesis is the first author and the main contributor

of the above mentioned publication.

1.6.4 Conclusion and Future Directions

In the last chapter, the contents of the preceding chapters are summarize with an emphasis on the dependency of chainlike structures on the bulk stiffness, permittivity, and thermal conductivity and their potential applications. Some areas of interests, such as interfacial properties and polydispersed and anisotropic fillers, are suggested to bridge the simplified conceptual work with real world material systems. In addition, a few possible filler particle organizations worth exploring are suggested. Finally, a specific application on the material design of biomimicking micro unmanned aerial vehicles that benefits from the heterogeneous material properties is discussed.

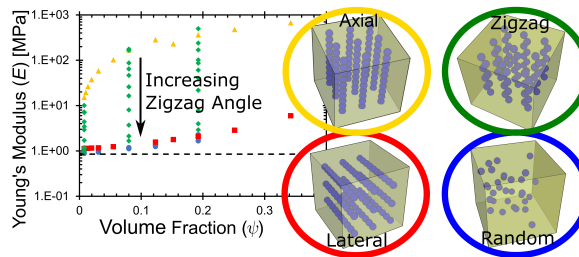
Chapter 2

Tailoring Material Stiffness by Filler Particle Organization¹

Abstract

In the context of emerging methods to control particle organization in particle-matrix composite materials, we explore, using finite element analysis, how to modu-

late the material bulk mechanical stiffness. Compared to a composite containing randomly distributed particles, material stiffness is enhanced 100-fold when filler particles are aligned into linear chains lying parallel to the loading direction. In contrast, chains aligned perpendicular to that direction produce



¹Reproduced with permission from Tsai, P. J., Ghosh, S., Wu, P., & Puri, I. K. (2016). Tailoring Material Stiffness by Filler Particle Organization. *ACS Applied Materials & Interfaces*, 8(41), 27449–27453. <http://doi.org/10.1021/acsami.6b10895> Copyright 2016 American Chemical Society.

negligible stiffness change. These outcomes reveal how zigzag chains, which provide intermediate results, can modulate stiffness. The stiffness decreases gradually with increasing zigzag angle θ over a range spanning 2 orders of magnitude.

2.1 Introduction

Many naturally occurring materials, e.g., ligaments (Becker and De Vita, 2015) and insect wings (Combes and Daniel, 2003), have heterogeneous mechanical stiffness. This intrinsic heterogeneity enhances mechanical functions, such as the resilience (Kappiyoor *et al.*, 2011) and damage tolerance of natural materials (Mountcastle and Combes, 2014), which are typically difficult to achieve for traditional engineered materials. Nature creates heterogeneity in stiffness by embedding rigid materials within a soft matrix, e.g., in the form of veins in insect wings (Combes, 2010) or fin rays in fish tails (Esposito *et al.*, 2012). The distribution of stiffness is often the key enabler to their enhanced mechanical functions (Milton and Cherkaev, 1995; Sigmund, 1994; Tai *et al.*, 2007).

Stiff filler particles can be distributed inside a soft polymer matrix to produce particle-matrix composite materials with heterogeneous stiffness. Various methods have emerged to control the organization of the filler particles. Typically, the particles are first dispersed in a liquid prepolymer, then organized using electromagnetic (Ghosh and Puri, 2013; Abdel Fattah *et al.*, 2016a), centrifugal (Hashmi and Dwivedi, 2007), or gravitational forces (Kirugulige and Tippur, 2006) that steer the stiff filler particles and hold them in place until the polymer is solidified to form a supportive matrix. This method can be

used to create materials with a desired inhomogeneous stiffness distribution (Ghosh *et al.*, 2015; Abdel Fattah *et al.*, 2016b).

Like the aforementioned natural materials, heterogeneities in the properties of engineered materials lead to the emergence of functional bulk properties. Thus, exercising control on the geometry of heterogeneities, i.e., the organization of filler particles in a particle-matrix composite, creates the conceptual basis for a “material printer” (Ghosh *et al.*, 2015). Beginning with the same polymer-particle solution, it is possible to vary the final properties of the composite material by *a priori* selecting the required organization with the potential of achieving desired bulk attributes, e.g., mechanical stiffness (Varga *et al.*, 2006), magnetic susceptibility (Ghosh and Puri, 2015), thermal (Dallas *et al.*, 2006), and electrical (Fragouli *et al.*, 2014) conductivities. Here we examine the feasibility of the concept by demonstrating that the bulk stiffness of a particle-matrix composite can be tailored to any desired value within bounds spanning 2 orders of magnitude simply by the deliberate organization of the filler particles.

2.2 Materials and Methods

The bulk mechanical stiffness of a material sample is best measured by its response to a uniaxial tensile load. Thus, to probe the influence of filler organizations on bulk stiffness, we conduct finite element simulations of tensile loading for material samples that have different particle organizations. These simulations allow precise control over particle organization and detailed scrutiny of the stress and strain fields, which are challenging to do through

typical experiments. Theoretical approximations of stiffness that use empirical, semiempirical, or micromechanical approaches often have the limitation of uncertain parameters (Fu *et al.*, 2008; Móczó and Pukánszky, 2008). Because of this, we use the ABAQUS finite element package, which has the advantage of having minimal assumptions. Polydimethylsiloxane (PDMS) is selected as the polymer matrix and iron spheres for filler particles because of the relatively wide use of both materials, but the results are generally applicable to other stiff particles and soft materials. Besides particle organization, the bulk mechanical stiffness of particle-matrix composites is also influenced by interfacial adhesion between the particles and the matrix (Móczó and Pukánszky, 2008; Chawla, 2012). However, to investigate the influence of filler organization alone, we assume perfect particle-matrix interfacial bonding. This investigation examines the influence of (1) filler volume fraction ψ , (2) particle radius r , and (3) particle arrangement angles θ relative to their chain orientations, which are also termed as “zigzag angles”. These results are compared with those obtained for a material sample that includes randomly distributed particles. Figure 2.1 presents an overview of the simulations.

We investigated chainlike particle organizations labelled “axial”, “lateral”, “random”, and “zigzag”, as illustrated in Figure 2.1. For the “axial” case, chains were positioned parallel to the loading direction, whereas for “lateral”, they were placed normal to it. The particles contained in both “axial” and “lateral” chains were perfectly aligned end-to-end with each other. However, the centres of adjacent particles in “zigzag” chains formed internal zigzag angles θ (Figure 2.1e) relative to each other. The zigzag angles varied from 0 to 60° where $\theta = 0^\circ$ indicates a straight chain without any zigzag. For the “random”

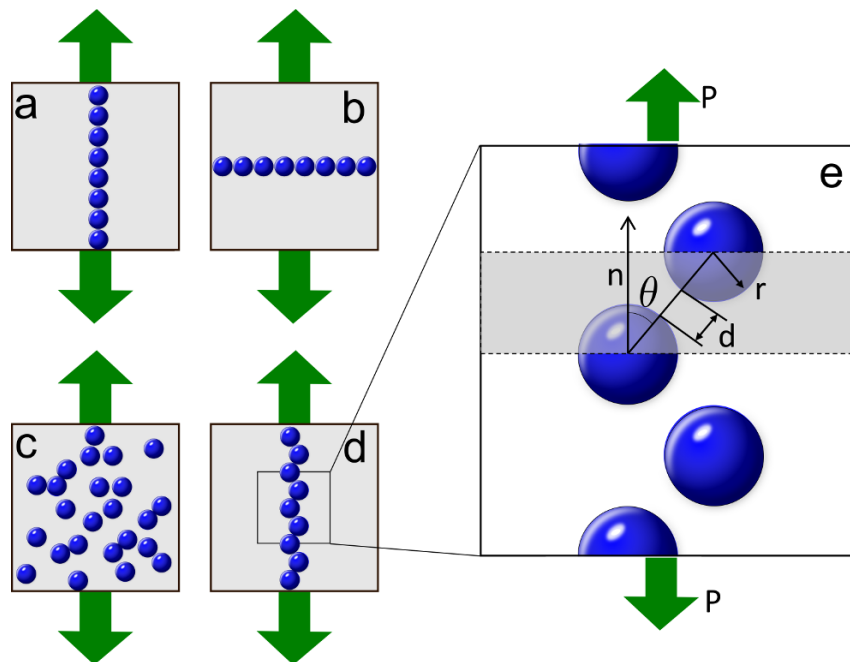


Figure 2.1: Overview. Using finite element analysis, the influence of filler particle organization on bulk material stiffness was examined by determining the response of iron-PDMS samples containing four different particle organizations, namely (a) “axial”, (b) “lateral”, (c) “random”, and (d) “zigzag”, to uniaxial tensile loading P . (e) Within the “zigzag” configuration, the zigzag angle θ was varied to examine its influence on bulk material stiffness.

case, ten spherical particles were randomly distributed in a unit cell. Five realizations were obtained for each volume fraction through a set of coordinates that correspond to the centres of the ten particles. Each set was generated using a pseudorandom number series subject to constraints that ensured that particles (1) did not overlap and (2) remained within the bounds of the cell.

The filler iron particles were modelled as linear elastic solids with Young's modulus $E = 211$ GPa and Poisson's ratio $\nu = 0.29$ (Kaye and Laby, 1993). PDMS was modelled as a hyperelastic solid where the stress $\boldsymbol{\sigma}$ is related to the strain $\boldsymbol{\varepsilon}$ through the strain energy density

$$U(\boldsymbol{\varepsilon}) \equiv \int_0^{\boldsymbol{\varepsilon}} \boldsymbol{\sigma} : d\boldsymbol{\varepsilon}. \quad (2.1)$$

After carefully considering various hyperelastic constitutive models, we adopted the Arruda and Boyce model (Arruda and Boyce, 1993) for its accuracy in describing elastomers. Assuming PDMS to be incompressible, the model describes the strain energy density as

$$U = \mu \left\{ \frac{1}{2} (\bar{I}_1 - 3) + \frac{1}{20\lambda_m^2} (\bar{I}_1^2 - 9) + \frac{1}{1050\lambda_m^4} (\bar{I}_1^3 - 27) + \frac{19}{7000\lambda_m^6} (\bar{I}_1^4 - 81) + \frac{519}{673750\lambda_m^8} (\bar{I}_1^5 - 243) \right\}, \quad (2.2)$$

where μ , λ_m , and \bar{I}_1 denote the shear modulus, chain-locking stretch, and first deviatoric strain invariant, respectively (Simulia, 2013). Mechanical test data for PDMS (Zang *et al.*, 2012) was used to determine the values of $\mu = 0.169$ MPa and $\lambda_m = 1.23$ using ABAQUS. The effective stiffness was evaluated from

the slope of the macroscopic nominal stress Σ_n and strain ε_n curve, namely

$$\Sigma_n = \frac{F_i}{A_0}, \quad \varepsilon_n = \frac{V_i}{b}, \quad (2.3)$$

where F_i and V_i denote the total reaction force and displacement along the loading direction i , respectively, A_0 the initial cross-sectional area, and b the initial length.

The unit cell method, or representative volume element (RVE) (Segurado and Llorca, 2002; Michel *et al.*, 1999), was employed to simulate a bulk material using a tractable modelling domain that is large enough to represent the bulk. The accuracy of using a unit cell was confirmed by comparing the results with those obtained for the same material sample but for other larger and smaller cell sizes. The boundary conditions for unit cell modelling ensured that the surfaces remained parallel to their initial states after deformation (see the Supporting Information for details). Several numerical tests were performed to indicate the unit cells we selected were representative of the bulk material.

2.3 Results and Discussion

The stress-strain curves for the “axial”, “lateral”, “random”, and “zigzag” configurations under uniaxial tension are presented in Figure 2.2. With increasing ψ , all configurations exhibit material stiffening, which is expected for a composite material containing a dispersed phase that is stiffer than the matrix (Varga *et al.*, 2006; Fu *et al.*, 2008). From particulate composite theory, this stiffening is a function of ψ alone, regardless of particle organizations (Fu *et al.*, 2008; Chawla, 2012). We show that the magnitudes of the stiffness enhancements

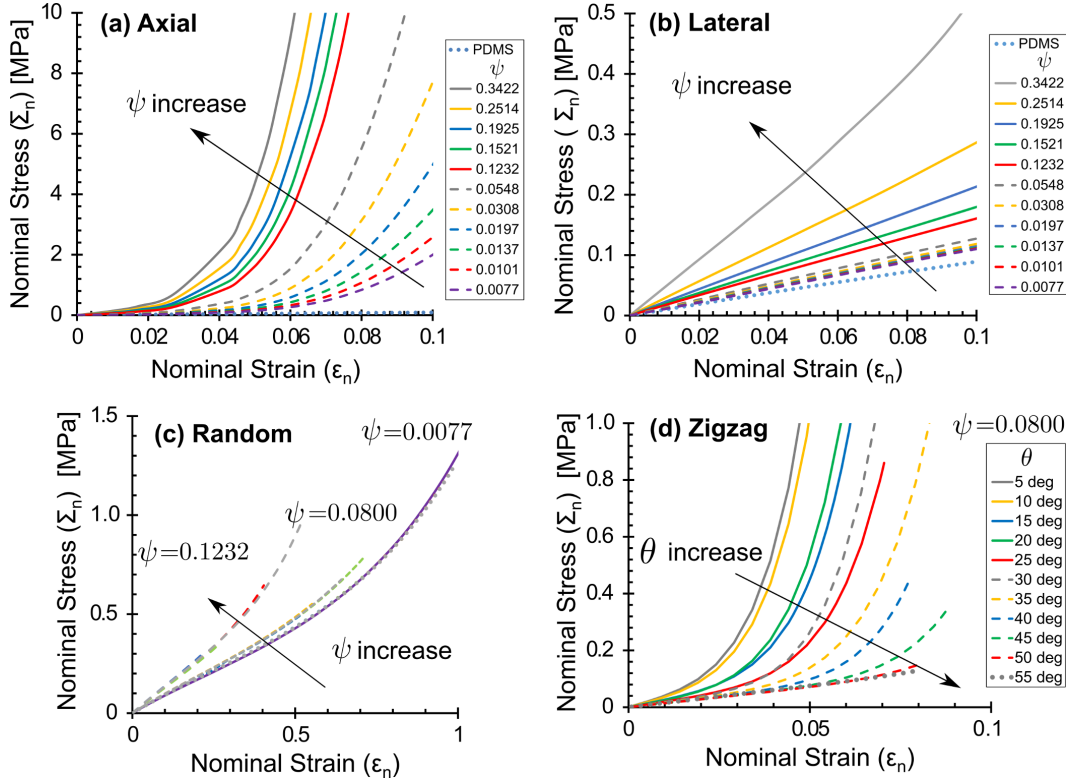


Figure 2.2: Simulated tensile tests of composite samples with particle configurations in (a) “axial”, (b) “lateral”, (c) “random”, and (d) “zigzag” organizations. (For brevity, results are only presented for $\psi = 0.0800$ samples for the “zigzag” chains.) The “axial” configuration induces substantially higher stiffness and strain-hardening than the “random” configuration, whereas the “lateral” configuration produces negligible stiffness enhancement. The “zigzag” configuration produces intermediate results that are a function of the zigzag angle θ .

are significantly influenced by the filler particle arrangements. This effect is most pronounced for the “axial” cases. Similar trends, but with smaller magnitudes, are observed for the other configurations. Introducing an internal zigzag angle that alters chain alignment away from a linear configuration reduces the stiffness enhancement. The larger the value of θ , the smaller the stiffness enhancement.

We explain these stiffness variations by considering the distributions of

the particle-induced stress and strain heterogeneities within the composite. Because the embedded particles are rigid relative to the soft PDMS matrix, the deformation due to loading is mainly distributed within the elastomer matrix itself. Most of this load is borne through deformation of the elastomer between two adjacent particles where stress concentration is clearly observed, as shown in Figure 2.3. The elastomer that is available to bear the uniaxial load is more constrained by adjacent rigid particles that bound it in the “axial” configuration rather than in the other configurations because these latter configurations provide a larger material volume that can be deformed in the loading direction. Thus, for the same load, the elastomer between adjacent particles in the “axial” sample experiences a significantly higher stress and consequently has a much higher stiffness, which is representative of the strain-hardening of rubbers. In contrast, the “lateral” configuration experiences a much lower stress and thus exhibits a lower stiffness because the constraint around the elastomer bearing the load is smaller.

The “zigzag” configuration is intermediate between the two cases discussed above because the deformation constraint due to neighbouring particles is itself a combination of the “axial” and “lateral” cases. For instance, when $\theta = 10^\circ$, the “axial” component along the loading direction is greater than the “lateral” component, while for $\theta = 50^\circ$ this behaviour is reversed. Because the “axial” component has a stronger constraint, the greater the axial load leading to higher stress (Figure 2.3) and therefore, the larger the stiffness enhancement. This provides a means to tune the stiffness to a desired value by combining these two components, which we do by simply altering the internal zigzag angle of a particle chain.

To compare the stiffness quantitatively, the effective Young’s moduli E are

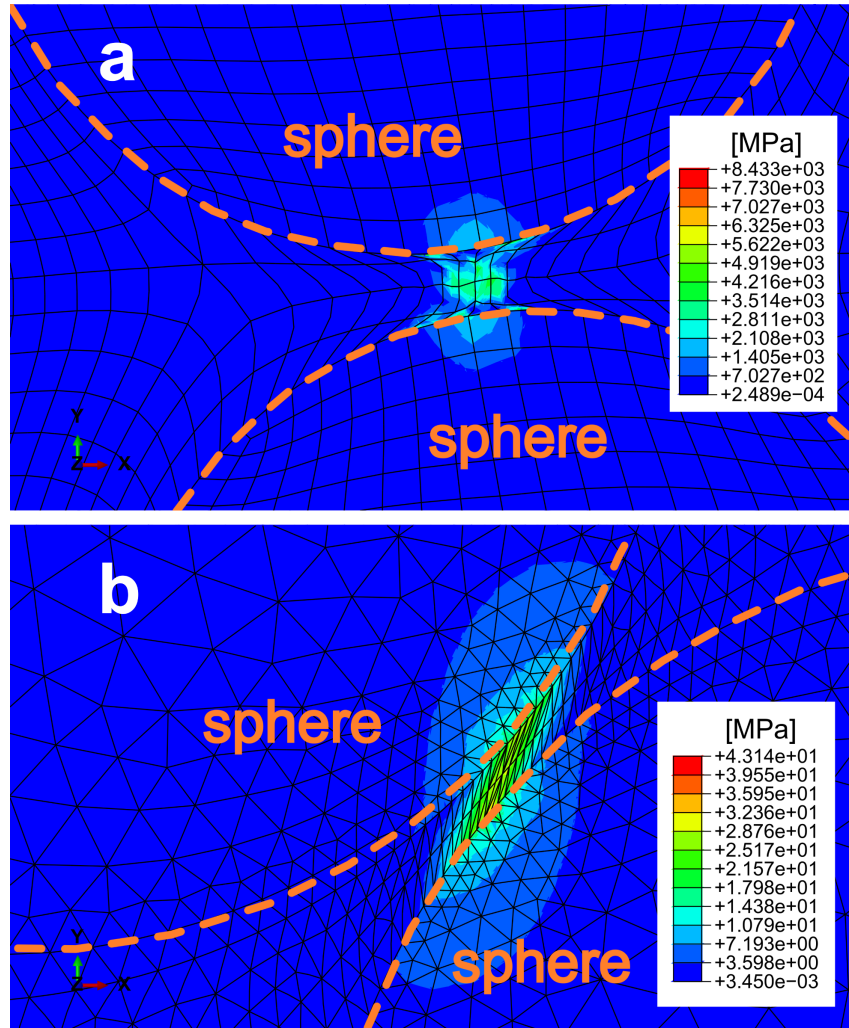


Figure 2.3: Example of Von Mises stress map for (a) $\theta = 10^\circ$ and (b) $\theta = 50^\circ$. Deformation due to uniaxial loading occurs mainly in the matrix between two particles, leading to stress concentration occurs in this region. The higher the stress the higher is the stiffness. (Results are presented for $\psi = 0.0800$ and $r = 0.0569 \mu\text{m}$ at 0.06 nominal strain.)

calculated from the slopes of the macroscopic nominal stress-strain curves at 0.06 strain. These moduli are presented with respect to varying ψ in Figure 2.4a for various configurations, and with θ in Figure 2.4b for “zigzag” chains. The upper and lower bounds of the effective Young’s moduli are also demonstrated using isostrain and isostress assumptions (Chawla, 2012). Figure 2.4a shows that the moduli for all cases increase with increasing ψ . Note that this increase is more significant for the “axial” case that exhibits a more rapid rise until $\psi \approx 12.3\%$ and after that it becomes more gradual. For all ψ , the “axial” configuration is stiffer than the others. Even with a relatively small filler concentration $\psi = 0.77\%$, the Young’s modulus for the “axial” case is 17.4 MPa while for the “lateral” and “random” configurations the corresponding values are 1.1 and 0.9 MPa. A value of ψ as low as $\approx 5.5\%$ provides a hundredfold stiffness enhancement when the filler particles are arranged in an “axial” configuration.

The large difference between the “axial” and “random” moduli is to be expected. However, modifications to the “zigzag” configuration result in more granular control. The Young’s moduli for the “zigzag” results have values intermediate between “axial” and “random” when θ is varied (Figure 2.4b). As θ increases, the stiffness decreases until it reaches a minimum at $\theta \approx 55^\circ$, illustrating that it is possible to manipulate the stiffness over more than 2 orders of magnitude by simply changing the chain geometry.

Differences in E between the “lateral” and “random” cases are minor and the moduli for these two cases overlap once $\psi \approx 20\%$, as shown in Figure 2.4a. For “random”, the probability that adjacent particles can be arranged along the loading direction increases with ψ , providing a much higher stiffness increase than for the corresponding “lateral” case when ψ is large. This shows that

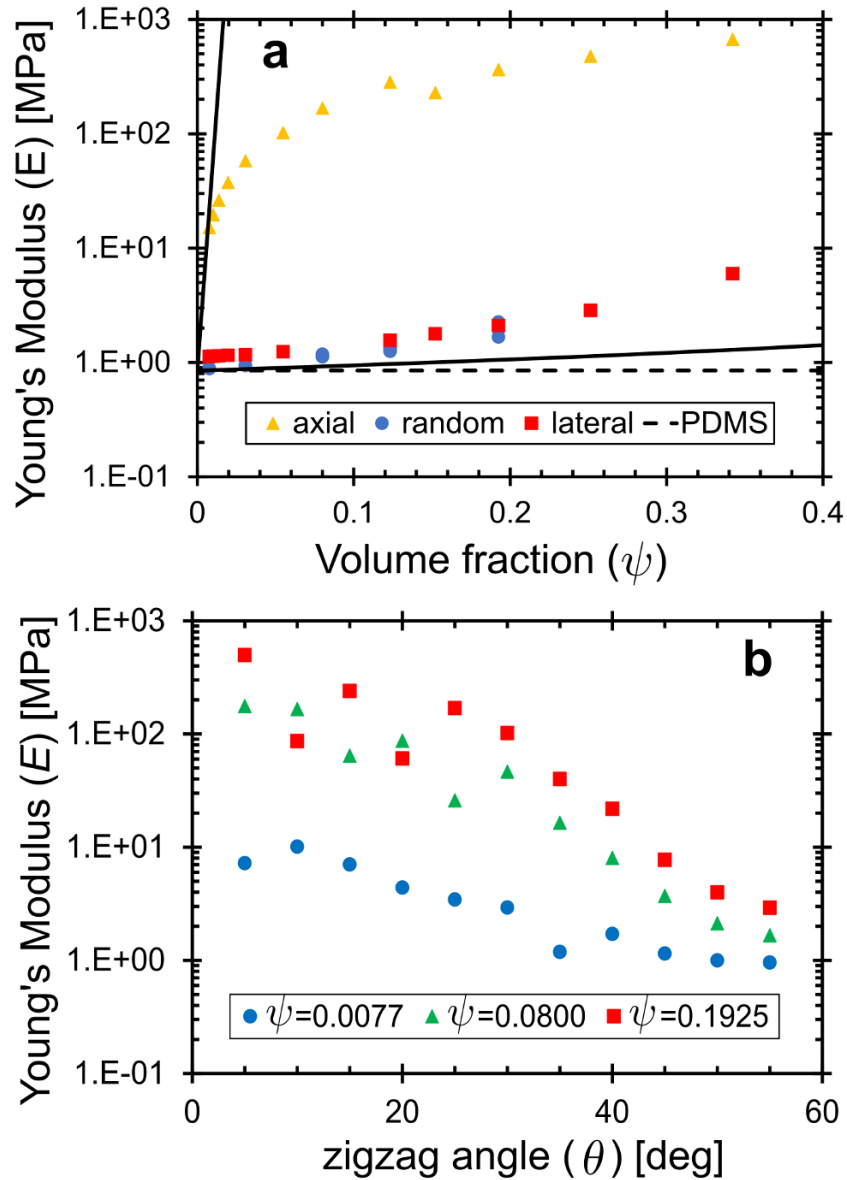


Figure 2.4: The “zigzag” angle θ provides granular control of bulk mechanical stiffness, measured by the Young’s modulus $E = \partial\Sigma_n/\partial\varepsilon_n$ at $\varepsilon_n = 0.06$. (a) E increases with volume fraction ψ for the “axial”, “lateral”, and “random” configurations, as anticipated. When $\psi < 0.2$, the difference in E between “lateral” and “random” is minor. The two solid lines frame the upper and lower bounds using isostrain and isostress assumptions. (b) For “zigzag”, E lies between values for the “axial” and “lateral” cases. It decreases as θ increases and reaches a minimum at $\theta \approx 55^\circ$.

control over stiffness enhancement is limited to cases when the direction of a stiff filler particle chain lies parallel to that of loading.

The PDMS matrix is a rubber-like elastomer that undergoes hysteresis upon loading and unloading and its deformation can be described from thermodynamic considerations. When an ideal elastomer deforms, its internal energy remains constant. In reality, energy is lost when an elastomer experiences large strain so that, upon unloading, the path of the stress-strain curve differs from the prior loading curve. However, hysteresis does not occur for relatively small strain or with softer elastomers (Kim *et al.*, 2011). Furthermore, at larger strains, hysteresis occurs only during the first cycle, and successive loading and unloading cycles up to the same strain exhibit relatively small hysteresis (Kim *et al.*, 2011). Since the simulations did not consider hysteresis, our observations only apply to the uniaxial tensile behaviours of elastomeric composites that undergo small hysteresis.

The enhancement of directional stiffness discussed here furthers the possibility of introducing anisotropic stiffness, common for fibre-reinforced composites, to particulate-reinforced composites. Filler particles with submicrometer or smaller sizes can easily be distributed heterogeneously. Thus, particle chains can conceivably be placed and manipulated locally, tailoring small-scale stiffness gradients. Using additive manufacturing, these locally tailored composite elements can be assembled into objects (Kokkinis *et al.*, 2015) with functional stiffness gradients, which should be useful for applications where overall flexible or rubberlike materials that have local stiffness are desired, e.g., for biomaterials such as artificial tissues and membranes.

2.4 Conclusion

In summary, we investigated how a specified material stiffness is produced for a composite material that consists of PDMS and distributed iron filler particles. Our results show that the stiffness of the composite can be tailored toward desired values by varying the particle arrangement and the internal angle between adjacent particles that are arranged to produce longitudinal chains. The axial stiffness is enhanced by almost 2 orders of magnitude when particles are arranged in the form of linear chains as compared to the case where the particles are randomly distributed in the matrix. The stiffness enhancement increases with increasing particle volume fraction, is most prominent when the direction of loading is aligned with that of chain organization, and approaches a minimum value when the zigzag angle $\theta \approx 55^\circ$. Consequently, enabling appropriate particle arrangements could tailor small-scale stiffness in applications where stiffness gradients can be beneficial. The results provide the basis for designing stiffness into a particulate-reinforced elastomeric material by heterogeneously organizing stiff particles within a soft matrix.

2.5 Acknowledgements

This work is supported by Natural Sciences and Engineering Research Council of Canada Discovery Grant (NSERC-DG) RGPIN-2014-04066.

2.6 Supporting Information

2.6.1 Boundary Conditions for Unit Cell Methods

Applying the appropriate boundary conditions is essential when using unit cell methods or representative volume elements. In the case when the repetitive configuration shows symmetry, such as in Fig. 2.1a, b, and d, the modelled volume is reduced to 1/8 of the repetitive cell by applying the boundary conditions that account for symmetry (Li, 2008; Li and Wongsto, 2004). For uniaxial tension in y direction,

$$\begin{aligned}
 u|_{x=0} &= 0, & u|_{x=b_x} &= b_x \varepsilon_x = U, \\
 v|_{y=0} &= 0, & v|_{y=b_y} &= b_y \varepsilon_y^0 = V, \\
 w|_{z=0} &= 0, & w|_{z=b_z} &= b_z \varepsilon_z = W,
 \end{aligned} \tag{2.4}$$

where u , v , and w denote displacements along the x , y , and z directions, b_j the dimension of the unit cell, $|_k$ the corresponding quantity at surface k , and ε_y^0 the prescribed macroscopic normal strain (while ε_x and ε_z are determined during simulations through the displacements U and W).

In ABAQUS, the symmetric boundary conditions, $u = U_1 = 0$, $v = U_2 = 0$, and $w = U_3 = 0$, are applied on the symmetric faces $x = 0$, $y = 0$, and $z = 0$, respectively. Equation constraints are implemented on the opposite surfaces

using a reference control point for each surface, as

$$\begin{aligned} X(\text{dof:1}) - C_x(\text{dof:1}) &= 0, \\ Y(\text{dof:2}) - C_y(\text{dof:2}) &= 0, \\ Z(\text{dof:3}) - C_z(\text{dof:3}) &= 0, \end{aligned} \tag{2.5}$$

where X , Y , and Z denote sets of nodes on the corresponding surfaces, and C_x , C_y , and C_z are node sets containing only a single reference point within each set to control the degree of freedom (dof), where dof:1, 2, and 3 are displacements along the x , y , and z directions. A displacement boundary condition is set on C_y as the prescribed uniaxial tensile strain through $b_y \varepsilon_y^0 = V$. No boundary conditions are applied on C_x and C_z . By using the control point and the equation constraints, the surfaces remain parallel to their initial states after deformation.

2.6.2 Hyperelastic Model Verification²

The first stage of this research is to perform the simulation of PDMS material using ABAQUS to verify the numerical model parameters that will be used on subsequent simulations. First, a comparison of seven different hyperelastic models fitting to a silicone rubber uniaxial compression test data (Bergström, 2013) was demonstrated. Fig. 2.5a shows the results of polynomial form models including Mooney-Rivlin model (i.e., 1st order polynomial), 2nd order polynomial, and 3rd order Ogden model. Fig. 2.5b shows the results of reduced polynomial models including Neo-Hookean (i.e., 1st order), Yeoh (i.e., 3rd order), Arruda-Boyce 8-chain model (Arruda and Boyce, 1993),

²This section is not included in the published material.

and Van der Waals model. The curve fitting results of 1st order models (i.e., Mooney-Rivlin and Neo-Hookean) and 3rd order Ogden models are slightly worse than other models. This is because 1st order models only captured the linear behaviour, and for Ogden model, it needs more than one set of different experiment data modes, such as uniaxial and planar test data, uniaxial and biaxial test data, or all three test data, as input to evaluate the parameters accurately.

Among these seven hyperelastic models, Arruda-Boyce, Ogden, and Yeoh models were used for further evaluations. The reasons for choosing these three models are the popular usage of Arruda-Boyce and Ogden models for hyperelastic large deformation simulations and Yeoh model is used to compare the unified parameter, initial shear modulus (μ_0), since it provide the initial shear modulus estimation closest to the real material. The first material to evaluate was silicone rubber (40 durometer)(Arruda and Boyce, 1993). The experimental data for uniaxial and plane strain compression tests are shown in Fig. 2.6. Using these two sets of test data as input, the curve fittings for uniaxial compression and plane strain compression are demonstrated in Fig. 2.7. The R^2 values, an indicator of the closeness of curve fitting (value of one being identical curves), for each model in two test modes are listed in Table 2.1 and the values are all well above 0.95. The Arruda-Boyce and Ogden models are even greater than 0.97. However, while using the test data as input for material properties in ABAQUS for large deformation simulation, the Ogden model has stability limit that means above or below certain deformation, the model behaviour becomes unrealistic as shown in Fig. 2.8. This indicates that in order to obtain accurate simulation results, the deformation range and test mode of material input should be as close to the target simulation range and mode as

possible.

Table 2.1: R^2 values for curve fitting of silicone rubber (Arruda and Boyce, 1993). The corresponding fitting curves are shown in Fig. 2.7.

R^2	Arruda	Ogden	Yeoh
Uniaxial	0.980	0.960	0.940
Planar	0.974	0.986	0.968
Average	0.977	0.973	0.954

Next questions arise concerning how many test modes are considered sufficient to obtain the parameters in hyperelastic models and how the input test mode data affect the parameters. In order to accomplish this, a more thorough test data for large deformation with uniaxial, biaxial, and plane strain test modes are desired. A widely used rubber material test that fulfill this requirement was performed by Treloar (1944). The experiment data for large deformation uniaxial tension, biaxial tension, and pure shear tests for a rubber material are shown in Fig. 2.9. The procedures for material evaluation were performed with various combinations of test modes as input data to determine the parameters for Arruda-Boyce, Ogden, and Yeoh models. Each model has its own parameters to describe the material properties, so the initial shear modulus (μ_0) is used as a unification for comparison. In Fig. 2.10, for all three models the values of initial shear modulus are more consistent when at least two test modes, uniaxial inclusive, were used. While using only one test data, the values for Ogden and Yeoh models fluctuate. Therefore, the parameters that acquired from feeding three test modes are considered most accurate. A comparison between simulation and test data using Arruda-Boyce

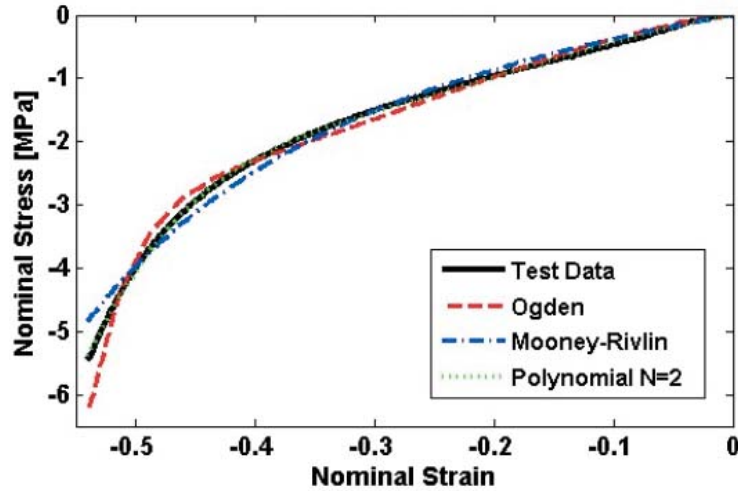
model for this case shows great closeness (Fig. 2.11). It is worth noting that for Arruda-Boyce model when uniaxial test data were used solely, the initial shear modulus is comparable to the consistent value when multiple test modes were used, shown in Fig. 2.10. This is the convenient aspect of Arruda-Boyce model which depends only on 1st invariant and only one uniaxial test data set is sufficient to obtain the parameters for describing the material behaviour successfully. Furthermore, the parameters in Arruda-Boyce model have physical meanings. Hereafter, the Arruda-Boyce model will be used for hyperelastic material simulation throughout this research.

Most of the simulations in this research use ABAQUS to perform the numerical simulations. It is necessary to verify the hyperelastic model parameters obtained in ABAQUS is comparable to others described in literatures. The materials used for this task are the same silicone rubber and rubber used above. The model parameters described by Arruda and Boyce (1993) are N and CR , where N is the number of statistical links in a crosslinking chain and CR is a function of chain density, Boltzmann's constant, and temperature. While shear modulus μ and locking chain stretch λ_m are used in ABAQUS, the relationships between these two sets of parameters are $\lambda_m = \sqrt{N}$, and $\mu = 3CR$. The parameters listed in Table 2.2 were all determined from uniaxial compression test data. Close parameters are expected since both of them use the same Arruda-Boyce model and test input data. The difference is the technique of curve fitting to determine the parameters. However, the λ_m value by ABAQUS for silicone rubber is almost twice of that by Arruda and Boyce, and μ value is not as expected neither. In the case of rubber, the closeness of both parameters is acceptable and as expected. In order to visualize the material behaviour using these parameters, planar compression simulations were

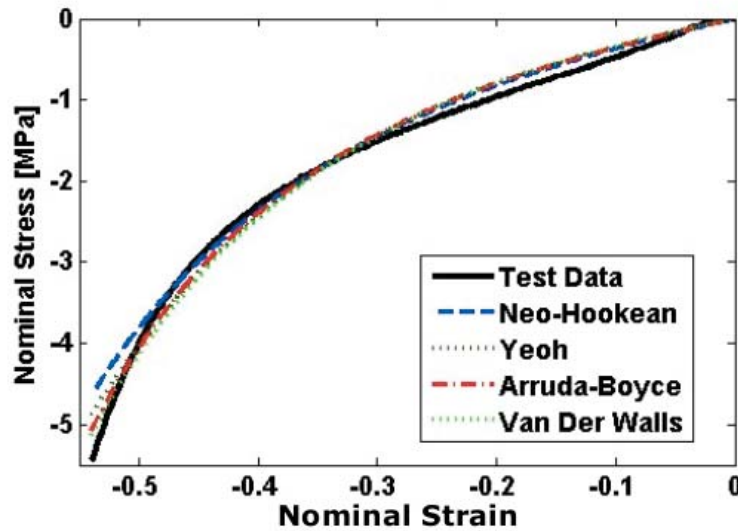
performed for silicone rubber and biaxial tension simulations for rubber. The nominal stress-stretch curves are shown in Fig. 2.12. For silicone rubber, the result using Arruda-Boyce parameters is closer to test data; while for rubber, the case with ABAQUS parameters is closer. Although the difference of the results can be observed, the overall description of the behaviour is comparable. Hence, it can conclude that either use ABAQUS to evaluate the parameters or use the ones described by the authors is both appropriate.

Table 2.2: Parameters described by Arruda and Boyce (1993) and those evaluated in ABAQUS with uniaxial test input solely for silicone rubber and rubber.

Material		N	CR	λ_m	μ
Silicone Rubber	Arruda and Boyce (1993)	7.9	0.16	2.81	0.435
	ABAQUS			6.09	0.515
Rubber	Arruda and Boyce (1993)	26.5	0.09	5.15	0.270
	ABAQUS			4.85	0.265



(a)



(b)

Figure 2.5: Curve fitting of silicone rubber (Bergström, 2013) under uniaxial compression. (a) General polynomial forms including 3rd order Ogden model. (b) 1st (Neo-Hookean) and 3rd (Yeoh) order reduced polynomial forms, Arruda-Boyce 8-chain model, and Van der Waals model. The fittings of 1st order and Ogden models results are slightly worse than others. All are considered good fitting.

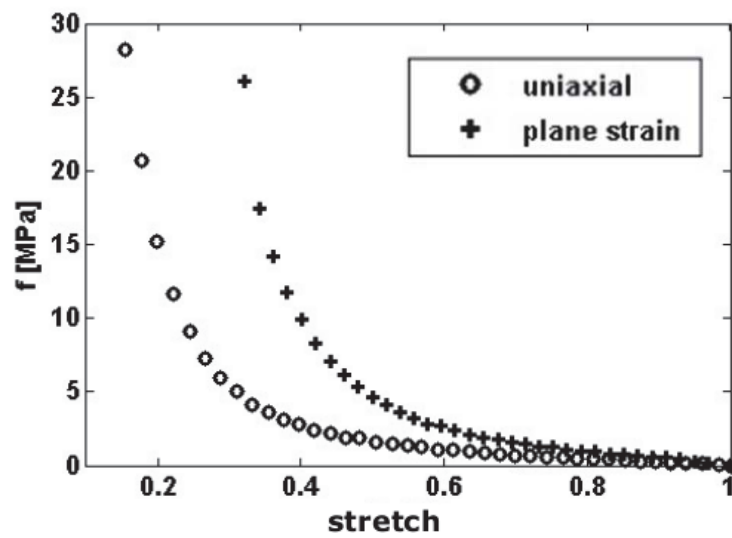
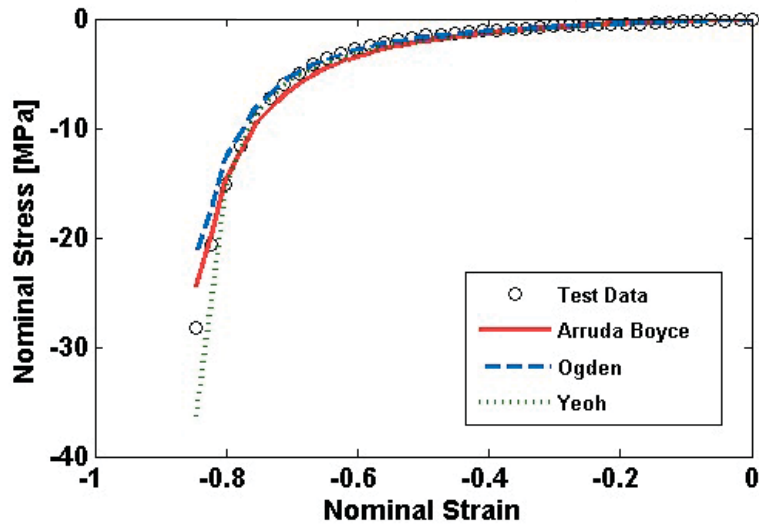
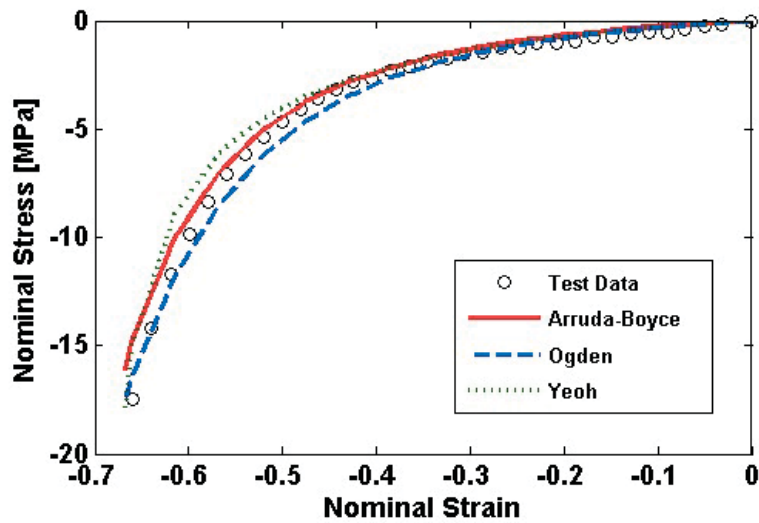


Figure 2.6: Uniaxial compression and plane strain compression test data for silicone rubber (Arruda and Boyce, 1993) where stretch is current length per unit initial length with the value of 1 being unstrained and values smaller than 1 is under compression deformations, and f is force per unit unstrained area (i.e., absolute value of nominal stress). The locking chain stretch is smaller in uniaxial compression which means with the same strain rate, the sample under uniaxial compression can endure longer than the one under plane strain compression before reaching the locking chain length.



(a)



(b)

Figure 2.7: Curve fitting of Arruda-Boyce, Ogden, and Yeoh models to silicone rubber (Arruda and Boyce, 1993) under (a) uniaxial compression and (b) plane strain compression. All three models show good fit with R^2 value well above 0.95.

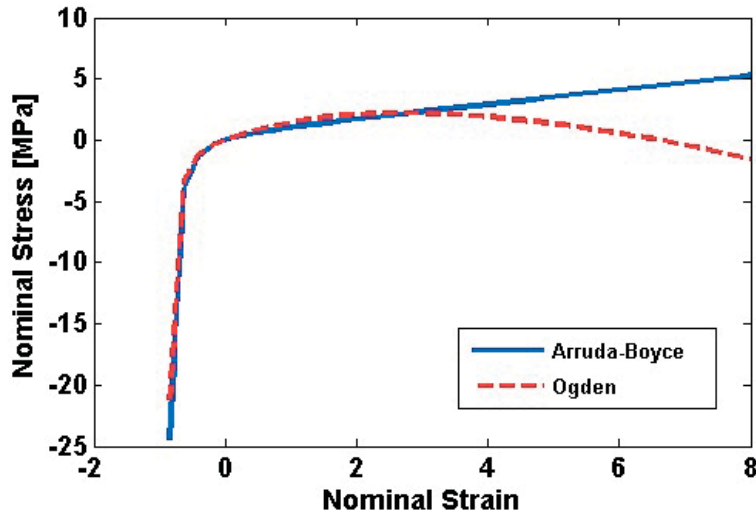


Figure 2.8: Evaluation of Arruda-Boyce and Ogden models under uniaxial simulation up to 800% strain. The uniaxial compression and plane strain compression test data of silicone rubber (Arruda and Boyce, 1993) are used as material input for both models. Stability limit is observed for Ogden model that behaves non-physically when the strain is greater than 200%.

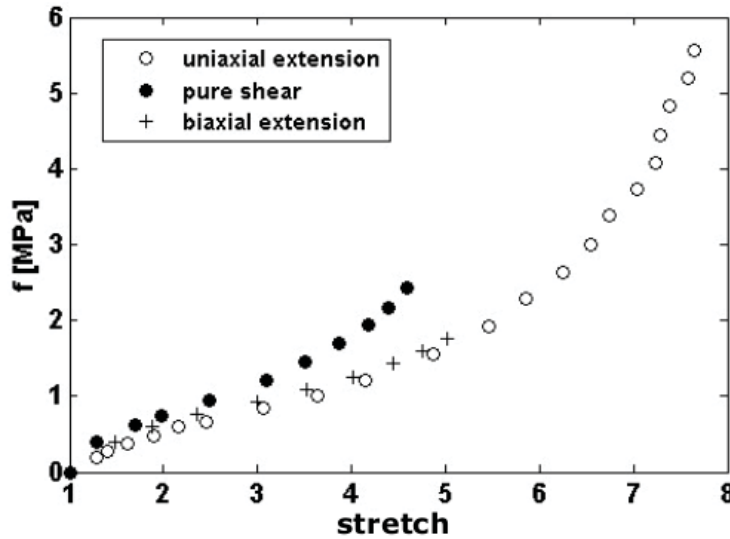


Figure 2.9: Uniaxial extension, biaxial extension, and pure shear tests for rubber by Treloar (1944) where f is force per unit unstrained area and stretch is current length per unit initial length. The behaviours under uniaxial and biaxial extension are close to each other while the behaviour under pure shear encountered greater f for the same stretch.

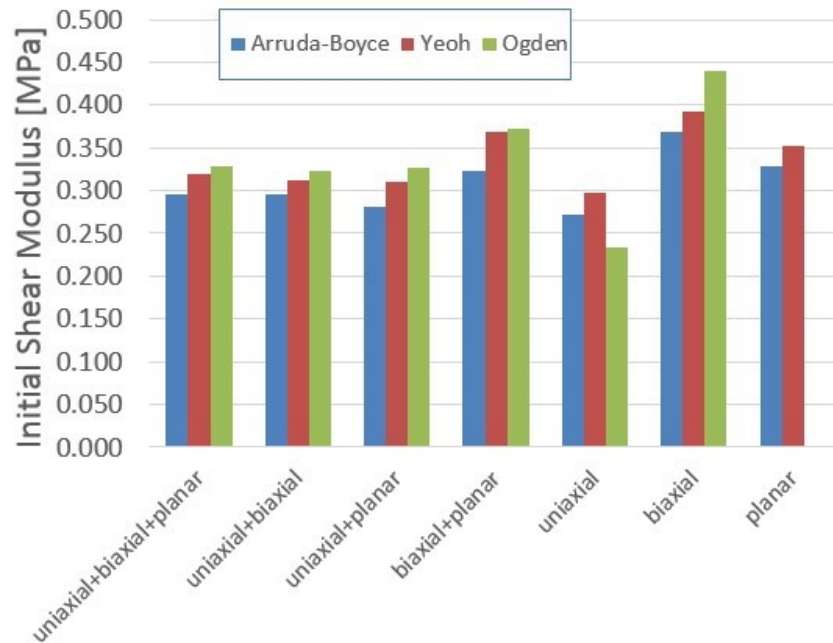


Figure 2.10: Comparison of initial shear modulus (μ_0) of rubber material among Arruda-Boyce, Yeoh, and Ogden models with different combinations of test modes input from Treloar (1944) for material parameter evaluation. Consistency is observed when more than two test modes including uniaxial were used as input. When only one test mode was used as input, the value fluctuates; however, the Arruda-Boyce model is able to obtain the consistent value using uniaxial solely.

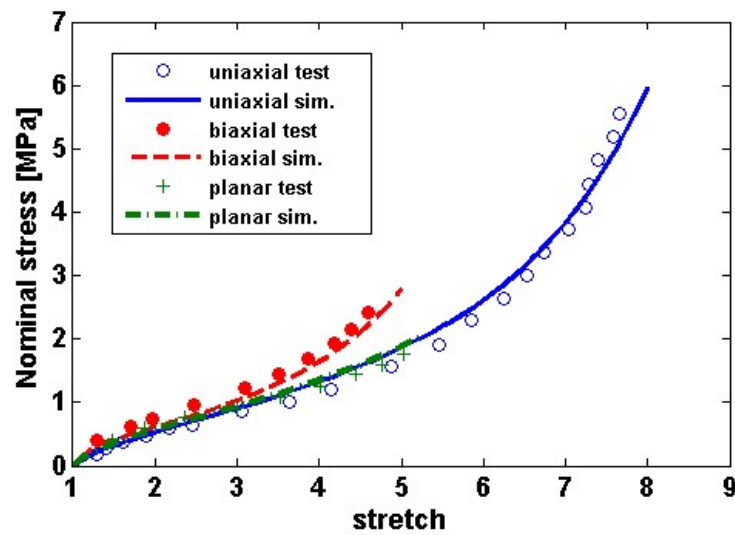
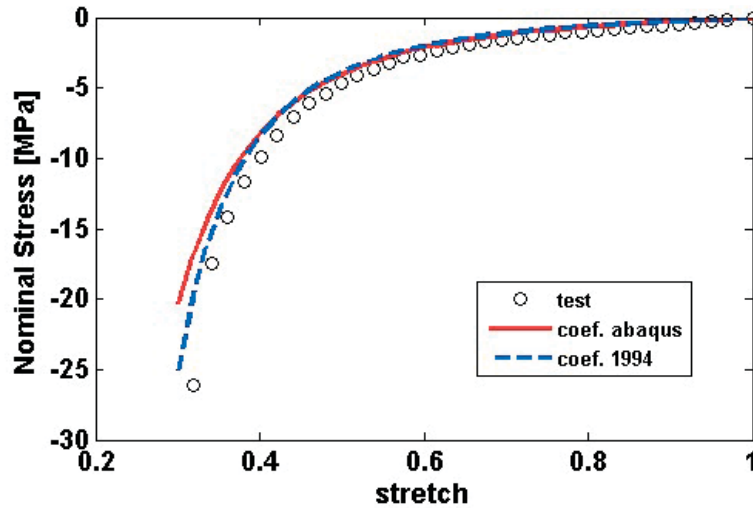
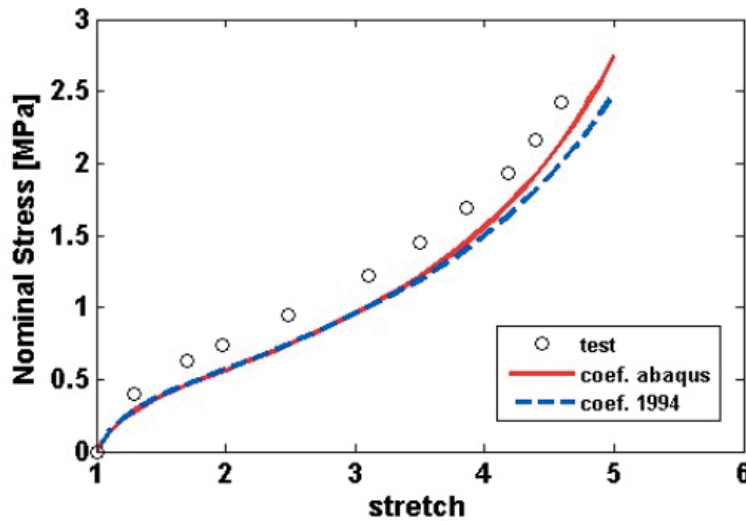


Figure 2.11: Comparison between simulation and test data (Treloar, 1944) for rubber material using Arruda-Boyce model with parameters obtained by applying all three test modes data as input. The simulation results well describe the behaviour observed from experiments.



(a) Planar compression of silicone rubber



(b) Biaxial tension of rubber

Figure 2.12: Comparison of Arruda-Boyce parameters evaluated in ABAQUS and described in Arruda and Boyce (1993) for (a) Planar compression of silicone and (b) biaxial tension of rubber. The uniaxial test data provided for silicone (Arruda and Boyce, 1993) and for rubber (Treloar, 1944) are used as input to obtain the parameters. (a) $\lambda_m = 6.09$ and $\mu = 0.515$ were obtained by ABAQUS; $N = 7.9$ and $CR = 0.145$ (i.e., $\lambda_m = 2.81$ and $\mu = 0.435$) (Arruda and Boyce, 1993). (b) $\lambda_m = 4.85$ and $\mu = 0.265$ in ABAQUS; $N = 26.5$ and $CR = 0.09$ (i.e., $\lambda_m = 5.15$ and $\mu = 0.265$) (Arruda and Boyce, 1993). Although the parameters may not as close as expected, both results show good simulations to experiment results.

Bibliography

- Abdel Fattah, A. R., Ghosh, S., and Puri, I. K. (2016a). Printing microstructures in a polymer matrix using a ferrofluid droplet. *J. Magn. Magn. Mater.*, **401**, 1054–1059.
- Abdel Fattah, A. R., Ghosh, S., and Puri, I. K. (2016b). Printing Three-Dimensional Heterogeneities in the Elastic Modulus of an Elastomeric Matrix. *ACS Appl. Mater. Interfaces*, **8**(17), 11018–11023.
- Arruda, E. M. and Boyce, M. C. (1993). A three-dimensional constitutive model for the large stretch behavior of rubber elastic materials. *J. Mech. Phys. Solids*, **41**(2), 389–412.
- Becker, W. R. and De Vita, R. (2015). Biaxial mechanical properties of swine uterosacral and cardinal ligaments. *Biomech. Model. Mechanobiol.*, **14**(3), 549–560.
- Bergström, J. S. (2013). PolymerFEM.com.
- Chawla, K. K. (2012). *Composite Materials Science and Engineering*. Springer, third edition.
- Combes, S. A. (2010). Materials, structure, and dynamics of insect wings as bioinspiration for MAVs.

- Combes, S. A. and Daniel, T. L. (2003). Flexural stiffness in insect wings. II. Spatial distribution and dynamic wing bending. *J. Exp. Biol.*, **206**(17), 2989–2997.
- Dallas, P., Georgakilas, V., Niarchos, D., Komninou, P., Kehagias, T., and Petridis, D. (2006). Synthesis, characterization and thermal properties of polymer/magnetite nanocomposites. *Nanotechnology*, **17**(8), 2046–2053.
- Esposito, C. J., Tangorra, J. L., Flammang, B. E., and Lauder, G. V. (2012). A robotic fish caudal fin: effects of stiffness and motor program on locomotor performance. *J. Exp. Biol.*, **215**(1), 56–67.
- Fragouli, D., Das, A., Innocenti, C., Guttikonda, Y., Rahman, S., and Liu, L. (2014). Polymeric Films with Electric and Magnetic Anisotropy Due to Magnetically Assembled Functional Nano fibers. *ACS Appl. Mater. Interfaces*, **6**(6), 4535–4541.
- Fu, S.-Y., Feng, X.-Q., Lauke, B., and Mai, Y.-W. (2008). Effects of particle size, particle/matrix interface adhesion and particle loading on mechanical properties of particulate-polymer composites. *Compos. Part B Eng.*, **39**(6), 933–961.
- Ghosh, S. and Puri, I. K. (2013). Soft polymer magnetic nanocomposites: microstructure patterning by magnetophoretic transport and self-assembly. *Soft Matter*, **9**(6), 2024–2029.
- Ghosh, S. and Puri, I. K. (2015). Changing the magnetic properties of microstructure by directing the self-assembly of superparamagnetic nanoparticles. *Faraday Discuss.*, **181**, 423–435.

- Ghosh, S., Tehrani, M., Al-haik, M. S., and Puri, I. K. (2015). Patterning the Stiffness of Elastomeric Nanocomposites by Magnetophoretic Control of Cross-linking Impeder Distribution. *Materials*, **8**, 474–485.
- Hashmi, S. A. R. and Dwivedi, U. K. (2007). Estimation of Concentration of Particles in Polymerizing Fluid during Centrifugal Casting of Functionally Graded Polymer Composites. *J. Polym. Res.*, **14**(1), 75–81.
- Kappiyoor, R., Balasubramanian, G., Dudek, D. M., and Puri, I. K. (2011). Elastomechanical properties of resilin. *Soft Matter*, **7**(22), 11006–11009.
- Kaye, G. and Laby, T. (1993). *Tables of physical and chemical constants*. Longman, London, UK, 15th edition.
- Kim, T. K., Kim, J. K., and Jeong, O. C. (2011). Measurement of nonlinear mechanical properties of PDMS elastomer. *Microelectron. Eng.*, **88**(8), 1982–1985.
- Kirugulige, M. S. and Tippur, H. V. (2006). Mixed-mode dynamic crack growth in functionally graded glass-filled epoxy. *Exp. Mech.*, **46**(2), 269–281.
- Kokkinis, D., Schaffner, M., and Studart, A. R. (2015). Multimaterial magnetically assisted 3D printing of composite materials. *Nat. Commun.*, **6**, 8643.
- Li, S. (2008). Boundary conditions for unit cells from periodic microstructures and their implications. *Compos. Sci. Technol.*, **68**(9), 1962–1974.
- Li, S. and Wongsto, A. (2004). Unit cells for micromechanical analyses of particle-reinforced composites. *Mech. Mater.*, **36**, 543–572.

- Michel, J. C., Moulinec, H., and Suquet, P. (1999). Effective properties of composite materials with periodic microstructure: a computational approach. *Comput. Methods Appl. Mech. Eng.*, **172**, 109–143.
- Milton, G. W. and Cherkaev, A. V. (1995). Which Elasticity Tensors are Realizable? *J. Eng. Mater. Technol.*, **117**(4), 483–493.
- Móczó, J. and Pukánszky, B. (2008). Polymer micro and nanocomposites: Structure, interactions, properties. *J. Ind. Eng. Chem.*, **14**(5), 535–563.
- Mountcastle, A. M. and Combes, S. a. (2014). Biomechanical strategies for mitigating collision damage in insect wings : structural design versus embedded elastic materials. *J. Exp. Biol.*, **217**(7), 1108–1115.
- Segurado, J. and Llorca, J. (2002). A numerical approximation to the elastic properties of sphere-reinforced composites. *J. Mech. Phys. Solids*, **50**(10), 2107–2121.
- Sigmund, O. (1994). Materials with prescribed constitutive parameters: An inverse homogenization problem. *Int. J. Solids Struct.*, **31**(17), 2313–2329.
- Simulia (2013). *Abaqus 6.12 user manual*. Simulia, Mason, OH.
- Tai, K., Dao, M., Suresh, S., Palazoglu, A., and Ortiz, C. (2007). Nanoscale heterogeneity promotes energy dissipation in bone. *Nat. Mater.*, **6**(6), 454–62.
- Treloar, L. (1944). Stress-strain data for vulcanised rubber under various types of deformation. *Trans. Faraday Soc.*, **40**(59).
- Varga, Z., Filipcsei, G., and Zrínyi, M. (2006). Magnetic field sensitive functional elastomers with tuneable elastic modulus. *Polymer*, **47**, 227–233.

Zang, J., Zhao, X., Cao, Y., and Hutchinson, J. W. (2012). Localized ridge wrinkling of stiff films on compliant substrates. *J. Mech. Phys. Solids*, **60**(7), 1265–1279.

Chapter 3

Influence of Particle Arrangement on the Permittivity of an Elastomeric Composite¹

Abstract

Elastomers are used as dielectric layers contained between the parallel conductive plates of capacitors. The introduction of filler particles into an elastomer changes its permittivity ε . When particle organization in a composite is intentionally varied, this alters its capacitance. Using numerical simulations, we examine how conductive particle chains introduced into polydimethylsiloxane (PDMS) alter ε . The effects of filler volume fraction ψ , interparticle d and interchain spacing a , zigzag angle θ between adjacent particles and overall chain

¹Adapted from Tsai, P. J., Nayak, S., Ghosh, S., & Puri, I. K. (2017). Influence of particle arrangement on the permittivity of an elastomeric composite. *AIP Advances*, 7(1), 15003. <http://doi.org/10.1063/1.4973724>

orientation, particle size r , and clearance h between particles and the conductive plates are characterized. When filler particles are organized into chainlike structures rather than being just randomly distributed in the elastomer matrix, ε increases by as much as 85%. When particles are organized into chainlike forms, ε increases with increasing ψ and a , but decreases with increasing d and θ . A composite containing smaller particles has a higher ε when $\psi < 9\%$ while larger particles provide greater enhancement when ψ is larger than that value. To enhance ε , adjacent particles must be interconnected and the overall chain direction should be oriented perpendicular to the conductive plates. These results are useful for additive manufacturing on electrical applications of elastomeric composites.

3.1 Introduction

Due to their low cost, lighter weight, and superior hydrophobicity, electrically insulating rubberlike materials, such as silicone rubber, are often used as the dielectric medium in capacitors. A dielectric medium is characterized by its permittivity, which is measured using a capacitor. At steady state, the relative permittivity, i.e., the ratio of the capacitance for a dielectric medium to that for a vacuum (Young and Lovell, 2011), is also called the static relative permittivity (Alger, 1996). The properties of its individual constituents influence the bulk properties of a composite material. The addition of conductive filler particles into an elastomer matrix improves the bulk relative permittivity of the composite, predictions of which can be based on mixing rules or effective medium theory (Ponnamma *et al.*, 2016; Pickles and Steer, 2013; Barber *et al.*, 2009). However, since predictive methods only consider the volume fractions

of the constituents, the geometrical arrangement of the filler particles, which also influences the bulk properties of the composite (Fragouli *et al.*, 2014; Tsai *et al.*, 2016), is not appropriately represented.

There are several means to organize the filler, e.g., using optical tweezers (Guffey and Scherer, 2010), electron beams (Tseng *et al.*, 2003), or field-assisted self-assemblies (Abdel Fattah *et al.*, 2016a,b; Collino *et al.*, 2015). The former two methods require expensive tools, whereas the latter method uses simpler tools (Truby and Lewis, 2016), such as application of an external magnetic field on a liquid polymer that is infused with suspended particles in ferrofluid (Abdel Fattah *et al.*, 2016a,b; Ghosh *et al.*, 2015; Ghosh and Puri, 2015, 2013; Ganguly and Puri, 2007). This creates a basis for a ‘material printer’. For instance, starting with a liquid polymer-particle mixture, desired bulk material attributes can be imparted to a material by *a priori* specifying the required particle arrangements. Enhancing the electric permittivity by organizing the filler particles in an elastomeric composite is expected to be beneficial for flexible electronics (Siegel *et al.*, 2010), 3D printed circuit boards (Juskey *et al.*, 1993; Schmidt *et al.*, 1991) and sensors (Frutiger *et al.*, 2015; Muth *et al.*, 2014), data storage (Sun *et al.*, 2011), optics (Ge *et al.*, 2011), and artificial muscles (Stoyanov *et al.*, 2011).

3.2 Materials and Methods

The simplest and most common particle organization using field-assisted control is a chainlike structure (Collino *et al.*, 2015; Ghosh and Puri, 2013; Boudenne *et al.*, 2015). Upon application of an external field, filler particles within the liquid prepolymer align along the field direction to form straight (Collino

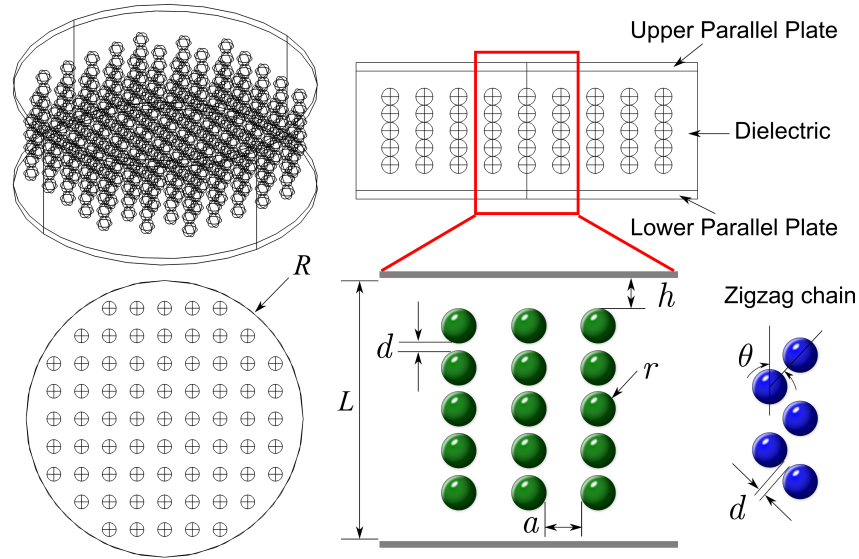


Figure 3.1: Model of a parallel capacitor consisting of two circular plates of radius R placed at a distance L apart. The capacitor is filled with a dielectric composite consisting of polydimethylsiloxane (PDMS) and spherical conductive particles. For simplicity, particle organization is limited to a chainlike structure characterized by interparticle spacing d , interchain spacing a , particle radius r , clearance h between the outermost particle of a chain and its adjacent plate, zigzag angle θ , and volume fraction of the particles ψ .

et al., 2015) or zigzag chains (Collino *et al.*, 2015; Han *et al.*, 2013; Borbáth *et al.*, 2012; Coquelle and Bossis, 2005). Therefore, we arrange conductive particles in chainlike structures that lie perpendicular to the conductive plates within polydimethylsiloxane (PDMS), as shown in Figure 3.1. Numerical simulations are employed to investigate the effects of different particle arrangements and sizes on the static relative permittivity of the composite using the COMSOL Multiphysics[®] package along with its electrostatics physics module. Our simulations assume uniform spherical particles, a steady electrostatic condition, and the absence of defect, fatigue and hysteresis. Despite these assumptions, the results are useful for designing and understanding how the electric permittivity of polymer-particle composites can be improved.

The relative permittivity of a composite (ε) is predicted by simulating a parallel capacitor at steady state without any current flow,

$$(1/V) \int_v (\rho_v dv) = C = (\varepsilon_0 \varepsilon A)/L, \quad (3.1)$$

where V denotes the applied voltage, $\int_v (\rho_v dv)$ total charge, C overall capacitance, ε_0 absolute permittivity of vacuum, A projected surface area of the plates, and L distance between the plates. The PDMS matrix has relative permittivity of 2.69 (Trajkovikj *et al.*, 2012). Since the relative permittivity of metal is infinite (van Enk, 1995; Klimchitskaya *et al.*, 2009), we assume a large value, 2.8×10^5 , for the conductive particles as an appropriate idealization. Our models are verified for pure PDMS and for PDMS-particle composites with randomly distributed particles using various approaches, as explained in the supplementary material. We also ensure that the applied voltages do not lead to electric field strengths inside the composites that exceed the breakdown strength for the PDMS matrix (Brochu and Pei, 2010). When particle chains are oriented parallel to the plates, ε lies within 3% of that obtained with randomly distributed particles. Therefore, only the results for chains oriented perpendicular to the plates are discussed.

3.3 Results and Discussion

We examine the influence of the following parameters on ε : (1) filler particle volume fraction ψ , (2) interparticle spacing d , (3) interchain spacing a , (4) clearance h between the outermost particle and its adjacent conductive plate, (5) zigzag angle θ (the acute angle between the centre-to-centre direction of

adjacent particles and the overall chain direction), and (6) size of the filler particles r , all of which are illustrated in the schematic of Figure 3.1.

Organizing filler particles into a chainlike structure within a dielectric composite enhances ε . For the same ψ , this ε enhancement diminishes rapidly as the interparticle spacing $d/2r$ increases and ε approaches the corresponding value for a composite that contains only randomly distributed particles, as shown in Figure 3.2a. This result is explained through the interparticle long-range dipolar interaction that decays proportionally to m^{-3} , where m denotes the average distance between neighbouring particles (Gubin *et al.*, 2009). A composite with higher ψ has larger ε , which agrees with the mixing rule concept (Barber *et al.*, 2009). The ε enhancement is most pronounced for $d/2r = 0$ when the particles form continuous chains and it is negligible when $d/2r > 0$, i.e., when discontinuous chains are formed. Thus, when the composite contains continuous filler particle chains, ε enhancement is more significant than when discontinuous chains are included in it. Hence, results for composites that include continuous particle chains are discussed below.

Consider that the two clearances between each plate of a capacitor and their nearest particles form two smaller capacitors that are connected in series by a continuous conductive particle chain, i.e.,

$$1/C = (V_1 + V_2)/Q = V/C, \quad (3.2)$$

where V_1 and V_2 denote the electric potentials across each of the two capacitors. No matter how V_1 and V_2 change, the electric potential V across the two plates is constant. Therefore, when the entire filler organization is placed off-centre, changing h does not significantly influence ε , as shown in Figure 3.2b. Thus,

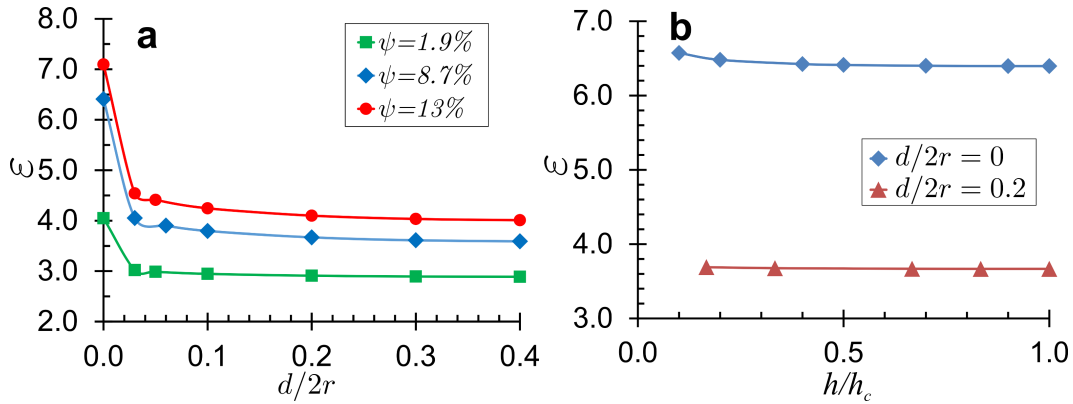


Figure 3.2: (a) Organizing the filler particles into a chainlike structure increases the relative permittivity ε . When the interparticle spacing $d/2r$ is increased, ε decreases and approaches the value for the composite that includes only randomly distributed particles. When $d/2r = 0$, the particles form continuous particle chains that enhance ε more than discontinuous chains do, which occurs when $d/2r > 0$. The larger the volume fraction θ , the higher ε is. The green squares, blue diamonds, and red circles correspond to $\psi = 1.9\%$, 8.7% , and 13% , respectively. (b) The clearance h has negligible influence on ε . The entire particle organization can be placed off-centre perpendicular to the plate without influencing ε . The clearance for particle organization that is centred between the two plates is h_c . The farther the ratio h/h_c is from unity, the more off-centre is the placement of the particle organization. Considering symmetry, results for $h/h_c \leq 1$ are presented for $\psi = 8.7\%$.

for both continuous and discontinuous chains, ε enhancement is independent of h .

Reducing a diminishes ε enhancement, as shown in Figure 3.3a. This result is counterintuitive with the general understanding that the capacitance, hence ε , should increase with decreasing distance between two conductive objects. However, the statement is only true for two conductive objects with equal and opposite charges (Haus and Melcher, 1989). Since each conductive chain herein has zero net charge, this leads to the different observed behaviour.

Essentially, for the same applied voltage, as a decreases, charge interactions between adjacent particle chains reduce the electric charges at the chain ends. This results in a lower overall capacitance and therefore smaller ε for the composite. Consider two continuous particle chains in a dielectric composite that are placed far enough to avoid long-range dipolar interactions (Gubin *et al.*, 2009). The electric charges induced by an applied voltage V at the two ends of each chain are $\pm Q_0$, which can be visualized by examining the distribution of surface charge density (Figure 3.3b–d). When the chains are moved closer, i.e., a is decreased, like charges located at the ends of the chains repel each other and migrate towards the middle of these chains. Here, charges from opposite ends of the chain intersperse and neutralize their polarity (green region in Figure 3.3c and d). The remaining charges at the two ends of each chain are now $\pm Q_1$ where $Q_1 < Q_0$, shown as the smaller and asymmetrical blue and purple (higher surface charge densities) regions in Figure 3.3d. For a capacitor of specific overall geometry and applied voltage, there is a proportional relationship between its electric charges $\int_v \rho_v dv = Q$ and ε , cf. Equation 3.1. Therefore, with decreasing a , charge interactions within the chains diminish

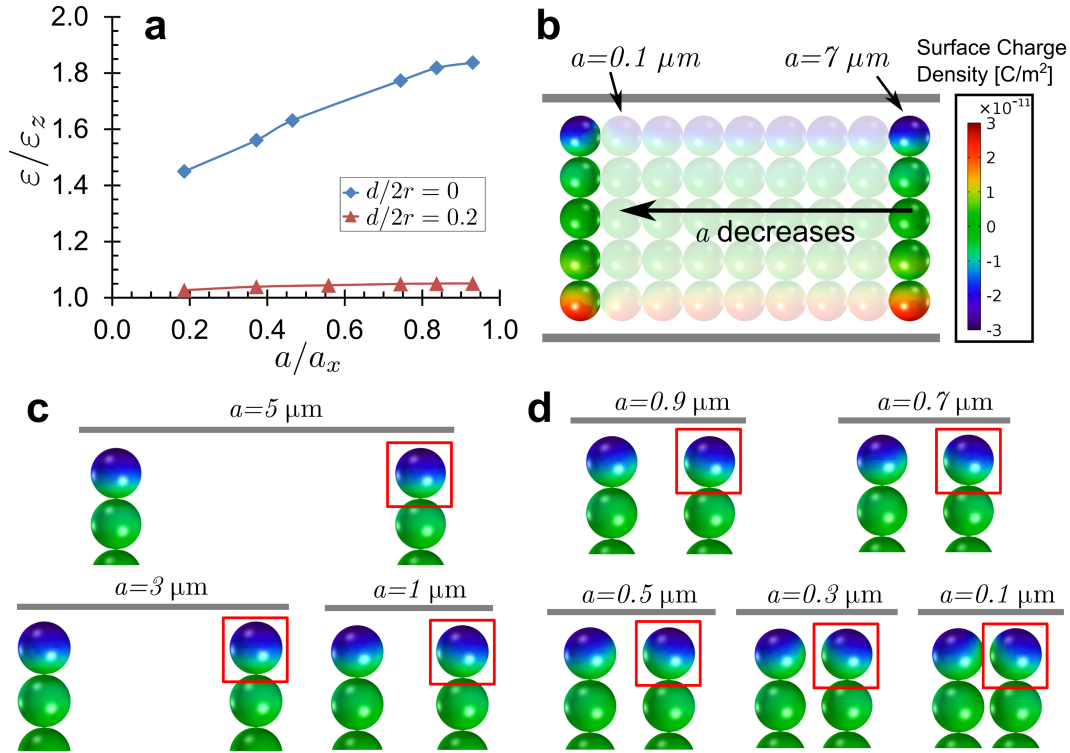


Figure 3.3: (a) Permittivity enhancement ϵ/ϵ_z increases with increasing interchain spacing a . When $a \approx a_x$, which is the maximum allowable value for a chainlike arrangement at any volume fraction, permittivity enhancement is largest. The distribution of the surface charge density in (b)-(d) shows that as a decreases, like charges at the ends of the particle chains are repelled towards the middle of the chains, which decreases the induced charges at chain ends, as illustrated by the smaller and non-symmetric blue and purple regions in (d). The smaller the induced charges, the lower the capacitance is, hence the smaller the relative permittivity.

the overall charge at their ends, diminishing ε enhancement, as shown in Figure 3.3a. Since a has the maximum value a_x for any ψ (see the supplementary material for details), Figure 3.3a also implies that when the particle chains are placed evenly with $a/a_x = 1$, ε enhancement is largest.

Increasing ψ increases ε . The ε enhancement is more significant for a composite containing continuous particle chains than one that includes randomly distributed particles (ε_z), as shown in Figure 3.4a. When $\psi < 9\%$, a composite containing smaller filler particles has higher ε than one containing larger particles, whereas when $\psi > 9\%$ the behaviour is opposite because chains formed with smaller particles have a greater overall surface area (Prateek *et al.*, 2016). In addition, the surface morphologies of the interfaces between the matrix and smaller filler particles are more intricate, leading to a higher interfacial polarization (Xu *et al.*, 2015; Yuan *et al.*, 2014), a size advantage that diminishes as ψ increases. Due to the competing influences of increasing ψ and charge interactions discussed above, a composite containing smaller particles has an inherently smaller a_x when $\psi > 9\%$, resulting in more vigorous charge interactions that decrease the ε enhancement.

For smaller ψ , a_x is larger so that interchain charge interactions are negligible. These interactions become stronger with increasing ψ for continuous particle chains regardless of particle size. Therefore, for organized particles, ε increases with ψ and a_x but the higher ψ is, the smaller a_x becomes whereas ε_z depends on ψ only. Consequently, there exists an optimal value of ψ for ε enhancement that maximizes the benefit of using organized particles as compared to simply distributing them randomly. The permittivity reaches a maximum value $\varepsilon/\varepsilon_z \approx 1.85$ for any particle size at an optimal ψ value, as shown in Figure 3.4b. For instance, when $r = 0.68 \mu\text{m}$, the maximum value of $\varepsilon/\varepsilon_z$

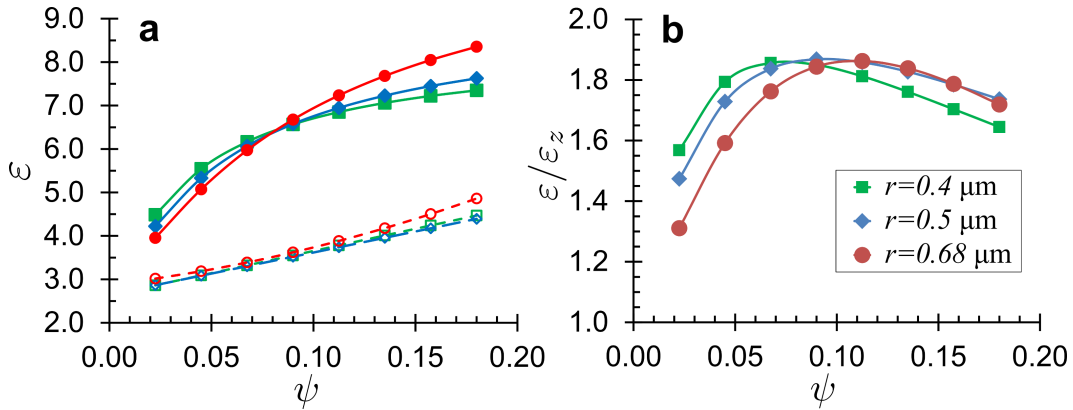


Figure 3.4: (a) When particles are arranged into continuous chains (solid lines) or distributed randomly (dashed lines), the relative permittivity ε increases with volume fraction ψ for all three particle sizes, $r = 0.4 \mu\text{m}$ (green squares), $0.5 \mu\text{m}$ (blue diamonds), and $0.68 \mu\text{m}$ (red circles). ε is higher when particles form continuous chains, i.e., $d/2r = 0$. When the particles are randomly distributed, ε is smaller. For smaller particles (green squares), ε is higher when $\psi < 9\%$, but this size advantage diminishes as ψ increases. This is because, when $\psi > 9\%$, charge interactions between adjacent chains that contain smaller particles are stronger than for chains with larger particles, which diminishes ε enhancement. (b) The ε enhancement for composites that have filler particle organizations is compared with counterparts containing randomly distributed particles ε_z . Maximum enhancement occurs at $\psi = 7\%$, 9% , and 11% for particle radii $r = 0.4 \mu\text{m}$, $0.5 \mu\text{m}$, and $0.68 \mu\text{m}$, respectively. This figure demonstrates that organized particle arrangements are more beneficial than randomly distributed filler particles for permittivity enhancement.

occurs at $\psi = 11\%$ while the maxima for $r = 0.4 \mu\text{m}$ and $0.5 \mu\text{m}$ lie at $\psi = 7\%$ and 9% , respectively.

The particle chains discussed above are straight and aligned ($\theta = 0^\circ$) with overall chain directions perpendicular to the conductive plates. In Figure 3.5, we demonstrate the influence of $\theta = 0^\circ$ to 60° and ψ on ε for $r = 0.5 \mu\text{m}$. For continuous particle chains (Figure 3.5a), ε decreases with increasing θ and even more rapidly with increasing ψ . Without varying the number of particles in a chain, the larger θ is, the closer are the particles within a chain. Since the electric potential over the entire surface of the chain is the same, for a chain that is oriented perpendicular to the equipotential surfaces, the closer the particles are, the lower is the distortion of the equipotential surfaces. This leads to smaller electric field strengths and therefore smaller ε for the composite. For discontinuous chains, ε is more or less independent of θ , as shown in Figure 3.5b, the largest difference in ε being 0.265. Hence, through various combinations of ψ and θ for the same matrix and filler material, it is possible to design elastomer-particle composites with ε in the range from 3 to 8 (Figure 3.5c).

3.4 Conclusion

In summary, the manner in which conductive filler particles contained within a PDMS elastomeric matrix are arranged influences the electric permittivity of the composite material. Organizing the particles into chainlike structures enhances the bulk permittivity by 85% in comparison with that for a composite containing the same filler, but which is randomly distributed. The value of ψ that is most beneficial when organized particles are used is $9\% \pm 2\%$.

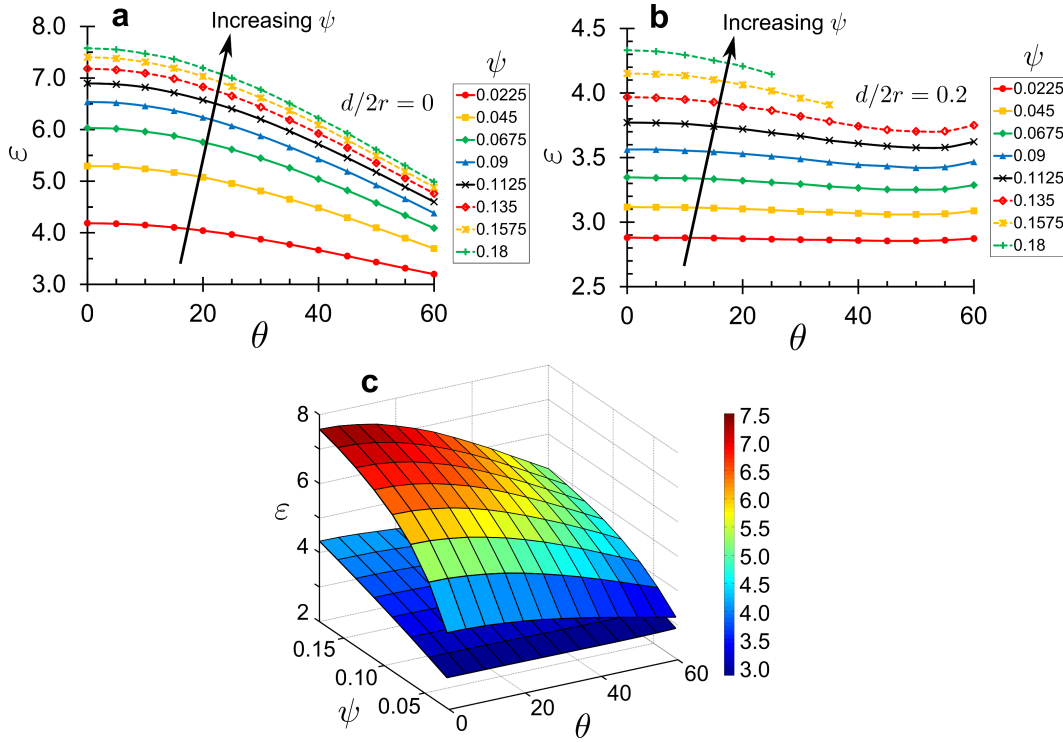


Figure 3.5: Relative permittivity ε as a function of zigzag angle θ and volume fraction ψ for (a) continuous chains ($d/2r = 0$) and (b) discontinuous chains ($d/2r = 0.2$), both composed of particles with radius $r = 0.5 \mu\text{m}$. For continuous chains, ε decreases with increasing θ . The larger ψ is, the greater is the decrease in ε . For $d/2r = 0.2$, as shown in (b), θ has negligible effect on ε with the largest difference in ε being 0.265. (c) Surface plot of ε , ψ , and θ for $r = 0.5 \mu\text{m}$. The top surface corresponds to the results for $d/2r = 0$ whereas that on the bottom is for $d/2r = 0.2$. The same overall behaviour is observed, irrespective of the constituent particle size. (See supplementary material for the corresponding figures for $r = 0.4 \mu\text{m}$ and $0.68 \mu\text{m}$.)

The bulk permittivity increases with increasing ψ and $a_{(x)}$, but decreases with increasing d and θ . When $\psi < 9\%$, a composite containing smaller particles has higher ε , while for $\psi > 9\%$, introduction of larger particles increases ε . The enhancement in ε is more gradual beyond $\psi \approx 9\%$ due to the competition between effects induced by increasing ψ , which increases ε , and decreasing a_x , which decreases ε . When adjacent particles are interconnected, ε enhancement is more pronounced because continuous particle chains that are oriented perpendicular to the equipotential surfaces increase the induced charge of the composite, hence its bulk permittivity. These results are relevant for the design of soft dielectric materials with different permittivities when identical material compositions are used but their filler particles morphologies are varied, such as for additive manufacturing flexible electronics and 3D printed circuits.

3.5 Acknowledgements

This work was supported by a Discovery Grant from the Natural Sciences and Engineering Research Council of Canada (NSERC) under grant number RGPIN-2014-04066, and the Mitacs Globalink program.

3.6 Supporting Information

3.6.1 Model Verification

A simulation using pure PDMS as the dielectric medium confirms that the simulated relative permittivity is consistent with $\varepsilon_r \approx 2.69$ obtained from the literature (Trajkovikj *et al.*, 2012). Then, pure PDMS is replaced by a

PDMS-conductive particle composite, containing randomly distributed conductive particles, as the dielectric medium in the simulated capacitor. Here, the filler particles assumed to be uniform size spheres are individually placed at specific coordinates generated by a random number generator. After verifying our model, we organize these conductive particles into different chain-like structures.

We perform the simulations that consist of the dielectric composite with PDMS matrix and randomly distributed conductive spheres and compare the results with several analytical models, including Maxwell model (Barber *et al.*, 2009), Bruggeman model (Barber *et al.*, 2009), Lichtenecker's equation (Ponnamma *et al.*, 2016), and Jayasundere-Smith equation (Ponnamma *et al.*, 2016). They use mixing rules (Barber *et al.*, 2009; Ponnamma *et al.*, 2016), mean field theory (Barber *et al.*, 2009), or effective medium theory (Ponnamma *et al.*, 2016) to determine the effective relative permittivity ε_{eff} of the composites. The Maxwell model assumes a single spherical inclusion embedded in a continuous polymer matrix (Barber *et al.*, 2009), which is

$$\varepsilon_{eff} = \varepsilon_m \frac{\varepsilon_f + 2\varepsilon_m - 2\psi(\varepsilon_m - \varepsilon_f)}{\varepsilon_f + 2\varepsilon_m + \psi(\varepsilon_m - \varepsilon_f)}, \quad (3.3)$$

where ε_m and ε_f denote the relative permittivity of the matrix and filler, respectively, and ψ the filler volume fraction. The Bruggeman model assumes multiple spherical inclusions instead of a single inclusion and expresses as (Barber *et al.*, 2009)

$$(1 - \psi) \left(\frac{\varepsilon_m - \varepsilon_{eff}}{\varepsilon_m + 2\varepsilon_{eff}} \right) + \psi \left(\frac{\varepsilon_f - \varepsilon_{eff}}{\varepsilon_f + 2\varepsilon_{eff}} \right) = 0, \quad (3.4)$$

Lichtenecker uses logarithmic law of mixing and considers spheroids fillers that are randomly oriented and uniformly distributed in a continuous matrix (Ponnamma *et al.*, 2016).

$$\ln \varepsilon_{eff} = (1 - \psi) \ln \varepsilon_m + \psi \ln \varepsilon_f. \quad (3.5)$$

Jayasundere-Smith equation includes the interaction between neighbouring spheres and is (Ponnamma *et al.*, 2016)

$$\varepsilon_{eff} = \frac{\varepsilon_m (1 - \psi) + \varepsilon_f \psi \left[\frac{3\varepsilon_m}{\varepsilon_f + 2\varepsilon_m} \right] \left[1 + \left(\frac{3\psi(\varepsilon_f - \varepsilon_m)}{\varepsilon_f + 2\varepsilon_m} \right) \right]}{(1 - \psi) + \psi \left[\frac{3\varepsilon_m}{\varepsilon_f + 2\varepsilon_m} \right] \left[1 + \left(\frac{3\psi(\varepsilon_f - \varepsilon_m)}{\varepsilon_f + 2\varepsilon_m} \right) \right]} \quad (3.6)$$

All these models are often used to predict the ε_{eff} of the dielectric composite comprised of polymer matrix and homogeneous filler particles. Since there is no specific characteristic of filler organization involved in these models, we verify our simulation results for composite with randomly distributed particles using these equations. Our results show a good agreement with the Maxwell model for $\psi \leq 11\%$ and fall between the Jayasundere-Smith equation and the Maxwell model for $\psi > 11\%$, as shown in Figure 3.6.

3.6.2 Determination of a_x

The interchain spacing a is normalized by its maximum value a_x at the corresponding volume fraction. a_x depends on ψ and is determined by considering the average material volume occupied per chain—the total material volume divided by the number of particle chains that lie perpendicular to the plates. The average volume belongs to a chain is equivalent to a square prism of length a_x

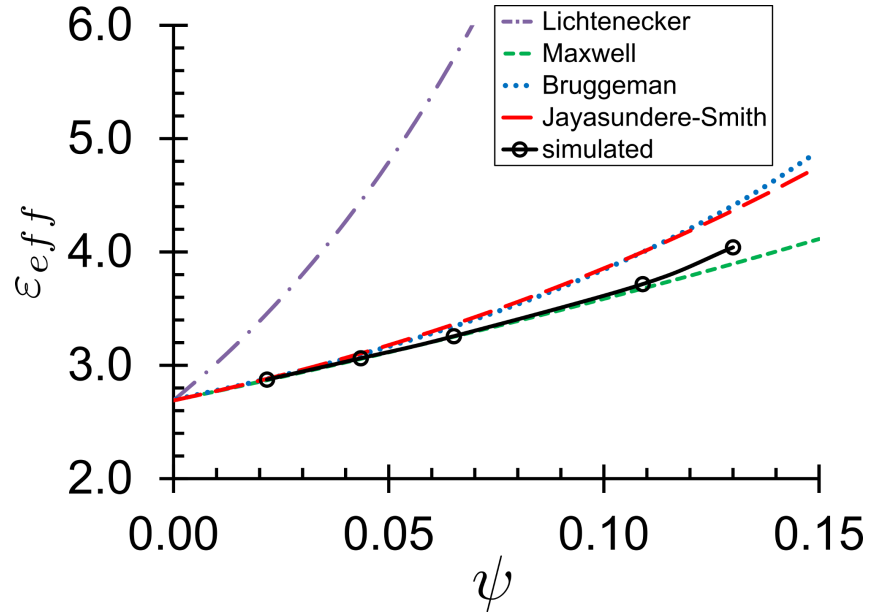


Figure 3.6: The simulated results of effective relative permittivity ε_{eff} agree with the Maxwell model for volume fraction ψ up to 11%. For $\psi > 11\%$, the results fall between the Jayasundere-Smith equation and the Maxwell model.

and height L . The corresponding a_x for any ψ is

$$a_x = \sqrt{\frac{4\pi r^3 n}{3\psi L}} - 2r, \quad (3.7)$$

where n denotes the number of particles in a chain. The normalized interchain spacing a/a_x has its value ranging from 0 to 1. The smaller the value, the closer the chains lie to one another within the filler structure and hence the higher the heterogeneity in the filler distribution. When $a/a_x = 1$, the filler structure (particle chains) occupies the entire composite evenly.

3.6.3 Results for zigzag configurations with varying particle sizes

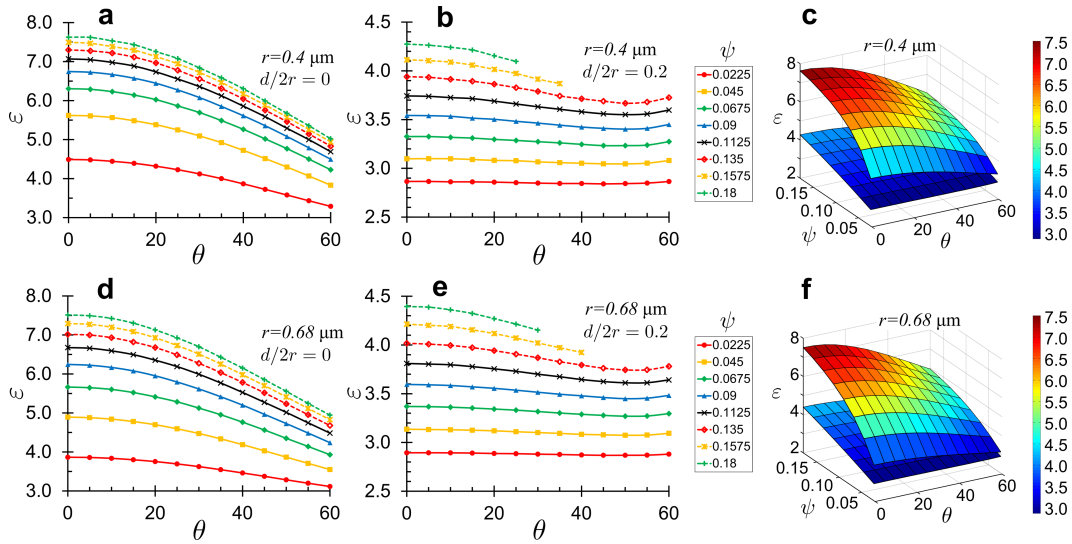


Figure 3.7: The overall behaviours of the relative permittivity ε for (a)-(c) $r = 0.4 \mu\text{m}$ and (d)-(f) $r = 0.68 \mu\text{m}$ are similar, but differ slightly in magnitude. For continuous chains, $d/2r = 0$, ε decreases with increasing zigzag angle θ , as shown in (a) and (d). The larger the volume fraction ψ , the larger the reduction in ε . When the interparticle spacing $d/2r = 0.2$, θ has negligible effect on ε , as shown in (b) and (e). The largest differences in ε for each ψ are 0.273 and 0.290, respectively. Surface plots of ε , θ , and ψ for chains with interparticle spacing $d/2r = 0$, and 0.2 are presented in (c) and (f). The top surface in each plot corresponds to a chain with $d/2r = 0$ whereas that on the bottom is for $d/2r = 0.2$. The same overall behaviour is observed for each type of chain, irrespective of its constituent particle size.

Bibliography

- Abdel Fattah, A. R., Ghosh, S., and Puri, I. K. (2016a). Printing microstructures in a polymer matrix using a ferrofluid droplet. *J. Magn. Magn. Mater.*, **401**, 1054–1059.
- Abdel Fattah, A. R., Ghosh, S., and Puri, I. K. (2016b). Printing Three-Dimensional Heterogeneities in the Elastic Modulus of an Elastomeric Matrix. *ACS Appl. Mater. Interfaces*, **8**(17), 11018–11023.
- Alger, M. (1996). *Polymer science dictionary*. Springer Science & Business Media.
- Barber, P., Balasubramanian, S., Anguchamy, Y., Gong, S., Wibowo, A., Gao, H., Ploehn, H. J., and zur Loye, H.-C. (2009). Polymer Composite and Nanocomposite Dielectric Materials for Pulse Power Energy Storage. *Materials*, **2**(4), 1697–1733.
- Borbáth, T., Günther, S., Yu Borin, D., Gundermann, T., and Odenbach, S. (2012). X μ CT analysis of magnetic field-induced phase transitions in magnetorheological elastomers. *Smart Mater. Struct.*, **21**(10), 105018.
- Boudenne, A., Mamunya, Y., Levchenko, V., Garnier, B., and Lebedev, E.

- (2015). Improvement of thermal and electrical properties of Silicone–Ni composites using magnetic field. *Eur. Polym. J.*, **63**, 11–19.
- Brochu, P. and Pei, Q. (2010). Advances in dielectric elastomers for actuators and artificial muscles. *Macromol. Rapid Commun.*, **31**(1), 10–36.
- Collino, R. R., Ray, T. R., Fleming, R. C., Sasaki, C. H., Haj-Hariri, H., and Begley, M. R. (2015). Acoustic field controlled patterning and assembly of anisotropic particles. *Extrem. Mech. Lett.*, **5**, 37–46.
- Coquelle, E. and Bossis, G. (2005). Magnetostriction and piezoresistivity in elastomers filled with magnetic particles. *J. Adv. Sci.*, **17**(1/2), 132–138.
- Frutiger, A., Muth, J. T., Vogt, D. M., Mengüç, Y., Campo, A., Valentine, A. D., Walsh, C. J., and Lewis, J. A. (2015). Capacitive Soft Strain Sensors via Multicore-Shell Fiber Printing. *Adv. Mater.*, **27**(15), 2440–2446.
- Ganguly, R. and Puri, I. K. (2007). Field-Assisted Self-Assembly of Superparamagnetic Nanoparticles for Biomedical, MEMS and BioMEMS Applications. In *Adv. Appl. Mech.*, volume 41, pages 293–335.
- Ge, J., He, L., Hu, Y., and Yin, Y. (2011). Magnetically induced colloidal assembly into field-responsive photonic structures. *Nanoscale*, **3**(1), 177–183.
- Ghosh, S. and Puri, I. K. (2013). Soft polymer magnetic nanocomposites: microstructure patterning by magnetophoretic transport and self-assembly. *Soft Matter*, **9**, 2024–2029.

- Ghosh, S. and Puri, I. K. (2015). Changing the magnetic properties of microstructure by directing the self-assembly of superparamagnetic nanoparticles. *Faraday Discuss.*, **181**, 423–435.
- Ghosh, S., Tehrani, M., Al-haik, M. S., and Puri, I. K. (2015). Patterning the Stiffness of Elastomeric Nanocomposites by Magnetophoretic Control of Cross-linking Impeder Distribution. *Materials*, **8**, 474–485.
- Gubin, S. P., Khomutov, G. B., and Koksharov, Y. A. (2009). Organized Ensembles of Magnetic Nanoparticles: Preparation, Structure, and Properties. In S. P. Gubin, editor, *Magn. Nanoparticles*, pages 117–195. Wiley-VCH Verlag GmbH & Co. KGaA, Weinheim, Germany.
- Guffey, M. J. and Scherer, N. F. (2010). All-optical patterning of Au nanoparticles on surfaces using optical traps. *Nano Lett.*, **10**(11), 4302–4308.
- Han, Y., Hong, W., and Faidley, L. E. (2013). Field-stiffening effect of magneto-rheological elastomers. *Int. J. Solids Struct.*, **50**(14-15), 2281–2288.
- Haus, H. A. and Melcher, J. R. (1989). Electroquasistatic Fields in the Presence of Perfect Conductors. In *Electromagn. Fields Energy*, chapter 4.6. Prentice-Hall, Englewood Cliffs, NJ.
- Juskey, F., Suppelsa, A., and Dorinski, D. (1993). Method of forming a three-dimensional printed circuit assembly.
- Klimchitskaya, G. L., Mohideen, U., and Mostepanenko, V. M. (2009). The Casimir force between real materials: Experiment and theory. *Rev. Mod. Phys.*, **81**(4), 1827–1885.

- Muth, J. T., Vogt, D. M., Truby, R. L., Mengüç, Y., Kolesky, D. B., Wood, R. J., and Lewis, J. A. (2014). 3D Printing: Embedded 3D Printing of Strain Sensors within Highly Stretchable Elastomers. *Adv. Mater.*, **26**(36), 6202–6202.
- Pickles, A. J. and Steer, M. B. (2013). Effective permittivity of 3-d periodic composites with regular and irregular inclusions. *IEEE Access*, **1**, 523–536.
- Ponnamma, D., Kishor Kumar Sadasivuni, C. W., Thomas, S., and Al-Ma'adeed, M. A.-A. (2016). *Flexible and Stretchable Electronic Composites*. Springer Series on Polymer and Composite Materials. Springer International Publishing, Cham.
- Prateek, Thakur, V. K., and Gupta, R. K. (2016). Recent Progress on Ferroelectric Polymer-Based Nanocomposites for High Energy Density Capacitors: Synthesis, Dielectric Properties, and Future Aspects. *Chem. Rev.*, **116**(7), 4260–4317.
- Schmidt, H. F., Rauchmaul, S., and Bednarz, J. (1991). Three-dimensional printed circuit board.
- Siegel, A. C., Phillips, S. T., Dickey, M. D., Lu, N., Suo, Z., and Whitesides, G. M. (2010). Foldable printed circuit boards on paper substrates. *Adv. Funct. Mater.*, **20**(1), 28–35.
- Stoyanov, H., Kollosche, M., Risse, S., McCarthy, D. N., and Kofod, G. (2011). Elastic block copolymer nanocomposites with controlled interfacial interactions for artificial muscles with direct voltage control. *Soft Matter*, **7**(1), 194–202.

- Sun, Z. Z., Lopez, A., and Schliemann, J. (2011). Zero-field magnetization reversal of two-body Stoner particles with dipolar interaction. *J. Appl. Phys.*, **109**(10), 104303.
- Trajkovicj, J., Zurcher, J.-F., and Skrivervik, A. K. (2012). Soft and flexible antennas on permittivity adjustable PDMS substrates. In *2012 Loughbrgh. Antennas Propag. Conf.*, number November, pages 1–4. IEEE.
- Truby, R. L. and Lewis, J. A. (2016). Printing soft matter in three dimensions. *Nature*, **540**(7633), 371–378.
- Tsai, P. J., Ghosh, S., Wu, P., and Puri, I. K. (2016). Tailoring Material Stiffness by Filler Particle Organization. *ACS Appl. Mater. Interfaces*, **8**(41), 27449–27453.
- Tseng, A. A., Chen, K., Chen, C. D., and Ma, K. J. (2003). Electron beam lithography in nanoscale fabrication: Recent development. *IEEE Trans. Electron. Packag. Manuf.*, **26**(2), 141–149.
- van Enk, S. (1995). The Casimir Effect in Dielectrics. *J. Mod. Opt.*, **42**(2), 321–338.
- Xu, N., Hu, L., Zhang, Q., Xiao, X., Yang, H., and Yu, E. (2015). Significantly Enhanced Dielectric Performance of Poly(vinylidene fluoride-co-hexafluoropylene)-based Composites Filled with Hierarchical Flower-like TiO₂ Particles. *ACS Appl. Mater. Interfaces*, **7**(49), 27373–27381.
- Young, R. J. and Lovell, P. A. (2011). *Introduction to polymers*. CRC press.
- Yuan, J., Yao, S., Li, W., Sylvestre, A., and Bai, J. (2014). Vertically Aligned Carbon Nanotube Arrays on SiC Microplatelets: A High Figure-of-Merit

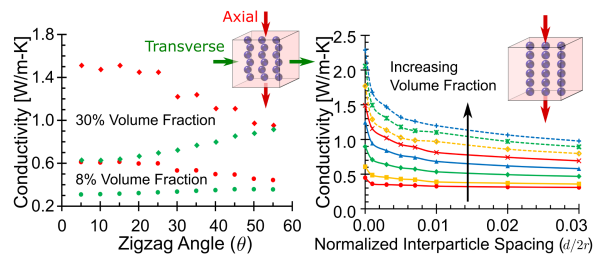
Strategy for Achieving Large Dielectric Constant and Low Loss in Polymer Composites. *J. Phys. Chem. C*, **118**(40), 22975–22983.

Chapter 4

Tailoring Anisotropic Thermal Conductivity by Varying Particle Organization in Nickel-PDMS Composites^{1,2}

Abstract

Anisotropic properties can be imparted to composite materials by arranging filler particles along specific directions inside the polymer matrix. Using finite element



¹Authors: Peiyang J. Tsai, Souvik Pal, Suvojit Ghosh, Ishwar K. Puri

²The content of this chapter has been submitted to Composites Science and Technology on March 13, 2017.

analysis, we explore how chainlike particle arrangements modify the bulk thermal conductivity. Both the axial and transverse conductivities increase with increasing filler volume fraction, but while the former decreases with increasing interparticle spacing the latter remains uninfluenced. Increasing the interparticle zigzag angle decreases axial conductivity and increases transverse conductivity. An empirical model that includes effects of interparticle spacing and zigzag angle is developed to predict the anisotropic thermal conductivity of a composite that contains particle chains.

4.1 Introduction

While many materials that are produced through additive manufacturing have isotropic material properties (Richter and Lipson, 2011), applications such as flexible electronics (Siegel *et al.*, 2010) and bionic devices (Kong *et al.*, 2016; Compton and Lewis, 2014) require anisotropic and heterogeneous properties. As another example, directional thermal conductivity gradients are used to remove heat in electronic devices along specific directions to prevent local hot spots (Yuan *et al.*, 2016). Directional, or anisotropic, properties can be introduced into a composite material by inserting and arranging appropriate filler particles in specific patterns inside a polymer matrix (Boudenne *et al.*, 2015; Gaska *et al.*, 2015; Goc *et al.*, 2016; Yuan *et al.*, 2015).

There are numerous ways by which such an organization can be remotely directed. Starting with a liquid polymer-particle mixture, suspended particles can be assembled as desired by applying external electric (Zhu *et al.*, 2009), magnetic (Abdel Fattah *et al.*, 2016; Ghosh and Puri, 2013; Ghosh *et al.*, 2015; Kokkinis *et al.*, 2015), or acoustic (Collino *et al.*, 2015) fields. Doing so enables

a “material printer” (Ghosh *et al.*, 2015) that manufactures materials additively with strategically engineered anisotropies, for instance, in mechanical stiffness (Tsai *et al.*, 2016; Han *et al.*, 2013), magnetic susceptibility (Ghosh and Puri, 2015), and thermal (Dallas *et al.*, 2006) and electrical conductivities (Fragouli *et al.*, 2014).

The most common form of field-assisted particle assembly in a polymer matrix is a chainlike structure (Boudenne *et al.*, 2015; Gaska *et al.*, 2015; Goc *et al.*, 2016; Yuan *et al.*, 2015), examples for which include straight or zigzag (i.e., wavy) chains (Han *et al.*, 2013; Borbáth *et al.*, 2012; Coquelle and Bossis, 2005). Control over particle organization is exercised by enhancing the field strength, which improves particle alignment (Goc *et al.*, 2016; Collino *et al.*, 2015; Borbáth *et al.*, 2012; Wang *et al.*, 2009) and reduces the spacing between adjacent particles (Wang *et al.*, 2009), thus producing straighter and tighter chains. While previous investigations have described the influence of homogeneously dispersed filler particles on bulk composite properties (Kumlutas and Tavman, 2006; Ngo *et al.*, 2016; Khan *et al.*, 2016), the effect of non-homogeneous, or anisotropic, arrangements on these properties is far less understood (Boudenne *et al.*, 2015; Goc *et al.*, 2016; Tsai *et al.*, 2016; Fragouli *et al.*, 2014), particularly regarding the thermal properties of composite materials. Existing models only predict the isotropic thermal conductivity of a composite as a function of the filler volume fraction (Kumlutas and Tavman, 2006; Ngo *et al.*, 2016), ignoring effects due to specific anisotropic filler arrangements.

Here, we examine the influence of anisotropic filler particle organization on the bulk thermal conductivity of an elastomeric composite through finite element analysis. Unlike typical experiments, numerical simulations make it

possible to investigate composites that include particles that are organized with repeatable precision. We characterize a chainlike structure through an overall orientation n , uniform spherical particle radius r , interparticle spacing d , and internal zigzag angle θ , as shown in Figure 4.1. The angle θ lies between n and the centre-to-centre direction of two adjacent particles, which is between 0 – 60° in the simulations. When $\theta = 0^\circ$, the consequence is a straight chain with all of its particles perfectly aligned along n (Figure 4.1a). When $0^\circ < \theta < 60^\circ$, these particles are organized in the form of a zigzag chain (Figure 4.1b). This quasi one-dimensional chainlike particle organization introduces an anisotropic bulk thermal conductivity. While measurements confirm that the axial thermal conductivity is larger than the transverse conductivity (Boudenne *et al.*, 2015; Gaska *et al.*, 2015; Goc *et al.*, 2016), there is no valid model that precisely describes this behaviour in terms of important microstructural parameters, such as d and θ , which represent particular chain arrangements. To focus on the effects of d , θ , and filler volume fraction ψ on the effective thermal conductivity of the composite, we assume that the particles are of uniform radius, and omit the interfacial thermal resistance between filler particles and the surrounding matrix by assuming perfect thermal contact (Ngo and Byon, 2016; Hull and Clyne, 1996).

4.2 Materials and Methods

The effective thermal conductivities, k_a along n , and k_t along the transverse direction of n , both shown in Figure 4.1, are numerically simulated using the ABAQUS finite element package. Uniform high and low temperatures,

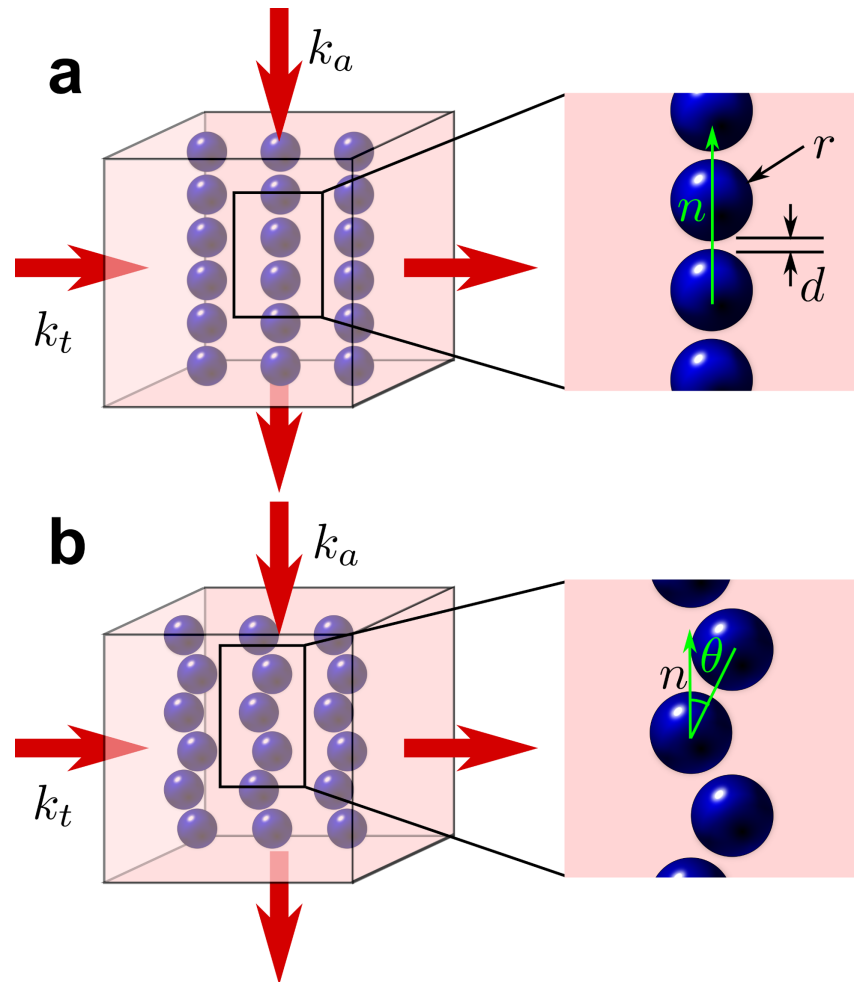


Figure 4.1: Uniform size spherical filler particles of radius r are organized into chainlike structures in a polymer matrix to investigate their influence on the material bulk thermal conductivity in the axial (k_a) and transverse (k_t) directions. (a) Particles are organized into straight chains along n and the interparticle spacing d is varied. (b) Particles are arranged into zigzag chains where the zigzag angle θ is varied.

$T_h = 50^\circ\text{C}$ and $T_c = 20^\circ\text{C}$, are applied on the two opposite surfaces of a representative volume element (RVE) whereas the other four orthogonal surfaces are adiabatic, i.e., perfectly insulated (Kumrlutas and Tavman, 2006; Ngo and Byon, 2016; Li *et al.*, 2013; Ramani and Vaidyanathan, 1995). At steady state, the effective thermal conductivity of the composite in a particular direction is determined using Fourier's heat conduction law,

$$q = -k(dT/dx) \approx -k(\Delta T/\Delta x), \quad (4.1)$$

where q denotes the heat flux obtained from the simulations, k the effective thermal conductivity of the composite, ΔT the temperature difference across the surfaces of the RVE, and Δx the length of the RVE along the direction of heat transfer. The bulk thermal conductivities of nickel (91 W/m-K) (Boudenne *et al.*, 2015) and polydimethylsiloxane (PDMS) (0.25 W/m-K) (Boudenne *et al.*, 2015) are assumed for the particles ($r = 5.7 \mu\text{m}$) and the matrix, respectively. While these two materials are chosen due to their wide use (Ngo and Byon, 2016), our approach and results are applicable to other polymer composites containing conductive filler particles. The simulation results for randomly distributed particles are verified with previous empirical models (Boudenne *et al.*, 2015; Kumrlutas and Tavman, 2006; Ngo *et al.*, 2016; Ngo and Byon, 2016), as shown in Figure 4.2a. (Details of the simulation approach and its verification are provided in the supporting information.)

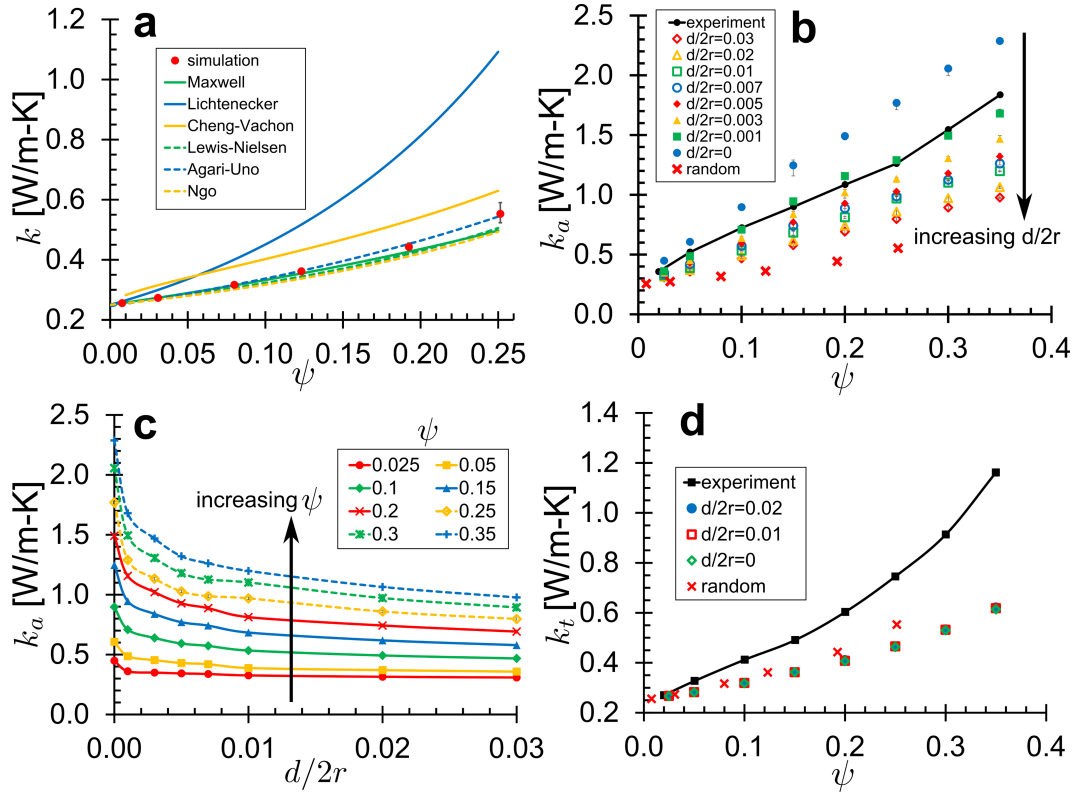


Figure 4.2: (a) Simulation results for randomly distributed particles in the polymer matrix are compared with previous models for $k_m = 0.25$ W/m-K and $k_f = 91$ W/m-K. The Agari-Uno model (Kumlutas and Tavman, 2006) provides the best fit with the simulations due to the fitting of its constants. (b)-(c) When filler particles are arranged into straight chains aligned along n , k_a increases linearly with increasing ψ but shows an exponential decrease with increasing normalized interparticle spacing $d/2r$. (d) There is negligible influence of $d/2r$ on k_t . For $\psi < 0.2$, k_t behaves in a manner similar to that of randomly distributed particles, but becomes smaller for $\psi > 0.2$. Experimental results (Boudenne *et al.*, 2015) for k_a are in closer agreement with simulations for $d/2r = 0.001$, implying that particles are not fully connected. For k_t , the higher experimentally measured values may arise to the side branching of chains (Boudenne *et al.*, 2015), while the simulations consider uniaxial chains. The “random” cases in (b) and (d) represent simulations with randomly distributed particles.

4.3 Results and Discussion

When filler particles are aligned in a chain along n , k_a increases linearly with increasing ψ (Figure 4.2b), which is expected from mixture theory, i.e., the larger the value of ψ the more conductive particles there are in the composite, which increases the effective conductivity (Kumrlutas and Tavman, 2006). Moreover, straight chains with negligible normalized interparticle distance $d/2r$ create more favourable thermally conducting paths, leading to higher k_a . Previous measurements of k_a for $r \approx 5 \mu\text{m}$ (Boudenne *et al.*, 2015), also included in Figure 4.2b, are in agreement with the quantitative and qualitative values for $d/2r = 0.001$ with respect to increasing ψ . This suggests that the filler particles in the experiments are not perfectly connected end to end but include small interparticle spacing (Wang *et al.*, 2009). Increasing $d/2r$ increases the proportion of lower thermal conductivity elastomer contained between adjacent particles along n in the heat transfer path, leading to higher overall thermal resistance and its subsequent saturation. Consequently, k_a decreases exponentially, as shown in Figure 4.2c. Variations in $d/2r$ have a negligible influence on k_t (Figure 4.2d) since that effect occurs in a direction perpendicular to that of heat transfer. The corresponding measured conductivities (Boudenne *et al.*, 2015) are higher than our predictions, which we attribute to side branching of particle chains (Boudenne *et al.*, 2015), and nonuniform particle sizes and shapes (Goc *et al.*, 2016) in the experiments.

For zigzag chains, k_a decreases and approaches a minimum value as θ increases to $\approx 55^\circ$, (Figure 4.3a) whereas k_t increases congruently and approaches a maximum value (Figure 4.3b). These effects are more prominent at higher ψ . Considering k_a , the overall heat transfer direction is parallel to

the overall chain orientation with the local heat flow being conducted through adjacent high conductivity particles that are interconnected within the low conductivity polymer matrix. Increasing θ lengthens the local heat transfer path, increasing the thermal resistance, thus decreasing k_a . In contrast, the heat transfer path perpendicular to a chain crosses over a single conductive particle per straight chain ($\theta = 0^\circ$) while for a zigzag chain this path crosses additional adjacent particles with increasing θ , thereby decreasing the thermal resistance and increasing k_t . This latter conductivity enhancement becomes more prominent at higher ψ and θ as more particles become involved in the transverse heat transfer path.

We have shown how the anisotropic thermal conductivity of a composite can be influenced by ψ , $d/2r$ and θ . However, the latter two characteristics have not been previously considered in theoretical and empirical models to predict the effective thermal conductivity of a particle-polymer composite. Based on the simulations, we propose a modified model that incorporates $d/2r$ and θ into the general Lewis and Nielsen (LN) model. Although the Agari-Uno (A-U) model has the best fit in the simulations for randomly distributed particles because of how its constants are fitted, unlike the A-U model the LN model also considers the geometry of filler particles, direction of heat flow, and maximum filler packing fraction (Kumrlutas and Tavman, 2006; Nielsen and Landel, 1994). With the LN model,

$$k_c = k_m \left(\frac{1 + AB\psi}{1 - B\psi C} \right), \text{ where} \quad (4.2)$$

$$B = \frac{(k_f/k_m) - 1}{(k_f/k_m) + A} \text{ and } C = 1 + \left(\frac{1 - \phi_m}{\phi_m^2} \right) \psi, \quad (4.3)$$

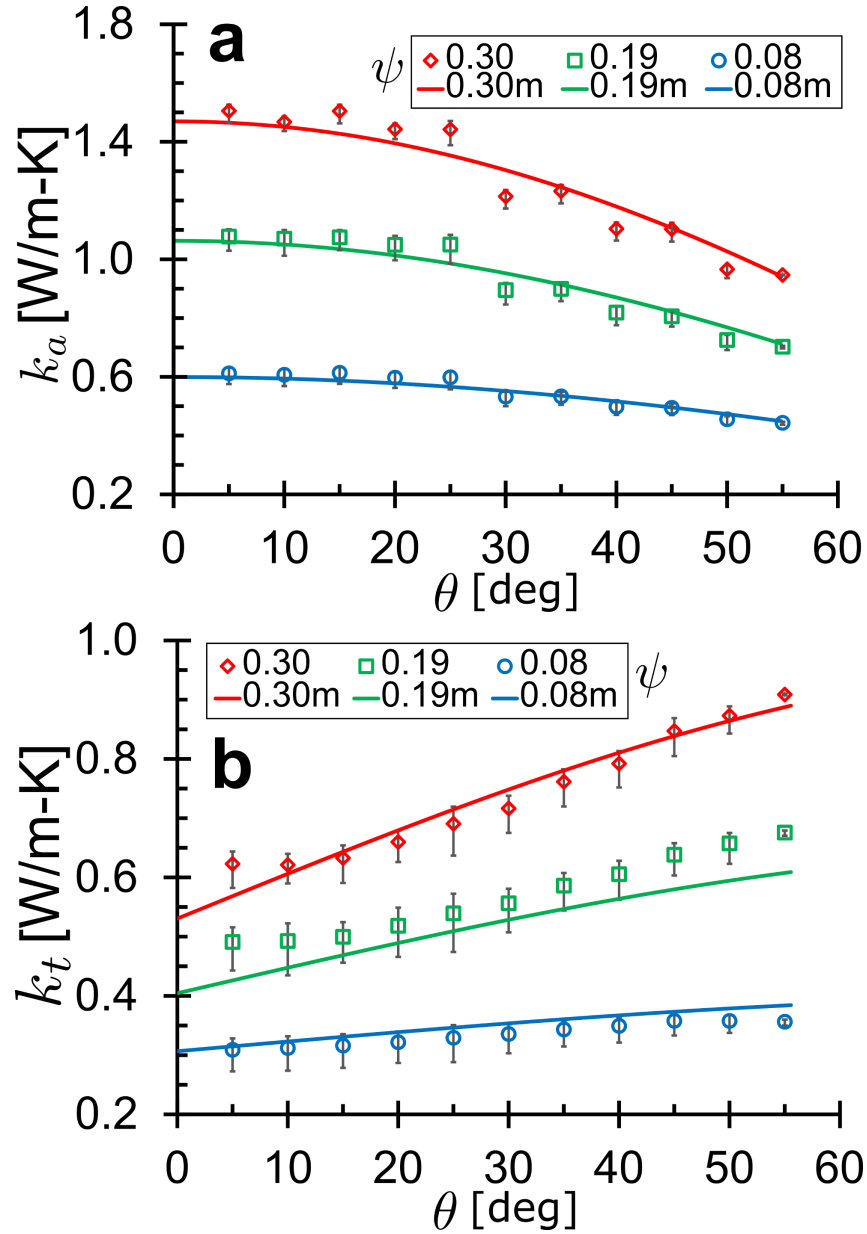


Figure 4.3: For zigzag chains, k_a decreases with increasing θ and reaches a minimum value when $\theta \approx 55^\circ$, while the transverse conductivity k_t increases with increasing θ . The effect of θ becomes more pronounced for higher ψ , which enables granular control over the thermal conductivity of a composite. Solid lines represent fits with the modified models that we have proposed, i.e., with the sinusoidal functions $f(\cos(\theta))$ for k_a and $f(\sin(\theta))$ for k_t . Overall, the models are in good agreement with the simulations (depicted by the symbols).

and k_c , k_m , and k_f denote the thermal conductivities of the composite, matrix, and filler, respectively. The constant A depends on the filler geometry and heat transfer direction while ϕ_m represents the maximum filler packing fraction. Since, for chainlike structures, the packing fraction of the filler is its volume fraction, the maximum possible particle volume fraction in a simple cube $\phi_m = 0.524$ is assumed to occur when there is no spacing between chains. (Details of the calculations are provided in the supporting information.)

To accommodate the influence of particle chains, we propose the modification,

$$k_c = k_m \left(\frac{1 + AB\psi D_2 D_3}{1 - B\psi C D_1} \right), \quad (4.4)$$

where D_1 accounts for the nature of packing and chain direction, D_2 the inter-particle spacing, and D_3 zigzag angle. An exponential function is used for D_2 to best represent the exponential decay of k_a with $d/2r$ (Figure 4.2c), while sinusoidal functions are employed for D_3 to represent θ . The values and expressions for A , D_1 , D_2 and D_3 are listed in Table 4.1, where the constants are obtained by fitting Equation 4.4 to our simulation results. Results using this relation, presented by solid lines in Figure 4.3, are in good agreement with our simulations, which are depicted by symbols. Since the above modification is generic, it is suitable for predicting the axial and transverse thermal conductivities of particulate-reinforced polymer composite. Hence, values of the constants in Table 4.1 for this specific problem can be also obtained for other material combinations using the same methodology.

Equation 4.4 is used to determine the equivalent values of $d/2r$ and θ for the chainlike structures contained in the particle-polymer composite samples used in experiments. The simulation results $d/2r = 0.001$ for $\theta = 0^\circ$ in Figure 4.2b

Table 4.1: Values of A , D_1 , D_2 and D_3 for the axial and transverse directions.

	Axial	Transverse
A	11.5	2.16
D_1	-0.2	0.5
D_2	$1 + 1.26\exp^{-382(d/2r)}$	1
D_3	$0.87 \cos(\theta)$	$1 + 2.1 \sin(\theta)$

and $d/2r = 0$ for $\theta = 30^\circ$ in Figure 4.4a both agree with measured values for k_a (Boudenne *et al.*, 2015), implying that the particle chains in the experimental samples have a relatively small $d/2r \approx 0.001$ or an equivalent zigzag angle $\theta \approx 30^\circ$.

Regarding k_t , the equivalent value of $\theta \approx 55^\circ$, which is depicted by the dashed line in Figure 4.4a. Ideally, both values of θ predicted using Equation 4.4 for k_a and k_t should be identical. In this case, the higher value of θ for k_t is attributed to side branching of particle chains (Boudenne *et al.*, 2015) that is not considered by Equation 4.4 but is instead captured by the higher equivalent value of θ .

We note that the proposed model is limited to chainlike structures consisting of spherical thermal conductive filler particles and a polymer matrix without interfacial resistance, and it is applicable only when $\psi < 0.35$. For fractions larger than $\psi > 30\%$, chains are more likely to form side branches (Goc *et al.*, 2016), diminishing their advantage (Boudenne *et al.*, 2015; Gaska *et al.*, 2015; Goc *et al.*, 2016). The more side branches there are, the closer are the values of k_a and k_t . To maximize the utilization of the chain structures, the proposed model suggests that the maximum anisotropy k_a/k_t occurs at $\psi = 0.293$ for connected chains with $k_a/k_t = 3.27$ (Figure 4.4b). If only disconnected chains are considered, i.e., $d/2r > 0$, the optimum value of ψ occurs at the lowest $d/2r$. For example, for the case $d/2r \geq 0.001$, the optimum

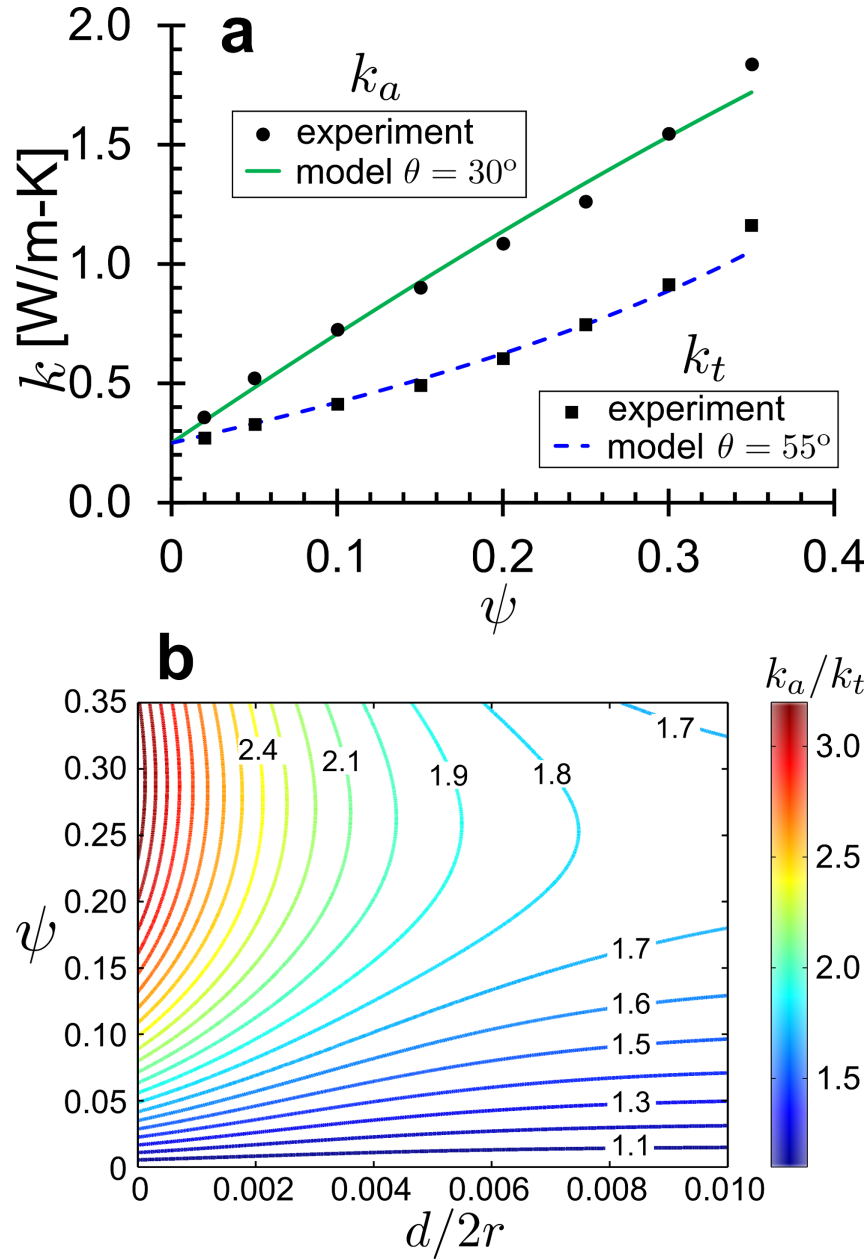


Figure 4.4: (a) The average θ for a zigzag chainlike structure in experiments (Boudenne *et al.*, 2015) can be reproduced through the modified models that we have proposed, using $\theta \approx 30^\circ$ for the k_a results and $\approx 55^\circ$ for k_t . (b) Contour plot of thermal conductivity anisotropy k_a/k_t predicted using Equation 4.4 and Table 4.1 with $\theta = 0^\circ$ shows that the k_a/k_t maxima of 3.27 occurs when $d/2r = 0$ and $\psi = 0.293$. As $d/2r$ increases, the value of the local maxima of k_a/k_t approaches 1.75 at $\psi = 0.250$.

$\psi = 0.285$ and $k_a/k_t = 2.77$, while for $d/2r \geq 0.01$, these values are $\psi = 0.250$ and $k_a/k_t = 1.75$. All these maxima occur at $\theta = 0^\circ$, i.e., for straight chains.

The value of d should be larger than the mean free path for phonon transport, which is typically a few angstroms or nanometers for amorphous polymers (Ngo *et al.*, 2016). When d is smaller than the phonon mean free path, particle chains should be treated as being connected, i.e., effectively $d/2r = 0$.

4.4 Conclusion

In summary, we demonstrate how anisotropic thermal conductivity can be introduced in a soft particulate-reinforced composite material, which consists of nickel particles distributed in a PDMS matrix. By arranging filler particles into chains, and varying their interparticle spacing and internal zigzag angle, it is possible to tailor the anisotropic thermal conductivity of the composite as desired. The simulations show that the axial thermal conductivity increases with filler volume fraction, but decreases exponentially with increasing interparticle spacing. The transverse thermal conductivity also increases with filler volume fraction but is not influenced by the interparticle spacing. As the zigzag angle increases to $\approx 55^\circ$, the axial thermal conductivity approaches a minimum value, while the transverse thermal conductivity approaches a maximum value. We propose a modified empirical model that predicts the axial and transverse components of the anisotropic thermal conductivity of the composite. The model, which includes the effects of the particle chain organization, interparticle spacing, and zigzag angle, can be used to (1) identify the equivalent characteristics of chain organization inside particle-polymer composite samples, and

(2) assist in composite material design for applications where anisotropic conductivity is desired. The results and model lay the foundation for advanced additive manufacturing strategies to produce particulate-reinforced soft composite materials by arranging conductive particles with customized directional thermal conductivity.

4.5 Acknowledgements

This work was supported by a Discovery Grant from the Natural Sciences and Engineering Research Council of Canada (NSERC) under grant number RGPIN-2014-04066.

4.6 Supporting Information

4.6.1 Simulation methods, settings, and verification

Simulations using Representative Volume Element (RVE), or unit cell, for estimating bulk material properties are conducted. This minimal simulation method provides a domain that reduces the computational cost but is able to maintain identical material properties throughout the material. Due to the symmetry of the chainlike particle structures, we construct a rectangular cuboid domain consisting of two 1/8 spherical particles for straight chains, as shown in Figure 4.5a. For zigzag chains, two quarter spheres are employed, as shown in Figure 4.5b and d. The filler volume fraction determines the length and width of the domain, while its height is determined from the interparticle spacing and zigzag angle. Maintaining constant particle size, the volume fraction, interparticle spacing, and zigzag angle are varied by changing the size of

the cuboid domain.

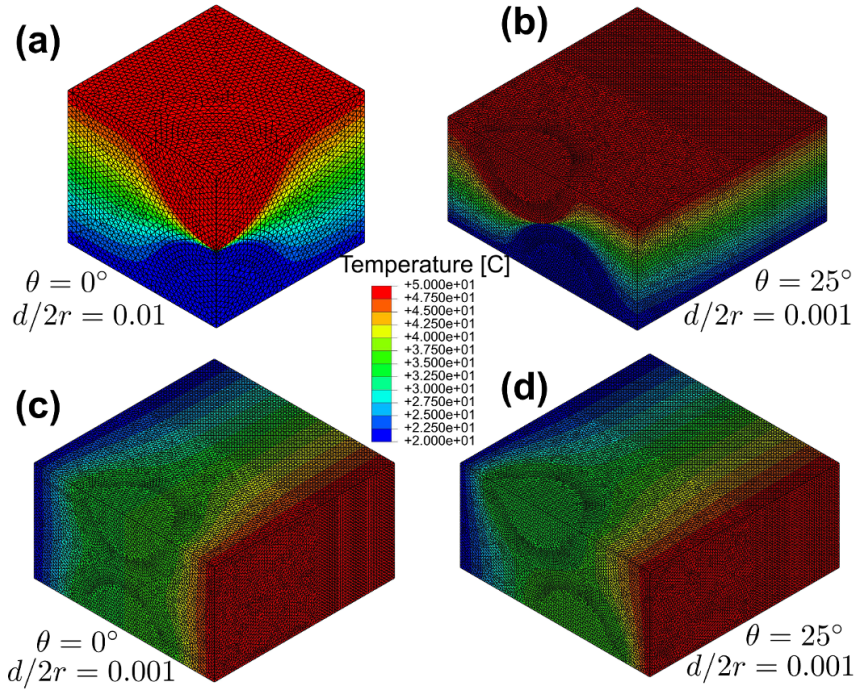


Figure 4.5: Examples of the temperature distribution while determining the axial thermal conductivity of (a) straight chain ($\theta = 0^\circ$ and $d/2r = 0.01$), (b) zigzag chain ($\theta = 25^\circ$ and $d/2r = 0.001$) cuboids, and the transverse thermal conductivity of (c) straight chain ($\theta = 0^\circ$ and $d/2r = 0.001$) and (d) zigzag chain ($\theta = 25^\circ$ and $d/2r = 0.001$) cuboids.

Spherical nickel particles of uniform $5.69 \mu\text{m}$ radius and a homogeneous thermal conductivity of 91 W/m-K are inserted into a polydimethylsiloxane (PDMS) matrix that has a thermal conductivity of 0.25 W/m-K (Hull and Clyne, 1996). To facilitate symmetry and the RVE, the boundary conditions on the four orthogonal surfaces are adiabatic, i.e., the cuboid is insulated on its transverse sides, while the two opposite axial surfaces are isothermal at temperatures $T_h = 50^\circ\text{C}$ on one surface and $T_c = 20^\circ$ on the other. For an appropriate mesh, 10-node quadratic heat transfer tetrahedron elements (DC3D10 in ABAQUS) are used to better represent the spherical shape of the filler particles.

The effective thermal conductivity of a composite material can be determined using Fourier's heat conduction law. At steady state with no heat source or sink within the cuboid and no heat loss from its sides, the heat transfer rate across the two opposite isothermal surfaces must be equal. This rate obtained from a simulation also accounts for the overall thermal resistance originating from the complex 3D filler particle arrangements inside the composite material. Therefore, the effective thermal conductivity of a composite can be determined by using this heat transfer rate into the Fourier law equation. The mesh sensitivity, or grid independency, of the simulations is verified by ensuring that the variation of the heat transfer rates across the two opposite axial surfaces is in agreement within 0.1%, otherwise mesh refinement is performed.

To demonstrate that our selection of RVE is appropriate, we note that the same effective thermal conductivity is achieved from simulations that combine multiple RVEs. Since we use constant thermal conductivities for nickel and PDMS, different isothermal temperatures can be applied at the non-adiabatic axial surfaces as long as these temperatures are within a reasonable range to ensure constant thermal conductivity in the cuboid. Doing so, results in the same effective thermal conductivity. Moreover, simulations for different dimensions, e.g., by scaling up the entire domain leading to particle radius of 56.9 μm or 5.69 mm, are examined and shown to provide identical effective thermal conductivities. This confirms that the simulations are size independent.

4.6.2 Model verification for random configuration

To further verify our simulation models, we compare the results of the composite containing randomly distributed particles to various theoretical and empirical models, namely, Maxwell, Lichtenecker, Cheng-Vachon, Lewis-Nielsen, Agari-Uno, and Ngo models, as shown in Figure 4.2a. Ten spherical filler particles are individually placed inside a cubic matrix domain with their coordinates created from a random number generator with constraints. All particles are restricted to the bounds of the cubic domain, and completely separated from each other (none of them can be connected). For each volume fraction, five of these realizations are simulated, and the average of them are presented. The deviations among these five models are demonstrated as the error bars in Figure 4.2a.

In general, for a two-phase material composite, the effective thermal conductivity of the composite (k_c) is influenced by the attributes of its constituents, i.e., the thermal conductivity of the filler (k_f) and the matrix (k_m), and the filler volume fraction (ψ). Despite the simple rule-of-mixture that defines the upper and lower bound of k_c , Lichtenecker employed the logarithmic law of mixing (Boudenne *et al.*, 2015), or mean geometric method (Kumlutas and Tavman, 2006), with consideration of spheroids fillers that are uniformly distributed but randomly oriented in a continuous matrix:

$$\log k_c = (1 - \psi) \log k_m + \psi \log k_f. \quad (4.5)$$

Agari and Uno modified Lichtenecker's model to include the effect of the particles on the secondary structure, such as crystallinity, of the polymer, and the easiness of these particles forming conductive path (Kumlutas and Tavman,

2006):

$$\log k_c = (1 - \psi)\log(C_1 k_m) + \psi C_2 \log k_f, \quad (4.6)$$

where C_1 and C_2 are experimental constants that need to be obtained *a priori* by fitting appropriate experimental data for the desired composites (Kumlutas and Tavman, 2006). The Maxwell model:

$$k_c = k_m \frac{2k_m + k_f - 2\psi(k_m - k_f)}{2k_m + k_f + \psi(k_m - k_f)}, \quad (4.7)$$

is derived theoretically for the thermal conductivity of non-interacting randomly distributed spherical particles in a continuous matrix (Kumlutas and Tavman, 2006). The Cheng and Vachon model is expressed in terms of the distribution function of the filler and the matrix (Kumlutas and Tavman, 2006; Ngo *et al.*, 2016):

$$\begin{aligned} \frac{1}{k_c} = & \frac{1}{\sqrt{C(k_f - k_m)[k_m + B(k_f - k_m)]}} \\ & \times \ln \frac{\sqrt{k_m + B(k_f - k_m)} + (B/2)\sqrt{C(k_f - k_m)}}{\sqrt{k_m + B(k_f - k_m)} - (B/2)\sqrt{C(k_f - k_m)}} + \frac{1 - B}{k_m}, \end{aligned} \quad (4.8)$$

where $B = \sqrt{3\psi/2}$, and $C = 4/B$. The semi-theoretical Lewis and Nielsen model takes into account the shape, the orientation, and the type of packing of the particles for a two-phase composites (Kumlutas and Tavman, 2006):

$$k_c = k_m \left(\frac{1 + AB\psi}{1 - B\psi C} \right), \text{ where} \quad (4.9)$$

$$B = \frac{(k_f/k_m) - 1}{(k_f/k_m) + A} \text{ and } C = 1 + \left(\frac{1 - \phi_m}{\phi_m^2} \right) \psi. \quad (4.10)$$

Ngo *et al.* proposed a general model based on numerical simulations (Ngo and

Byon, 2016). They focused on the effects of ψ , the ratio of thermal conductivities k_f/k_m , and the thermal contact resistance between the particle and the matrix. For the model without thermal contact resistance,

$$k_c = k_m + k_m \frac{A\sqrt{k_f/k_m(k_f/k_m - 1)}}{B + \sqrt{k_f/k_m(k_f/k_m - 1)}}, \text{ where} \quad (4.11)$$

$$A = 0.4918(\exp^{\psi/0.2276} - 1) + 2.161 \times 10^{-15}(\exp^{\psi/0.0149} - 1), \text{ and}$$

$$B = 3.2826 + 1.76 \times 10^{-21}\exp^{\psi/0.0104} + 0.1792\exp^{\psi/0.1364}.$$

These correlation constants are valid for $0 \leq \psi \leq 0.52$ and $1 \leq k_f/k_m \leq 10^8$.

Considering all these models, our results are in good agreement with the Maxwell, Lewis-Nielsen, Agari-Uno, and Ngo models, as presented in Figure 4.2a. The constants of the Agari-Uno model are obtained by fitting the simulation results ($C_1 = 0.983$ and $C_2 = 0.3927$), leading to a best fit for this model. For the Lewis-Nielsen model, the constants $A = 1.5$ for spherical particles (Kumlutas and Tavman, 2006), and $\phi_m = 0.59$ for loose random packing (Dullien, 1979) are used.

4.6.3 Packing fraction for simple cubic structures

The closest packing volume fraction of chainlike structure can be considered as that within a simple cube. When chains consisting of uniform size spheres are closely packed, i.e., there is no spacing between chains and between particles, the chainlike structure is identical to the simple cubic structure with the spheres on the 8 vertices of the cube connected to the adjacent particles. The

volume fraction at this point can be calculated:

$$\psi = \phi_m = \frac{\text{volume of the filler}}{\text{volume of the cube}} = \frac{8 \times (4/3\pi r^3) \times (1/8)}{(2r)^3} = 0.524, \quad (4.12)$$

where r denotes the radius of the particles. The length of the cube is $2r$ because there is no gap between adjacent particles. Thus, this volume fraction is applicable to Lewis-Nielsen model as $\phi_m = 0.524$ for chainlike structures.

Bibliography

- Abdel Fattah, A. R., Ghosh, S., and Puri, I. K. (2016). Printing Three-Dimensional Heterogeneities in the Elastic Modulus of an Elastomeric Matrix. *ACS Appl. Mater. Interfaces*, **8**(17), 11018–11023.
- Borbáth, T., Günther, S., Yu Borin, D., Gundermann, T., and Odenbach, S. (2012). X μ CT analysis of magnetic field-induced phase transitions in magnetorheological elastomers. *Smart Mater. Struct.*, **21**(10), 105018.
- Boudenne, A., Mamunya, Y., Levchenko, V., Garnier, B., and Lebedev, E. (2015). Improvement of thermal and electrical properties of Silicone–Ni composites using magnetic field. *Eur. Polym. J.*, **63**, 11–19.
- Collino, R. R., Ray, T. R., Fleming, R. C., Sasaki, C. H., Haj-Hariri, H., and Begley, M. R. (2015). Acoustic field controlled patterning and assembly of anisotropic particles. *Extrem. Mech. Lett.*, **5**, 37–46.
- Compton, B. G. and Lewis, J. A. (2014). 3D-printing of lightweight cellular composites. *Adv. Mater.*, **26**, 5930–5935.
- Coquelle, E. and Bossis, G. (2005). Magnetostriction and piezoresistivity in elastomers filled with magnetic particles. *J. Adv. Sci.*, **17**(1/2), 132–138.

Dallas, P., Georgakilas, V., Niarchos, D., Komninou, P., Kehagias, T., and Petridis, D. (2006). Synthesis, characterization and thermal properties of polymer/magnetite nanocomposites. *Nanotechnology*, **17**(8), 2046–2053.

Dullien, F. A. L. (1979). *Porous Media: Fluid Transport and Pore Structure*. Academic Press.

Fragouli, D., Das, A., Innocenti, C., Guttikonda, Y., Rahman, S., and Liu, L. (2014). Polymeric Films with Electric and Magnetic Anisotropy Due to Magnetically Assembled Functional Nano fibers. *ACS Appl. Mater. Interfaces*, **6**(6), 4535–4541.

Gaska, K., Kmita, G., Rybak, A., Sekula, R., Goc, K., and Kapusta, C. (2015). Magnetic-aligned, magnetite-filled epoxy composites with enhanced thermal conductivity. *J. Mater. Sci.*, **50**(6), 2510–2516.

Ghosh, S. and Puri, I. K. (2013). Soft polymer magnetic nanocomposites: microstructure patterning by magnetophoretic transport and self-assembly. *Soft Matter*, **9**(6), 2024–2029.

Ghosh, S. and Puri, I. K. (2015). Changing the magnetic properties of microstructure by directing the self-assembly of superparamagnetic nanoparticles. *Faraday Discuss.*, **181**, 423–435.

Ghosh, S., Tehrani, M., Al-haik, M. S., and Puri, I. K. (2015). Patterning the Stiffness of Elastomeric Nanocomposites by Magnetophoretic Control of Cross-linking Impeder Distribution. *Materials*, **8**, 474–485.

Goc, K., Gaska, K., Klimczyk, K., Wujek, A., Prendota, W., Jarosinski, L.,

- Rybak, A., Kmita, G., and Kapusta, C. (2016). Influence of magnetic field-aided filler orientation on structure and transport properties of ferrite filled composites. *J. Magn. Magn. Mater.*, **419**, 345–353.
- Han, Y., Hong, W., and Faidley, L. E. (2013). Field-stiffening effect of magneto-rheological elastomers. *Int. J. Solids Struct.*, **50**(14-15), 2281–2288.
- Hull, D. and Clyne, T. W. (1996). *An Introduction to Composite Materials*. Cambridge Solid State Science Series. Cambridge University Press.
- Khan, K. A., Khan, S. Z., and Khan, M. A. (2016). Effective thermal conductivity of two-phase composites containing highly conductive inclusions. *J. Reinf. Plast. Compos.*, **35**(21), 1586–1599.
- Kokkinis, D., Schaffner, M., and Studart, A. R. (2015). Multimaterial magnetically assisted 3D printing of composite materials. *Nat. Commun.*, **6**, 8643.
- Kong, Y. L., Gupta, M. K., Johnson, B. N., and McAlpine, M. C. (2016). 3D printed bionic nanodevices. *Nano Today*, **11**(3), 330–350.
- Kumlutas, D. and Tavman, I. H. (2006). A Numerical and Experimental Study on Thermal Conductivity of Particle Filled Polymer Composites. *J. Thermoplast. Compos. Mater.*, **19**(4), 441–455.
- Li, Z., Wu, W., Chen, H., Zhu, Z., Wang, Y., and Zhang, Y. (2013). Thermal conductivity of micro/nano filler filled polymeric composites. *RSC Adv.*, **3**(18), 6417–6428.
- Ngo, I. and Byon, C. (2016). Thermal conductivity of particle-filled polymers.

- In A. Méndez-Vilas and A. Solano-Martín, editors, *Polym. Sci. Res. Adv. Pract. Appl. Educ. Asp.*, pages 554–565. Formatex Research Center.
- Ngo, I. L., Jeon, S., and Byon, C. (2016). Thermal conductivity of transparent and flexible polymers containing fillers: A literature review. *Int. J. Heat Mass Transf.*, **98**, 219–226.
- Nielsen, L. E. and Landel, R. F. (1994). *Mechanical Properties of Polymers and Composites*. Marcel Dekker, Inc., 2nd edition.
- Ramani, K. and Vaidyanathan, A. (1995). Finite Element Analysis of Effective Thermal Conductivity of Filled Polymeric Composites. *J. Compos. Mater.*, **29**(13), 1725–1740.
- Richter, C. and Lipson, H. (2011). Untethered hovering flapping flight of a 3D-printed mechanical insect. *Artif. Life*, **17**(2), 73–86.
- Siegel, A. C., Phillips, S. T., Dickey, M. D., Lu, N., Suo, Z., and Whitesides, G. M. (2010). Foldable printed circuit boards on paper substrates. *Adv. Funct. Mater.*, **20**(1), 28–35.
- Tsai, P. J., Ghosh, S., Wu, P., and Puri, I. K. (2016). Tailoring Material Stiffness by Filler Particle Organization. *ACS Appl. Mater. Interfaces*, **8**(41), 27449–27453.
- Wang, H., Chen, Q. W., Sun, L. X., Qi, H. P., Yang, X., Zhou, S., and Xiong, J. (2009). Magnetic-field-induced formation of one-dimensional magnetite nanochains. *Langmuir*, **25**(12), 7135–7139.
- Yuan, C., Duan, B., Li, L., Xie, B., Huang, M., and Luo, X. (2015). Thermal

Conductivity of Polymer-Based Composites with Magnetic Aligned Hexagonal Boron Nitride Platelets. *ACS Appl. Mater. Interfaces*, **7**(23), 13000–13006.

Yuan, C., Li, L., Duan, B., Xie, B., Zhu, Y., and Luo, X. (2016). Locally reinforced polymer-based composites for efficient heat dissipation of local heat source. *Int. J. Therm. Sci.*, **102**, 202–209.

Zhu, Y.-F., Ma, C., Zhang, W., Zhang, R.-P., Koratkar, N., and Liang, J. (2009). Alignment of multiwalled carbon nanotubes in bulk epoxy composites via electric field. *J. Appl. Phys.*, **105**(5), 054319.

Chapter 5

Conclusion and Future Directions

5.1 Conclusion

This dissertation has demonstrated that filler particle arrangements enable the tailoring of anisotropic material properties of particulate-reinforced elastomeric composites, such as mechanical stiffness, electric permittivity, and thermal conductivity. By introducing an internal zigzag angle into the chain-like structures, the properties can be fine-tuned. When stiff filler particles are assembled into linear chains with loading direction parallel to the chains, the stiffness strengthening effect can be up to approximate 100 times comparing to the elastomeric composite with randomly distributed filler particles. Also, both electrical permittivity and thermal conductivity along the chain direction increase in the presence of particle chains. All three properties investigated here increase with filler volume fraction and decreases gradually with increasing internal zigzag angle.

The influences of interparticle and interchain spacing and particle sizes on permittivity are explored. With increasing interparticle spacing, the bulk

permittivity decreases exponentially. This implies the permittivity enhancement is most pronounced when the conductive particles are interconnected. As interchain spacing increases, the permittivity increases. Regarding the size effect, the one with smaller particles has higher permittivity when the filler volume fraction is less than 9%. When the volume fraction is greater than 9%, the composite with larger particles has higher permittivity. Competing effects between the volume fraction and the interchain spacing occur when the volume fraction is greater than 9%, leading to gradual enhancement in permittivity.

The impact of interparticle spacing on both axial and transverse thermal conductivities is examined. The axial thermal conductivity decreases exponentially with increasing interparticle spacing, while the transverse conductivity is not affected. As for zigzag angle, the axial conductivity decreases with increasing zigzag angle, while the transverse conductivity increases with it. A modified empirical model to predict the axial and transverse thermal conductivities is proposed. In addition to the volume fractions and the thermal conductivities of the composite constituents, the model includes the effects of the particle chain organization, interparticle spacing, and zigzag angle. The model can not only identify the equivalent characteristics of chainlike filler particle structures of polymer composite samples, but also expedite the process of composite material design where anisotropic conductivity is pursued.

The results presented here is highly qualitative due to many simplifications. Also, the precise placement of filler particles reported here is still impossible based on current technology. However, the rapid development of additive manufacturing and field-assisted assembly reveals enormous potential for realizing this precise placement of particles in the near future, where the study shown here will shine and contribute most.

5.2 Future Directions

5.2.1 Model Improvements

Interfacial Properties

The influence of bonding between filler particles and the matrices on the effective material properties cannot be overlooked. This bonding can be simulated through consideration of interfacial layers, which can be a single layer of cohesive element that characterize the bonding behaviour (Qu *et al.*, 2005), an interfacial layer of finite thickness with gradual variation of properties transitioned from that of filler particles to that of the matrices (Ozmusul and Picu, 2002), or through molecular dynamic simulations (Choi *et al.*, 2015). Hence, for the models that include interfacial layers, it is possible to explore the influences of bonding strength, the change of isotropic or anisotropic properties in the interfacial regions, the doping or diffusion of filler and matrix molecules, and so on.

Polydispersed and Anisotropic Fillers

In real world material systems, the dimension of filler particles is rarely uniform. To compensate this, one can simply use a model consisting of various sizes of particles. This will inevitably increase the computational cost because now the size of the modelling RVE is significantly larger in order to maintain the quality of representing the whole material.

If the particles are polydispersed in space domain, i.e., non-uniformly distributed, the modelling has to include the entire material system since the RVE approach is no longer valid in this situation.

Unlike the computationally expensive polydispersed systems, fillers with anisotropic properties, such as carbon nano tubes, can be cheaply employed. The only change from an isotropic model is the anisotropic material properties. There is no need to change the modelling domain if the filler geometries of both models are identical.

5.2.2 Other Particle Organizations

The feasibility of exploring unlimited designs is one of the biggest advantages that numerical simulations possess. In the history of engineered material development, only those structures, shapes, and arrangements that are considered easy to fabricate are chosen. Since the late 20th century, more and more focus has turned to nature for inspiration to solve modern engineering challenges (Fratzl, 2007), leading to emerging biomimicking and bio-inspired research across disciplines. The honeycomb structure is the most widely used example of bio-inspired configurations. Another common pattern found in nature is logarithmic spiral, which is still rare in man-made objects. This spiral is also called *Spira mirabilis*, Latin for “miraculous spiral”, by Jacob Bernoulli due to its unique fully scalable self-similarity characteristic, i.e., the shape of the spiral is independent of its size. Natural examples of logarithmic spirals are observed in the nautilus shells, the flying path of a hawk approaching its prey (Chin, 2000), the swirl pattern of tropical cyclones (Gray, 1901), or as enormous as the arms of spiral galaxies (Bertin and Lin, 1996), etc. Even so, the equation that describe logarithmic spiral in polar coordinates (r, θ) is fairly straight forward:

$$r = ae^{b\theta}$$

where a and b denote arbitrary positive real constants. Therefore, one can explore the two constants that form the backbone structure of the filler arrangement and perform an optimal design that tailor to a customized application.

5.2.3 Wing Design of Micro Aerial Vehicles

The feasibility of adjusting material stiffness by arranging the embedded filler particles within elastomeric matrix in particular configurations enables the ability of applying stiffness enhancements in local regions readily. Most objects have nonuniform material stiffness. For large objects, e.g., airplanes, bridges, etc., large areas of stiffer materials are patched on the regions of interest for strengthening. The stronger the better is the philosophy when developing material for large scale applications; while for small scale applications, e.g., insect wings, micro air vehicle, etc., the ability of creating stiffness enhancement in small local areas is more essential which is a promising target field of this thesis research.

Wing design of micro aerial vehicles (MAVs) embraces the local stiffness design of elastomeric composites. In nature, flight behaviours and wing designs can be categorized into active and passive, as shown in Table 5.1. An active flight occurs when an object actively manipulates the surrounding air vortices in order to fly, such as birds and insects flapping their wings; on the other hand, a passive flight occurs when an object flies with the wind, such as the soaring and gliding of eagles, flying of airplanes, seeds, pollen, etc. Each flight group can be further divided by wing design, where active wings have muscles or actuators to change the wing profile actively, while passive wing profiles are fixed, i.e., not able to change actively.

Table 5.1: Examples of flying objects into four categories.

	Active Flight	Passive Flight
Active Wing	flapping wing birds	glider (eagles), airplanes
Passive Wing	insects	seeds, pollens

Passive wing designs are often observed in smaller scale objects, an area where this research is applicable. Experiments have demonstrated the heterogeneous stiffness distribution in insect wings (Combes and Daniel, 2003). Centimetre scale artificial insect wings have been fabricated through MEMS techniques by using carbon fibre veins and polyester membranes to create realizations of heterogeneous stiffness (Shang *et al.*, 2009). The process is highly labour intensive. Therefore, through the numerical simulation approaches reported herein, one can perform virtual design and optimize wing designs for different MAV applications by simply changing the filler microstructure in elastomeric composites to achieve the desired stiffness gradients on the wings. Subsequently, optimal designs can be delivered for additive manufacturing followed by required tests. Such a process greatly improves the efficiency and lowers the cost of the entire design and manufacturing stages. It also provides endless possibilities for ultimate designs.

Bibliography

- Abdel Fattah, A. R., Ghosh, S., and Puri, I. K. (2016). Printing microstructures in a polymer matrix using a ferrofluid droplet. *J. Magn. Magn. Mater.*, **401**, 1054–1059.
- Batra, S. and Cakmak, M. (2015). Ultra-capacitor flexible films with tailored dielectric constants using electric field assisted assembly of nanoparticles. *Nanoscale*, **7**(48), 20571–20583.
- Bazin, G. and Zhu, X. (2013). Crystalline colloidal arrays from the self-assembly of polymer microspheres. *Prog. Polym. Sci.*, **38**(2), 406–419.
- Beal, D. N., Hover, F. S., Triantafyllou, M. S., Liao, J. C., and Lauder, G. V. (2006). Passive propulsion in vortex wakes. *J. Fluid Mech.*, **549**, 385–402.
- Bele, A., Cazacu, M., Stiubianu, G., Vlad, S., and Ignat, M. (2015). Polydimethylsiloxane–barium titanate composites: Preparation and evaluation of the morphology, moisture, thermal, mechanical and dielectric behavior. *Compos. Part B Eng.*, **68**, 237–245.
- Bertin, G. and Lin, C. C. (1996). *Spiral structure in galaxies: a density wave theory*. MIT Press.

- Chawla, K. K. (2012). *Composite Materials Science and Engineering*. Springer, third edition.
- Chin, G. J. (2000). ORGANISMAL BIOLOGY: Flying Along a Logarithmic Spiral. *Science*, **290**(5498), 1857c–1857.
- Choi, J., Shin, H., Yang, S., and Cho, M. (2015). The influence of nanoparticle size on the mechanical properties of polymer nanocomposites and the associated interphase region: A multiscale approach. *Compos. Struct.*, **119**, 365–376.
- Collino, R. R., Ray, T. R., Fleming, R. C., Sasaki, C. H., Haj-Hariri, H., and Begley, M. R. (2015). Acoustic field controlled patterning and assembly of anisotropic particles. *Extrem. Mech. Lett.*, **5**, 37–46.
- Combes, S. A. (2010). Materials, structure, and dynamics of insect wings as bioinspiration for MAVs.
- Combes, S. A. and Daniel, T. L. (2003). Into thin air: Contributions of aerodynamic and inertial-elastic forces to wing bending in the hawkmoth *Manduca sexta*. *J. Exp. Biol.*, **206**(Pt 17), 2999–3006.
- Eigler, D. M. and Schweizer, E. K. (1990). Positioning single atoms with a scanning tunnelling microscope. *Nature*, **344**(6266), 524–526.
- Einstein, A. (1956). *Investigations on the Theory of the Brownian Movement*. Courier Corporation.
- Eshelby, J. (1957). The determination of the elastic field of an ellipsoidal inclusion, and related problems. *Proc. R. Soc.*, **241**(1226), 376–396.

- Esposito, C. J., Tangorra, J. L., Flammang, B. E., and Lauder, G. V. (2012). A robotic fish caudal fin: effects of stiffness and motor program on locomotor performance. *J. Exp. Biol.*, **215**(1), 56–67.
- Felton, S. M., Tolley, M. T., Onal, C. D., Rus, D., and Wood, R. J. (2013). Robot self-assembly by folding: A printed inchworm robot. *2013 IEEE Int. Conf. Robot. Autom.*, pages 277–282.
- Fratzl, P. (2007). Biomimetic materials research: what can we really learn from nature’s structural materials? *J. R. Soc. Interface*, **4**(March), 637–642.
- Fu, S.-Y., Xu, G., and Mai, Y.-W. (2002). On the elastic modulus of hybrid particle/short-fiber/polymer composites. *Compos. Part B Eng.*, **33**(4), 291–299.
- Fu, S.-Y., Feng, X.-Q., Lauke, B., and Mai, Y.-W. (2008). Effects of particle size, particle/matrix interface adhesion and particle loading on mechanical properties of particulate-polymer composites. *Compos. Part B Eng.*, **39**(6), 933–961.
- Genzer, J., Liu, Y., Shaw, B., and Dickey, M. (2014). Light-induced sequential self-folding of pre-strained polymer sheets. *Bull. Am. Phys. Soc.*, **59**.
- Ghosh, S. and Puri, I. K. (2013). Soft polymer magnetic nanocomposites: microstructure patterning by magnetophoretic transport and self-assembly. *Soft Matter*, **9**(6), 2024–2029.
- Glotzer, S. C. and Solomon, M. J. (2007). Anisotropy of building blocks and their assembly into complex structures. *Nat. Mater.*, **6**(7), 557–562.
- Gray, A. (1901). *Treatise on Physics*. Churchill.

- Guffey, M. J. and Scherer, N. F. (2010). All-optical patterning of Au nanoparticles on surfaces using optical traps. *Nano Lett.*, **10**(11), 4302–4308.
- Guth, E. (1945). Theory of filler reinforcement. *J. Appl. Phys.*, **16**(1), 20–25.
- Halpin, J. C. (1969a). Effects of Environmental Factors on Composite Materials. Technical report.
- Halpin, J. C. (1969b). Stiffness and Expansion Estimates for Oriented Short Fiber Composites. *J. Compos. Mater.*, **3**(4), 732–734.
- Hashin, Z. and Shtrikman, S. (1963). A variational approach to the theory of the elastic behaviour of multiphase materials. *J. Mech. Phys. Solids*, **11**(42), 127–140.
- Jouni, M., Boudenne, A., Boiteux, G., Massardier, V., Garnier, B., and Serghei, A. (2013). Electrical and thermal properties of polyethylene/silver nanoparticle composites. *Polym. Compos.*, **34**(5), 778–786.
- Kokkinis, D., Schaffner, M., and Studart, A. R. (2015). Multimaterial magnetically assisted 3D printing of composite materials. *Nat. Commun.*, **6**, 8643.
- Li, S. (2008). Boundary conditions for unit cells from periodic microstructures and their implications. *Compos. Sci. Technol.*, **68**(9), 1962–1974.
- Long, J. H., Hale, M. E., McHenry, M. J., and Westneat, M. W. (1996). Functions of fish skin: Flexural stiffness and steady swimming of longnose gar *Lepisosteus osseus*. *J. Exp. Biol.*, **199**(10), 2139–2151.

- Michel, J. C., Moulinec, H., and Suquet, P. (1999). Effective properties of composite materials with periodic microstructure: a computational approach. *Comput. Methods Appl. Mech. Eng.*, **172**, 109–143.
- Móczó, J. and Pukánszky, B. (2008). Polymer micro and nanocomposites: Structure, interactions, properties. *J. Ind. Eng. Chem.*, **14**(5), 535–563.
- Morariu, M. D., Voicu, N. E., Schäffer, E., Lin, Z., Russell, T. P., and Steiner, U. (2003). Hierarchical structure formation and pattern replication induced by an electric field. *Nat. Mater.*, **2**(1), 48–52.
- Mori, T. and Tanaka, K. (1973). Average stress in matrix and average elastic energy of materials with misfitting inclusions. *Acta Metall.*, pages 1–4.
- Moulinec, H. and Suquet, P. (1998). A numerical method for computing the overall response of nonlinear composites with complex microstructure. *Comput. Methods Appl. Mech. Eng.*, **157**, 69–94.
- Mountcastle, A. M. and Combes, S. A. (2013). Wing flexibility enhances load-lifting capacity in bumblebees. In *Proc. Biol. Sci.*, volume 280, page 20130531.
- Mountcastle, A. M. and Combes, S. A. (2014). Biomechanical strategies for mitigating collision damage in insect wings : structural design versus embedded elastic materials. *J. Exp. Biol.*, **217**(7), 1108–1115.
- Nakakubo, T. and Shimoyama, I. (2000). Three-dimensional micro self-assembly using bridging flocculation. *Sensors Actuators A Phys.*, **83**(1-3), 161–166.

- Nemiroski, A., Gonidec, M., Fox, J. M., Jean-Remy, P., Turnage, E., and Whitesides, G. M. (2014). Engineering shadows to fabricate optical metasurfaces. *ACS Nano*, **8**(11), 11061–11070.
- Ni, Y. and Chiang, M. Y. (2007). Prediction of elastic properties of heterogeneous materials with complex microstructures. *J. Mech. Phys. Solids*, **55**(3), 517–532.
- Nielsen, L. E. (1970). Generalized equation for the elastic moduli of composite materials. *J. Appl. Phys.*, **41**(11), 4626–4627.
- Nielsen, L. E. and Landel, R. F. (1994). *Mechanical Properties of Polymers and Composites*. Marcel Dekker, Inc., 2nd edition.
- Nielsen, L. F. (2005). *Composite Materials Properties as Influenced by Phase Geometry*. Springer.
- Ozmusul, M. S. and Picu, R. C. (2002). Elastic moduli of particulate composites with graded filler-matrix interfaces. *Polym. Compos.*, **23**(1), 110–119.
- Pandey, S., Gultepe, E., and Gracias, D. H. (2013). Origami inspired self-assembly of patterned and reconfigurable particles. *J. Vis. Exp.*, (72), e50022.
- Py, C., Reverdy, P., Doppler, L., Bico, J., Roman, B., and Baroud, C. (2007). Capillary Origami: Spontaneous Wrapping of a Droplet with an Elastic Sheet. *Phys. Rev. Lett.*, **98**(15), 156103.
- Qu, S., Siegmund, T., Huang, Y., Wu, P., Zhang, F., and Hwang, K. (2005). A

- study of particle size effect and interface fracture in aluminum alloy composite via an extended conventional theory of mechanism-based strain-gradient plasticity. *Compos. Sci. Technol.*, **65**(7-8), 1244–1253.
- Rothmund, P. W. K. (2006). Folding DNA to create nanoscale shapes and patterns. *Nature*, **440**(7082), 297–302.
- Sample, C. S., Xu, A. K., Swartz, S. M., and Gibson, L. J. (2015). Nanomechanical properties of wing membrane layers in the house cricket (*Acheta domesticus* Linnaeus). *J. Insect Physiol.*, **74**, 10–15.
- Shang, J. K., Combes, S. A., Finio, B. M., and Wood, R. J. (2009). Artificial insect wings of diverse morphology for flapping-wing micro air vehicles. *Bioinspir. Biomim.*, **4**(3), 036002.
- Shelton, R. M., Thornycroft, P. J. M., and Lauder, G. V. (2014). Undulatory locomotion of flexible foils as biomimetic models for understanding fish propulsion. *J. Exp. Biol.*, **217**(12), 2110–2120.
- Siddique, R. H., Gomard, G., and Hölscher, H. (2015). The role of random nanostructures for the omnidirectional anti-reflection properties of the glasswing butterfly. *Nat. Commun.*, **6**(November), 6909.
- Sreetharan, P. S., Whitney, J. P., Strauss, M. D., and Wood, R. J. (2012). Monolithic fabrication of millimeter-scale machines. *J. Micromechanics Microengineering*, **22**(5), 055027.
- Syms, R., Yeatman, E., Bright, V., and Whitesides, G. (2003). Surface tension-powered self-assembly of microstructures-the state-of-the-art. *J. Microelectromechanical Syst.*, **12**(4), 387–417.

- Tibbits, S. (2012). Design to Self-Assembly. *Archit. Des.*, **82**(2), 68–73.
- Tibbits, S. (2014). 4D Printing: Multi-Material Shape Change. *Archit. Des.*, **84**(1), 116–121.
- Tibbits, S. and Cheung, K. (2012). Programmable materials for architectural assembly and automation. *Assem. Autom.*, **32**(3), 216–225.
- Tsai, S. W. (1968). Formulas for the Elastic Properties of Fiber-Reinforced Composites. Technical report.
- Vincent, J. F. V. (2002). Arthropod cuticle: A natural composite shell system. *Compos. Part A Appl. Sci. Manuf.*, **33**(10), 1311–1315.
- Wang, H., Chen, Q. W., Sun, L. X., Qi, H. P., Yang, X., Zhou, S., and Xiong, J. (2009). Magnetic-field-induced formation of one-dimensional magnetite nanochains. *Langmuir*, **25**(12), 7135–7139.
- Whitney, J. P., Sreetharan, P. S., Ma, K. Y., and Wood, R. J. (2011). Pop-up book MEMS. *J. Micromechanics Microengineering*, **21**(11), 115021.
- Young, R. J. and Lovell, P. A. (2011). *Introduction to polymers*. CRC press.

Appendix A

Matlab Code for Random Configurations

A.1 RangGen2_rad_v1.m

```
clc;clear
```

```
%FOR GENERAL BRICK CELL!!!
```

```
%*****
```

```
%CONTROLS
```

```
%-----
```

```
%Length of each side of the 1/8 Unit Cell
```

```
lx = 0.3131;
```

```
ly = 0.3131;
```

```
lz = 0.3131;
```

```
%Number of particles
```

```
num = 10;
```

```
%Particle radius
r = 0.0569;
%Factor of safety for dist
sf = 1.01;
%Constraint distributed radius
Rc = 100*r;
%=====

%*****
%PRELIMINARY CALCULATIONS
%-----
%Calculating boundaries
lb = sf*r;
ubx = lx - sf*r; uby = ly - sf*r; ubz = lz - sf*r;
Rcb = Rc - r;
%Shuffle
rng('shuffle')
%initiate array
pos = zeros(num, 6);
flag = ones(num, 1);
%=====

%*****
%ITERATION CONTROL
%-----

count2 = 0;
```

```

while max(flag) ~= 0

%*****
%PARTICLE - 1
%-----
pnum = 1;
%Make it fail
pos(1, 1:3) = [5e5, 5e5, 5e5];
%counter
count = 0;
%Separate
x = pos(pnum, 1); y = pos(pnum, 2); z = pos(pnum, 3);
%calculate radial distance
Rxz = sqrt ((x - lx/2).^2 + (z - lz/2).^2);
pos(pnum, 5) = Rxz;
%Iteratively get position
while (x < lb) || (x > ubx) || (y < lb) || (y > uby) ...
|| (z < lb) || (z > uby) || (Rxz > Rcb)
%pos(1, 1:3) = l*rand(1,3);
pos(1, 1) = lx*rand(1,1);
pos(1, 2) = ly*rand(1,1);
pos(1, 3) = lz*rand(1,1);
x = pos(pnum, 1); y = pos(pnum, 2); z = pos(pnum, 3);
Rxz = sqrt ((x - lx/2).^2 + (z - lz/2).^2);
pos(pnum, 5) = Rxz;
count = count + 1

```

```

end

disp('Particle 1 Done')

pos(pnum, 6) = count;
flag(pnum) = 0;

%=====

%*****

%PARTICLES 2 - num
%-----

for pnum = 2 : num
    pnum

    %Make it fail
    %-----

    pos(pnum, 1:3) = [5e5, 5e5, 5e5];

    %Separate
    x = pos(pnum, 1); y = pos(pnum, 2); z = pos(pnum, 3);
    %Initiate inter-particle distance array
    disnum = zeros(pnum - 1, 1);
    %Build neighbor distance list
    for cnum = 1 : pnum - 1;
        %Neighbor coordinates
        xn = pos(cnum, 1); yn = pos(cnum, 2); zn = pos(cnum, 3);
        %Calculate Distance
        disnum(cnum) = sqrt((x - xn).^2 + (y - yn).^2 + (z - zn).^2);
    end
end

```

```

d = min(disnum);
count = 0;
%calculate radial distance
Rxz = sqrt ((x - lx/2).^2 + (z - lz/2).^2);
pos(pnum, 5) = Rxz;

%Iterate particle position
%-----
while ((x < lb) || (x > ubx) || (y < lb) || (y > uby) ...
    || (z < lb) | (z > ubz) || (d < 2*sf*r)) ...
    || (Rxz > Rcb) && count < 1e4
%Generate from an RNS
%pos(pnum, 1:3) = l*rand(1,3);
pos(pnum, 1) = lx*rand(1,1);
pos(pnum, 2) = ly*rand(1,1);
pos(pnum, 3) = lz*rand(1,1);
%Separate
x = pos(pnum, 1); y = pos(pnum, 2); z = pos(pnum, 3);
%Calculate radial distance
Rxz = sqrt ((x - lx/2).^2 + (z - lz/2).^2);
pos(pnum, 5) = Rxz;
%Initiate array of inter-particle distances
disnum = zeros(pnum - 1, 1);
%Build neighbor distance list
for cnum = 1 : pnum - 1;
%Neighbor coordinates

```

```
xn = pos(cnum, 1); yn = pos(cnum, 2); zn = pos(cnum, 3);
%Calculate Distance
disnum(cnum) = sqrt((x - xn).^2 + (y - yn).^2 + (z - zn).^2);
end
d = min(disnum);
count = count + 1;
end

if count >= 1e3
flag(pnum) = 1;
else
flag(pnum) = 0;
end
flag

pos(pnum, 4) = d;
pos(pnum, 6) = count;
end

%=====
count2 = count2 + 1;
if count2 > 1e3
count2
error('unable to locate the random particles')
end
end

%=====
```

```

pos3 = pos(:, 1:3);
pos4 = pos(:, 1:4);
pos5 = pos(:, 1:5)

pos
dc = 2 * r * sf
count2
AR = (pi * Rc ^2)/ (lx * lz)
% calculate orderness parameters
% average and standard deviation of radial distance
AVE = mean(pos); STD = std(pos,1);
Rxx_ave = AVE(5)
Rxx_std = STD(5)
% average absolute deviation of y coordinate
AVED = mad(pos,0);
AVED(2);
% normalized AVED by length y
Xi = AVED(2)/ly

% visulization
% note: in Abaqus y direction is vertical by default.
% The vertical axis here is Z.
subplot(2,2,1);
plot3(pos(:, 1), pos(:, 2), pos(:, 3),'ko'); grid on
xlabel('x'); ylabel('y'); zlabel('z')
xlim([0 lx]); ylim([0 ly]); zlim([0 lz])

```

```
subplot(2,2,2);  
plot(pos(:, 1), pos(:, 3),'ro'); grid on  
xlabel('x'); ylabel('z');  
xlim([0 lx]); ylim([0 lz])
```

```
subplot(2,2,4);  
plot(pos(:, 1), pos(:, 2),'bo'); grid on  
xlabel('x'); ylabel('y');  
xlim([0 lx]); ylim([0 ly])
```

Appendix B

Matlab Code for Calculating Thermal Conductivity

B.1 conductivity2.m

```
function [qf,k] = conductivity2(outputfile, filename1, ...
filename2, Lx, Ly, Lz, T1, T2)
%% read the .rpt file
[Node_1,NT11_1,RFL11_1,HFLMag_1,HFLHFL1_1,HFLHFL2_1, ...
HFLHFL3_1] = importfile(filename1);
[Node_2,NT11_2,RFL11_2,HFLMag_2,HFLHFL1_2,HFLHFL2_2, ...
HFLHFL3_2] = importfile(filename2);

%% calculate heat flux and thermal conductivity
% from surface at y0, x0, or z0

qf_HFLMag_1 = mean(HFLMag_1);
```

```
qf_HFLHFL2_1 = mean(HFLHFL2_1);
qf_RFL_1 = sum(RFL11_1) / (Lx * Lz);
qf_1 = [qf_RFL_1, qf_HFLMag_1, qf_HFLHFL2_1];
qfm_1 = [qf_RFL_1, qf_HFLMag_1, qf_HFLHFL2_1, mean(abs(qf_1))]
k_1 = qfm_1 * Ly / abs((T1-T2));

% from surface at y1, x1, or z1
qf_HFLMag_2 = mean(HFLMag_2);
qf_HFLHFL2_2 = mean(HFLHFL2_2);
qf_RFL_2 = sum(RFL11_2) / (Lx * Lz);
qf_2 = [qf_RFL_2, qf_HFLMag_2, qf_HFLHFL2_2];
qfm_2 = [qf_RFL_2, qf_HFLMag_2, qf_HFLHFL2_2, mean(abs(qf_2))]
k_2 = qfm_2 * Ly / abs((T1-T2));

% check heat rate through top and bottom surface are conserved
q1 = abs(sum(RFL11_1))
q2 = abs(sum(RFL11_2))
diff = abs(( q1 - q2 ) / ( (q1 + q2)/2 ))

flag=0;
if diff > 10^-3
warning('Heat rate difference is > 0.001. Refine mesh.')
flag=1;
end

%%
```

```
titleformat = '%12s %16s %16s %16s %16s \r\n';
dataformat = '%12s %16e %16e %16e %16e \r\n';

fid=fopen(outputfile,'w');

fprintf(fid, '%s \r\n', filename1);
fprintf(fid,titleformat, 'item', 'RFL', 'HFL.Magnitude', ...
    'HFL.HFL2', 'average');
fprintf(fid,dataformat, 'heat flux', qfm_1);
fprintf(fid,dataformat, 'conductivity', k_1);
fprintf(fid, '%s \r\n', ' ');

fprintf(fid, '%s \r\n', filename2);
fprintf(fid,titleformat, 'item', 'RFL', 'HFL.Magnitude', ...
    'HFL.HFL2', 'average');
fprintf(fid,dataformat, 'heat flux', qfm_2);
fprintf(fid,dataformat, 'conductivity', k_2);

if flag == 1
    fprintf(fid, '%s \r\n', ' ');
    fprintf(fid, '%s %f %s \r\n', 'Heat rate difference is ', ...
        diff, ' > 0.001');
end

fclose(fid);
```

B.2 Batch Processing

B.2.1 BatchPost_k.m

```
clear;clc;

n = 8;

ly = 0.1146;

lx = [0.5172,0.3657,0.2586,0.2111,0.1829,0.1635, ...
0.1493,0.1382];
lz = [0.2604,0.1841,0.1302,0.1063,0.0921,0.0823, ...
0.0752,0.0696];

T1 = 20;
T2 = 50;

vf={'025','05','10','15','20','25','30','35'};
ModelType=['_a_d8_'];
Date=['20161108'];

for k = 1:n
    jobname{k}=['vf_pt', char(vf(k)), ModelType, Date];
    rpt_y0{k}=['vf_pt', char(vf(k)), ModelType, 'y0_', Date, ...
'.rpt'];
end
```

```
rpt_y1{k}=['vf_pt', char(vf(k)), ModelType, 'y1_', Date, ...  
' .rpt'];  
end  
  
for k = 1:n  
output{k}=['cond_', jobname{k}, '.txt'];  
conductivity2(output{k}, rpt_y0{k}, rpt_y1{k}, ...  
lx(k), ly, lz(k), T1, T2)  
end
```

B.2.2 BatchPost_k_zigzag.m

```
clear;clc;  
  
n = 13;  
  
T1 = 20;  
T2 = 50;  
  
ly = [0.1139,0.1135,0.1122,0.1100,0.1070,0.1032, ...  
0.0987,0.0933,0.0873,0.0805,0.0732,0.0653,0.0570];  
lx = [0.2058,0.2062,0.2073,0.2094,0.2123,0.2161, ...  
0.2211,0.2273,0.2351,0.2447,0.2566,0.2717,0.2910];  
lz = lx;
```

```
deg={'00','05','10','15','20','25','30','35','40','45', ...
    '50','55','60'};
ModelType=['_d2_'];
Date=['20160112'];

for k = 1:n
    jobname{k}=['vf_pt08_deg', char(deg(k)), ModelType, Date];
    rpt_y0{k}=['vf_pt08_deg', char(deg(k)), ModelType, 'y0_', ...
    Date, '.rpt'];
    rpt_y1{k}=['vf_pt08_deg', char(deg(k)), ModelType, 'y1_', ...
    Date, '.rpt'];
end
%%
for k = 1:n
    output{k}=['cond_', jobname{k}, '.txt'];
    conductivity2(output{k}, rpt_y0{k}, rpt_y1{k}, ...
    lx(k), ly(k), lz(k), T1, T2)
end
```